Titre: Title:	Development of Thermosetting Composite Materials for Producing Multifunctional Coatings by Direct Ink Writing
Auteur: Author:	David Brzeski
Date:	2021
Type:	Mémoire ou thèse / Dissertation or Thesis
Référence: Citation:	Brzeski, D. (2021). Development of Thermosetting Composite Materials for Producing Multifunctional Coatings by Direct Ink Writing [Master's thesis, Polytechnique Montréal]. PolyPublie. https://publications.polymtl.ca/9131/

POLYTECHNIQUE MONTRÉAL
affiliée à l'Université de Montréal

Development of Thermosetting Composite Materials for Producing Multifunctional Coatings by Direct Ink Writing

DAVID BRZESKI
Département de génie mécanique

Mémoire présenté en vue de l'obtention du diplôme de *Maîtrise ès sciences appliquées*
Génie aérospatial

Août 2021

POLYTECHNIQUE MONTRÉAL
affiliée à l'Université de Montréal

Ce mémoire intitulé :

Development of Thermosetting Composite Materials for Producing Multifunctional Coatings by Direct Ink Writing

présenté par **David BRZESKI**
en vue de l'obtention du diplôme de *Maîtrise ès sciences appliquées*
a été dûment accepté par le jury d'examen constitué de :

Farbod KHAMENEIFAR, président
Daniel THERRIAULT, membre et directeur de recherche
Annie ROSS, membre et codirectrice de recherche
Marie-Claude HEUZEY, membre

DEDICATION

For my supportive family, to whom I owe my success.

ACKNOWLEDGEMENTS

I would first like to direct my thanks towards Professor Daniel Therriault, my research director, as well as Professor Annie Ross, my co-director. Their precious advice and guidance certainly allowed me to progress greatly as a researcher during this endeavour, wherefore I must express my utmost respect for them. The great amount of freedom my director conferred upon me in conducting this project and his confidence in my work surely allowed me to hone my creativity in problem solving and my critical thinking aptitudes in the context of academic work. I am also indebted to Dr. Rouhollah D. Farahani who had his office door wide open for me from the start of my project.

I am appreciative of the members of the Laboratory of Multiscale Mechanics (LM^2) for their help and company during my studies. In particular, I must express my sincere gratitude to Dr. Iee Lee Hia, Dr. Audrey Diouf Lewis and Jean-François Chauvette whom with I spent countless hours debating and discussing my project. They helped me a great deal over the course of this endeavour, not only as co-workers, but also as friends especially during the pandemic which affected us all. I must also extend my recognition to our partners at Safran Composite and Safran Aircraft Engines whom counselled me over the course of my masters, especially Dr. Nicola Piccirelli.

I am sincerely grateful to the Natural Sciences and Engineering Research Council (NSERC), Safran S.A., the Ministère de l'Éducation et de l'Enseignement supérieur du Québec (MEES), Polytechnique Montréal, the Polish Socio-Cultural Foundation of Montréal and the Canadian Polish Millenium Fund for their financial support in the completion of my degree.

Finally, I must thank Polytechnique's Director of Graduate Studies, Dr. Delphine Périé-Curnier, for allowing me to participate in a student exchange at Politecnico di Milano, Italy. That experience taught me invaluable lessons in perseverance and relationship development, in addition to enabling me to acquire skills and expand knowledge which I would otherwise have missed on, and, of course, seeing a bit of the world out there in the process.

RÉSUMÉ

La démocratisation du transport aérien rend accessible tant les contrées éloignées que les grandes villes à un nombre croissant de voyageurs. Au vu des défis environnementaux découlant d'une mobilité accrue, de nouvelles normes internationales assujettissent le domaine de l'aviation civile à d'importantes restrictions quant à la pollution sonore et aux émissions de gaz à effet de serre. Ces normes poussent les fabricants de composantes aéronautiques à concevoir des produits d'ingénierie non seulement plus légers, mais aussi énergétiquement plus performants afin de réduire la consommation de carburant des aéronefs.

L'amélioration des turbosoufflantes à haut débit de dilution constitue la clé pour réduire les émissions nocives des avions. Dans la soufflante, il est possible d'optimiser la consommation de carburant en limitant les fuites d'air en bout d'aube. À cet effet, des revêtements de composites thermodurcissables, dits abradables, sont appliquées sur la périphérie intérieure du carter-moteur pour contrôler le jeu fonctionnel entre les aubes et la section stationnaire les entourant. Du même coup, il est envisagé d'intégrer une seconde fonctionnalité aux revêtements abradables, soit de structurer le revêtement de manière à obtenir des réseaux filamentaires ordonnés pouvant atténuer le bruit émis par la soufflante. La fabrication additive est un outil de choix pour mettre en forme de tels revêtements en raison de leur complexité. Cependant, il n'existe pas de matériau qui puisse remplir simultanément la fonction d'abradabilité et celle d'atténuation sonore. Ce projet est donc consacré à l'élaboration de matériaux composites thermodurcissables multifonctionnels pouvant être mis en forme par voie de fabrication additive, ici par écriture d'encre directe à haute vitesse.

Le produit abradable commercial couramment employé par Safran, le partenaire industriel de ce projet, n'est pas imprimable en raison du fort taux de microsphères de verre creuses dans le matériau. Le développement du nouveau matériau s'appuie ainsi sur la résine de base du produit commercial sans microsphères ajoutées. Différentes proportions de microsphères et/ou de nanoparticules de silice sont incorporées dans le but d'obtenir des formulations pouvant être non seulement extrudées par les buses de 250 µm, mais lesquelles ont aussi l'habileté de conserver leur forme imprimée pendant que le matériau polymérise et fige. Des observations au microscope électronique et des balayages d'imagerie par rayons-X sont utilisées pour analyser la forme des filaments extrudés ainsi que l'intégrité des microsphères post-impression. À l'issue des observations au microscope, les trois formulations présentant la meilleure fidélité géométrique et intégrité microstructurelle sont retenues. Par la suite, des analyses rhéologiques permettent d'en obtenir les profils de viscosité en juxtaposant les

effets de polymérisation et du taux de cisaillement induit par l'extrusion. Les modèles ainsi établis sont utiles pour (1) calculer la pression nécessaire pour chaque matériau développé afin d'atteindre la vitesse d'impression désirée, et ce, à un moment connu après le mélange du matériau, ainsi que (2) prévoir la vitesse maximale d'impression correspondant à la capacité limite d'un système d'extrusion donné. Il est prévu que les caractérisations et les modèles présentés ici soient transférables du système d'extrusion mono-buse utilisé pour le développement des matériau au système industriel multi-buses, toujours pour un diamètre de buse de 250 µm. Pour le système utilisé dans cette étude, les vitesses maximales atteintes sont de l'ordre de $110 - 175$ mm.s^{-1} pour une pression de 4,54 MPa. Les vitesses d'impression obtenues ici sont plus de trois fois celles publiées dans la littérature pour des composites thermodurcissables mis en forme par écriture directe.

Les fonctionnalités visées pour le matériau final sont aussi évaluées séparément pour chacune des trois formulations contenant des microsphères creuses de verre et de la nano-silice. Pour l'absorption du bruit, des sections d'échantillon sont imprimées, puis superposées dans un tube de Kundt pour caractériser les propriétés acoustiques. Des coefficients d'absorption quasi-parfaits ($\geq$0.98) dans l'intervalle de fréquences de 2100 à 2700 Hz sont mesurés en imprimant la géométrie nominale sélectionnée pour la preuve de concept (distance minimale entre deux filaments de 300 µm, hauteur d'empilement de $\sim$25 mm). Les coefficients d'absorption et les taux d'amortissement acoutiques expérimentaux sont comparables aux valeurs qui ont été simulées employant le modèle de Johnson-Champoux-Allard-Lafarge.

En ce qui concerne l'abradabilité, des indicateurs tirés de la littérature sont mesurés pour les meilleures formulations. Ces indicateurs, constitués de la micro-dureté, de la résistance à l'arrachement et du taux de rupture cohésive, permettent une comparaison qualitative, bien qu'indirecte, entre l'abradabilité des matériaux développés et le produit commercial de base. Il est montré que les meilleures formulations se rompent dans un mode d'arrachement en grande partie cohésif à l'instar du produit commercial, mais que leur dureté et leur résistance mécanique est nettement supérieure, ce qui n'est pas désirable pour l'application visée. Ces mesures portent à croire que le taux de porosité créé par le microsphères creuses soit insuffisant dans les meilleures formulations pour que leur abradabilité soit comparable à celle du produit commercial.

Les trois formulations retenues sont prometteuses pour imprimer à haute vitesse des revêtements abradables capables d'atténuer le son sur des grandes surfaces comme les carters-moteur. Des expériences additionnelles sont nécessaires pour identifier un compromis entre les propriétés mécaniques, les performances fonctionnelles et l'aspect de fabrication des meilleures formulations.

ABSTRACT

The democratisation of travel gives easy access to both remote regions and densely populated areas, bringing them closer than ever to a growing number of passengers. Considering the environmental challenges arising from increased travel, new international policies impose severe restrictions on commercial aviation with respect to noise pollution and greenhouse gas emissions. These policies push aircraft component manufacturers to design products that are not only lighter but also more energy efficient to reduce aircraft fuel consumption.

Optimising the efficiency of high-bypass turbofans is paramount for reducing harmful aircraft emissions. Within the fan region, fuel consumption may be optimised by limiting blade tip air losses. To this end, coatings of abradable thermosetting composites are applied to the inner surface of the fan case to reduce the functional clearance between the blades and the shrouding. In addition, giving a second functionality to the abradable coatings could address noise pollution regulations. The abradable coating would have to be arranged in a porous structure to absorb the noise emitted by the fan. Additive manufacturing is a suitable method for shaping such noise-abating coatings due to their intricacy and fine detailing. However, there is no one material on the market that can simultaneously perform both abradable and sound absorption functionalities. It is therefore the aim of this project to develop multifunctional thermosetting composite materials that can be shaped by additive manufacturing, here by high-speed direct ink writing.

The commercial abradable product for the fan case used by Safran, the industrial partner of this project, is not printable due to the high filler loading in the material (hollow glass microspheres). Hence, the development of the new multifunctional material is based on the base resin of the commercial product, without fillers. Different loadings of microspheres and/or fumed silica nanoparticles are added in order to obtain blends which can be extruded by the 250 µm nozzles, and to enable printed shape retention until the part cures. Electron microscopic observations and X-ray imaging scans are used to study the shape of extruded filaments as well as filler integrity. Three best blends are retained for further testing based on their ability to keep a circular filamentary shape and the integrity of microspheres after printing. Rheological characterisations yield a complete flow behaviour model, which combines the effects of polymerisation and shear rate induced by the extrusion process. The models thus established find application for (1) calculating the pressure required for each developed blend to achieve a desired print speed at a known time after material mixing, and (2) predicting the speed maximum printing speed corresponding to the limiting pressure of a

given extrusion system. It is assumed that the characterisations and models presented herein will be transferable from the single nozzle extrusion system used for material development to the industrial multi-nozzle system (250 μm nozzle diameter). With the dispensing system used in this study, the maximum printing speeds reached $110 - 175 \text{mm.s}^{-1}$ at a pressure of 4.54 MPa. The printing speeds obtained are over three times those published in the literature for thermosetting composites printed by direct ink writing.

Both abradable and sound absorption functionalities desired for the final material are also assessed separately for each of the three best blends containing glass microspheres and/or fumed silica nanoparticles. For sound absorption, sample sections are printed, and stacked vertically in a Kundt's tube for acoustic characterisation. Near-perfect absorption coefficients ($\geq$0.98) in the range of frequencies between 2100 and 2700 Hz are measured for the printed geometry selected for the proof of concept (minimum distance between adjacent filaments of 300 μm, total stacking height of $\sim$25 mm). Sound absorption coefficients and experimental acoustic damping rates are comparable to the values simulated using the Johnson-Champoux-Allard-Lafarge model.

With respect to abradability, indicators drawn from the literature are measured for the best blends. These indicators, i.e. micro-hardness, pullout strength and cohesive failure percentage, provide a qualitative comparison between the abradability of the developed materials and the commercial abradable product. The best blends fracture in a cohesive mode similar to the commercial product, but their hardness and strength is significantly higher, which is not desirable for the target functionalities. Hence, mechanical properties suggest that the porosity created by the hollow microspheres is insufficient in the best blends to mimic the abradability of the commercial product.

The three best blends are promising for the high-speed printing of large area sound absorbing abradable coatings. Some characterisation remains to be completed in order to achieve a compromise between the mechanical properties, functional performance and manufacturing considerations of the best blends.

TABLE OF CONTENTS

LIST OF TABLES

LIST OF FIGURES

LIST OF SYMBOLS AND ACRONYMS

ACARE	Advisory Council for Aeronautics Research in Europe
AM	Additive Manufacturing
APS	Atmospheric Plasma Spray
DIW	Direct Ink Writing
DMA	Dynamic Mechanical Analysis
DSC	Differential Scanning Calorimetry
DSZ	Dysprosia-stabilized Zirconia
FS	Fumed Silica
GM	Glass Microspheres
HVOF	High Velocity Oxygen Fuel
ICAO	International Civil Aviation Organisation
JCAL	Johnson-Champoux-Allard-Lafarge
PJ	Petroleum Jelly
SEM	Scanning Electron Microscopy
TGA	Thermogravimetric Analysis
YSZ	Yttria-stabilized Zirconia
μCT	Micro-computed Tomography
a, a_1, a_2, b, b_1, b_2	Viscosity change parameters
A_e	Target pore area from a top view
A_o	Nozzle outlet area
A_p	Average pore area from a top view (printed)
A_p^f	Average filament cross-section area (printed)
$A_1,\ A_2$	Autocatalytic pre-exponential factors
$c_1,\ c_2$	Shape fidelity weights
D_e	Nozzle inlet diameter
D_o	Nozzle tip inner diameter
$E_1,\ E_2$	Autocatalytic activation energies
f_p	Peak absorption frequency
G'	Shear storage modulus
G''	Shear loss modulus
H	Heat flow
h_e	Expected interlayer height
h_p	Printed interlayer height

K	Consistency index
K_a	Apparent consistency index
k_1, k_2	Autocatalytic rate constants
L	Capillary length
l	Average cross-section perimeter of a printed filament
m_1, m_2	Autocatalytic reaction orders
n	Flow behaviour index
n_a	Apparent flow behaviour index
P_{atm}	Barometric pressure
P_e	Extrusion pressure
Q	Volumetric flow rate
Q_c	Volumetric flow rate through a cylindrical nozzle
Q_T	Volumetric flow rate through a tapered nozzle
R_g	Universal gas constant
T	Temperature
T_g	Glass transition temperature
T_p	Peak exotherm temperature
t	Time after mixing
u	Printing speed
α	Absorption coefficient
α_p	Peak absorption coefficient
$\bar{\alpha}$	Average absorption coefficient
ΔH	Partial heat of reaction
ΔH_0	Total heat of reaction
ΔP	Extrusion pressure gradient
ζ	Damping ratio
η	Shear viscosity
η_0	Rest shear viscosity
η_a	Process-related viscosity
η^*	Complex viscosity
θ	Half cone angle
Γ	Shear-thinning curvature parameter
γ	Shear strain
$\dot{\gamma}$	Shear rate
$\dot{\gamma}_N$	Newtonian wall shear rate
$\dot{\gamma}_w$	Corrected wall shear rate

λ	Material relaxation time
ξ	Degree of cure
ρ	Cured material density
τ	Wall shear stress
τ_{YS}	Yield shear stress
τ_0	Yield shear stress at rest
ϕ	Porosity
ψ	Weighted printability index
ψ^f	Filament printability index
ψ^{side}	Side view printability index
ψ^{top}	Top view printability index
ω	Oscillatory frequency

LIST OF APPENDICES

CHAPTER 1 INTRODUCTION

1.1 Project context

Amid growing environmental concerns, the International Civil Aviation Organisation (ICAO) created the Committee on Aviation Environmental Protection, tasking it with the modelling of environmental trends in aircraft noise pollution and CO_2 emissions [1]. The committee helps the ICAO Council in drafting new policies, most notably setting industry-wide CO_2 emission and noise level targets. A regional initiative in Europe, named the Advisory Council for Aeronautics Research in Europe (or ACARE), was mandated by the European Commission to manage the research and development activities necessary to achieve the objectives set forth by the ICAO. In an effort to mitigate the negative impacts of civil aviation, the ACARE therefore established the need for new technologies that would allow to reduce CO_2 emissions by 75 % per passenger per kilometre, and the perceived noise of flying aircraft by 65 %, relative to 2000 levels in 2050 [2].

Although complying with international standards is a responsibility bestowed upon system integrators (e.g., Airbus and Boeing), original equipment manufacturers have a key role to play in this matter. As the propulsion group is responsible for most of an aircraft's polluting emissions [3], engine manufacturers such as Safran, the industrial partner of this project, are keen to implement innovative solutions to their designs to palliate environmental emissions. Engine efficiency has consequently remained a priority in the aerospace industry.

Aircraft engine fuel consumption can be reduced by using abradable materials. Such materials are applied in the form of coatings to minimise the gap between rotating blade tips and the core shroud or the fan case. Tightening the operating clearance ensures a reduction of blade-tip losses, thus boosting engine efficiency [4]. Sacrificial abradable coatings are preferentially worn by engine blades initially when the engine is first used, to accommodate inherent geometry scattering from the manufacturing process, and then to prevent the blade tips from impacting the shroud or fan case, for example during in-flight manoeuvres [5].

The work herein focuses on the abradable material used for the fan case of the LEAP-1A engine, as per the specifications of the industrial partner of this project. Thermoset-based abradable materials, typically an epoxy resin matrix is filled with hollow glass microspheres (GM), are a widespread solution for coating fan cases. GM are used for their positive contribution in composite weight reduction, chemical resistance, thermal conductivity as well as abradability and wear properties [6]. Polymeric abradable materials are usually applied with a shape knife or by thermal spraying [7]. However, a manual application is a long, laborious and expensive process [8]. In addition, manual spreading is prone to introducing surface de-

fects to the coating, such as tears and punctures, which require subsequent filling and rework. An automated application technique for abradable coatings could address current industrial production limitations.

Additive manufacturing (AM), or 3D printing, has been gaining momentum in the past years as it enables the layer-by-layer fabrication of structures featuring complex geometries often not achievable by traditional machining [9]. The use of AM as a fabrication technique for polymeric abradable materials would allow to optimise the production cycle of sacrificial coatings by consistently controlling their thickness and introducing other functionalities like sound absorption. Abradable material systems currently available are incompatible with AM mainly due to a lack of post-printing shape retention. Hence, developing a new abradable material for AM is to one of the main objectives of the Industrial Research Chair on Additive Manufacturing of Organic Matrix Composites (FACMO). More broadly, the FACMO chair aims to develop composite materials and the associated manufacturing technologies to create high-performance composite structures for the aerospace industry.

To meet the noise reduction objectives set by the ACARE, the abradable materials developed in this work are also intended to reduce noise emissions. The development of this noise reduction functionality falls in line with the objectives of the Industrial Research Chair on Multifunctional Passive Acoustic Treatments for Turbofan Composite Structures (TAPPIS). The TAPPIS group aims to develop structures able to absorb and dissipate the noise produced by aircraft engines. Therefore, the work herein addresses objectives of both the FACMO and TAPPIS chairs. To that end, porous abradable coatings will be deposited onto a thermoplastic noise-abating sandwich structure, itself printed on the inner side of the fan case. The multifunctional abradable coating will effectively act as a gateway structure into sound absorbing cavities, yet still providing protection for fan blade tips and aerodynamic sealing. Such a lightweight design would complement other sound reduction solutions, such as *hush kits* [10], airframe fairings [11], or aero-acoustic nacelle designs such as that of the Boeing 787's General Electric's GEnx engines which feature the recognisable trailing edge chevrons [12].

The use of AM is further supported considering the increasing adoption of this technology by the aerospace industry, which accounts for 12% of AM applications [13]. For example, in 2017, Airbus started fitting a titanium bracket produced by Selective Laser Melting onto the engine pylons of the A350-XWB [14]. Perhaps the most widely cited application of AM in aerospace remains that of General Electric's fuel injector nozzles, which are now being produced by Direct Laser Melting, thus crossing from a twenty parts welded assembly to just a single part. As for polymer processing, brackets, air ducts, interior panel and fixtures are just a few examples of AM success stories in the civil aviation sector [15, 16].

1.2 Research objectives

The need for a new process for applying abradable materials being defined, the following two objectives must be met at the outcome of this project:

O1: Develop a thermosetting abradable material compatible with a high-speed direct ink writing printing process and a multinozzle printing system.

O2: Evaluate the bulk mechanical properties of the new material and assess the predictability of acoustic properties for printed structures.

1.3 Thesis outline

This dissertation is organised into five sections as follows. Chapter 2 presents the literature review with a focus on abradable materials, additive manufacturing, as well as a selection of topics related to polymer rheology and process modelling. Chapter 3 outlines the general methodology adopted to attain the aforementioned objectives and the relevance of the paper with respect to the objectives. Chapter 4 is devoted to most of **O1**, which was the main focus of this project. As such, Chapter 4 contains the scientific paper encompassing the development of the new abradable material. Chapter 5 complements **O1** with unpublished data and gathers preliminary results for **O2**, related to the mechanical properties of the developed abradable materials. Chapter 5 also offers a general discussion addressing the project as a whole, together with a the main limitations of this study. Lastly, the main results will be summarised and future works will be enumerated in Chapter 6.

CHAPTER 2 LITERATURE REVIEW

2.1 Turbofan engine architecture

A turbofan engine provides thrust to the aircraft in the form of a reaction force resulting from accelerating the inlet air flow. Figure 2.1 (a) presents a schematic of the components employed in the basic thermodynamic cycle of a high-bypass turbofan. The air flow enters on the left side by the fan and is directed through a series of low and high pressure compressor stages, alternating between rotors and stationary guide vanes which together increase the pressure of the medium. In the combustion chamber, fuel is injected into the highly pressurised air, and the mixture is ignited, thus releasing heat. The gases expand and accelerate into the subsequent high and low pressure turbines to extract and transfer work to a shaft, which in turn drives the compressor rotors to pump more air in. The remaining available energy is ejected at the back of the engine by the nozzle, whereby thrust is generated [17].

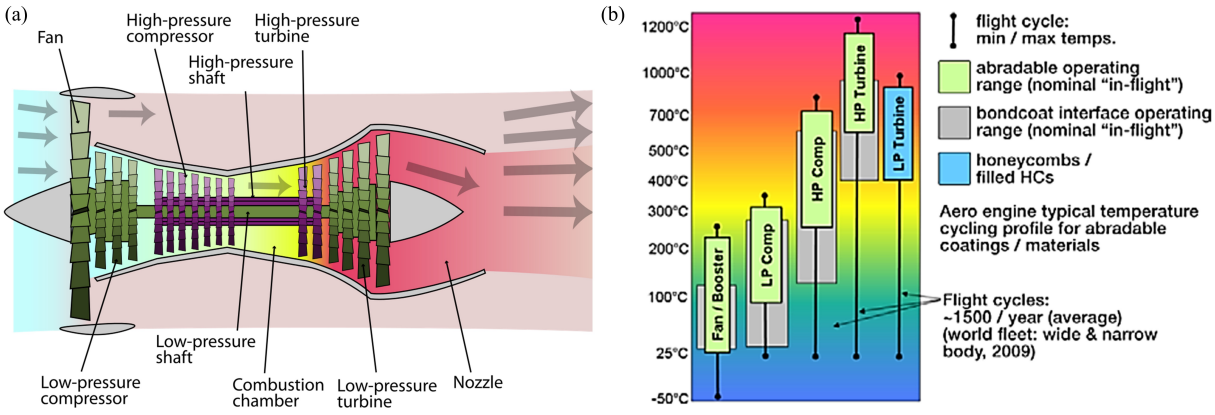

Figure 2.1 (a) Architecture of a modern high-bypass turbofan aero-engine [18]. (b) Typical operating temperature range of the main stages of a turbofan engine (LP for low pressure; HP for high pressure) [17].

Operating temperatures shown in Figure 2.1 (b) vary from -50 to 300 °C across the fan and low pressure compressor and increase up to 1200 °C in the high pressure turbine located directly downstream of the combustion chamber. The material selection for each stage must take into account those temperatures to avoid material degradation, or active cooling solutions must be implemented for the engine to withstand the extreme temperatures encountered in the combustion chamber.

Some of the inlet air flow bypasses the core of the engine through a duct to cool high-temperature components, in parallel of the combustion process. For example the LEAP-1A

engine from CFM international has a bypass ratio of 11:1, that is, for every 1 kg of air supplied to the core, 11 kg of air will circulate in the bypass duct [19]. The separate air stream also contributes additional thrust (up to 70 % of the total engine output during cruise [20]). The mixing of high-speed exhaust gases with the lower-speed bypass air in the nozzle leads to a considerable noise reduction [21].

2.2 Abradable materials

Parasitic air leakages between the stationary fan case (or engine core shroud) and rotating blades prevent an optimal extraction of work from the air flow, and thus are highly detrimental to overall engine efficiency by increasing fuel consumption [22]. Abradable materials are used as sacrificial coatings in aircraft engines in the form of seals to limit aerodynamic blade tip losses between subsequent compressor or turbine stages [23]. Figure 2.2 (a) illustrates how static abradable coatings can be worn through fan blade contacts (rubs) to improve efficiency. Tight operating clearances inevitably result in interactions between the stationary and rotating engine components due to shroud distortions caused by circumferential variations of heat gradients and gyroscopic forces during certain manoeuvres, rotor misalignment, unbalanced parts, blade creep deformation, or thermal and centrifugal dilatations [22, 24, 25]. Abradable coatings also avert catastrophic flow reversals caused by leakage-induced blade tip vortices which generate a suction effect in the direction opposite of the main air stream [26]. Abradable seals therefore allow for the geometrical adaptation of the aerodynamic gap so to mitigate potential structural damages to the blades while locally restricting air losses [5, 23].

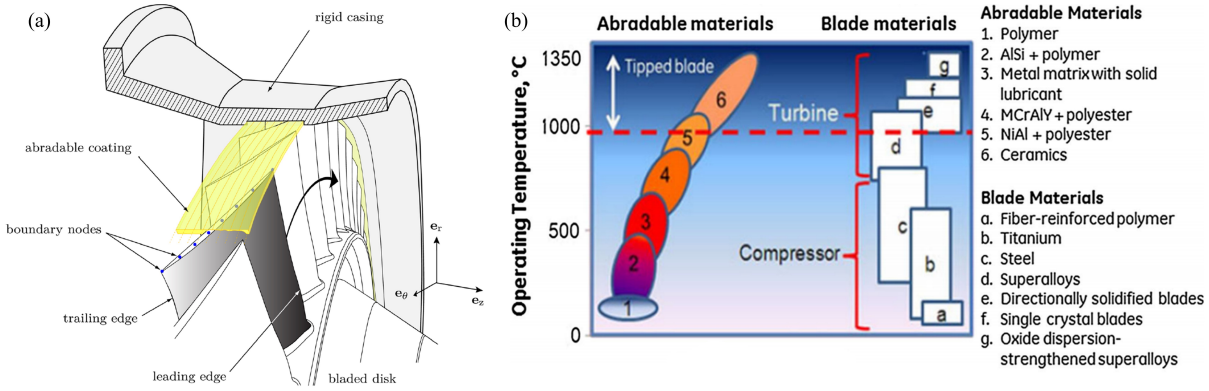

Figure 2.2 (a) Schematic of the abrasion phenomenon. A layer of the abradable coating is removed from the fan case by the action of the rotating blades [27]. (b) Categories of abradable and blade materials depending on engine stage operating temperatures [28].

Abradable sealing performance is considered optimal in compressors for operating gaps below 2 % of the blade tip chord, and becomes unacceptable for gaps above 5 % [25, 29]. In

the high pressure turbine, decreasing the operating clearance by 0.0254 mm can reduce the specific fuel consumption by 0.1 % [26, 30]. A gap reduction of 50 % has also been cited to lead to a 2 % increase in efficiency [17]. In terms of absolute values, for example in the case of the LEAP-1A engine, tightening the gap from 2 mm to 1 mm only between the 1.98 m diameter fan blade and shroud would lower fuel consumption by decreasing the fan efficiency losses from 0.2 % to 0.1 % [31]. For airlines in America, the efficiency gain represents annual savings of USD 20 million [26]. Abradable materials thus play a key role in optimising aircraft fuel consumption, and by extent reducing the environmental impact of commercial aviation.

2.2.1 Inorganic matrix abradable materials

Across most of the engine, prohibitive operating temperatures in the range of 200 to 1500 °C require the use of inorganic matrix abradable materials. Figure 2.2 (b) shows that for compressor stages, metallic matrix abradable materials are typically used up to approximately 800 °C (groups 2-4). For the low and moderate temperatures stages of the compressor, abradable materials are comprised of an aluminium-based matrix alloyed with silicon (AlSi) and solid lubricants such as graphite, hexagonal boron nitride (hBN) and bentonite [28,32,33] are added as a release agent to induce friability to the matrix. In the high pressure compressor and low pressure turbine where temperatures span 800 - 1000 °C, metallic abradable materials (groups 4 and 5) are applied, for example MCrAlY alloys or nickel/cobalt-based alloys. Within the hottest regions of the engine, an Yttria or Dysprosia-stabilized Zirconia ceramic matrix (YSZ and DSZ, respectively) substitutes metallic alloys [33, 34]. Modified thermal barrier coatings, such as Hastelloy X, are employed for applications beyond 1200 °C in the vicinity of the high pressure turbine [34,35]. The addition of non-metallic fillers to abradable materials has also been demonstrated to prevent galvanic corrosion caused by metal to metal contact when the aircraft is not operated, for example in Auxiliary Power Units [17, 36].

2.2.2 Organic matrix abradable materials

Organic matrix abradable materials ensure blade protection and aerodynamic sealing from the entry fan through the low pressure compressor [26, 37]. Although epoxy-based materials with micro-fillers are commonly applied at the engine entry region, published characterisation and development data is scarce; patents constitute the most part of publicly available information. A broad range of fillers are known to impart abradability properties in epoxy matrices: molybdenum disulfide, cerium fluoride, polytetrafluoroethylene, boron nitride, graphite, talc, tungsten disulfide, calcium fluoride [38], phenolic resin hollow microspheres [37, 39, 40], hollow glass microspheres [41], or polytetrafluoroethylene fillers and a small percentage of alumina-silica microspheres and fibres [36]. Some products use a silicone

matrix with nano-sized fumed silica [42] or glass microbeads [43]. Metallic fibres may also be incorporated to the material in order to carry away frictional heat generated during a rub event between the abradable seal and the blade. Heat dissipation is an important concern for fan blades made of composite layers bonded by adhesives which may dissociate at higher temperatures [38].

2.2.3 Abradable coating design criteria

From a mechanical standpoint, low-temperature abradable materials must be brittle in order to be removed preferentially in the case of rub events, without accumulating on the tip of the blades, smearing over the coating or damaging the blade [44]. Additional considerations for material design or selection include:

1. Resisting the eroding effect of ingested particles, such as ice, dirt and dust, for low temperature abradable materials, as well as wear and combustion debris for downstream abradable seals [22];

2. Resisting oxidation caused by high-velocity oxygen-rich gas flowing through the first compressor stages of the engine, plus high-temperature gasses in the turbine stages [45];

3. Resisting corrosion in the high-moisture and sometimes saline conditions encountered during low-altitude flight or aircraft rest [25];

4. Exhibiting a coefficient of thermal expansion compatible with the supporting substrate to prevent seal debonding or fracture from a misfit strain [25, 46, 46];

5. Sustaining repeated loading cycles at the seal-substrate interface (e.g. fan case geometrical distortions and resonant vibrations) [47];

6. Absorbing the heat generated by rub events [38];

7. Forming wear debris no larger than 0.1 mm to prevent downstream stator or rotor damage [25, 26, 48];

2.2.4 Coating application methods

Thermal spraying techniques are most common for applying inorganic matrix abradable coatings [7]. In Figure 2.3 (a), a schematic of the high-velocity oxygen fuel (HVOF) process shows how a powder feedstock is partially melted and projected at supersonic speeds onto a substrate by a burning gas stream [49, 50]. The atmospheric plasma spray (APS) method in Figure 2.3 (b) operates using an arc formed between an anode and a tungsten cathode

which ionises the gas stream thus developing a plume of plasma. The powder feedstock is injected into the plasma plume and then sprayed onto the coating substrate [33, 49]. Both the HVOF and APS thermal spraying techniques admit high melting points metallic and ceramic matrix powders, in order to produce high-temperature strength abradable coatings. Compatible feedstock inculdes AlSi with polyester [26], MCrAlY - boron nitride - polymer mixtures, YSZ and DSZ [17] and hastelloy [35]. Due to higher impact speeds, the HVOF process yields coatings with less porosity than the APS method. Selecting the appropriate method depends on the thermal stability of the substrate as APS allows to keep substrates at temperatures as low as 50 °C [50]. Many other methods such as flame spray (for powders) or the analogous less efficient diffusion brazing (for wire feedstock) accommodate abradable materials in the form of nickel or cobalt alloys [17, 26].

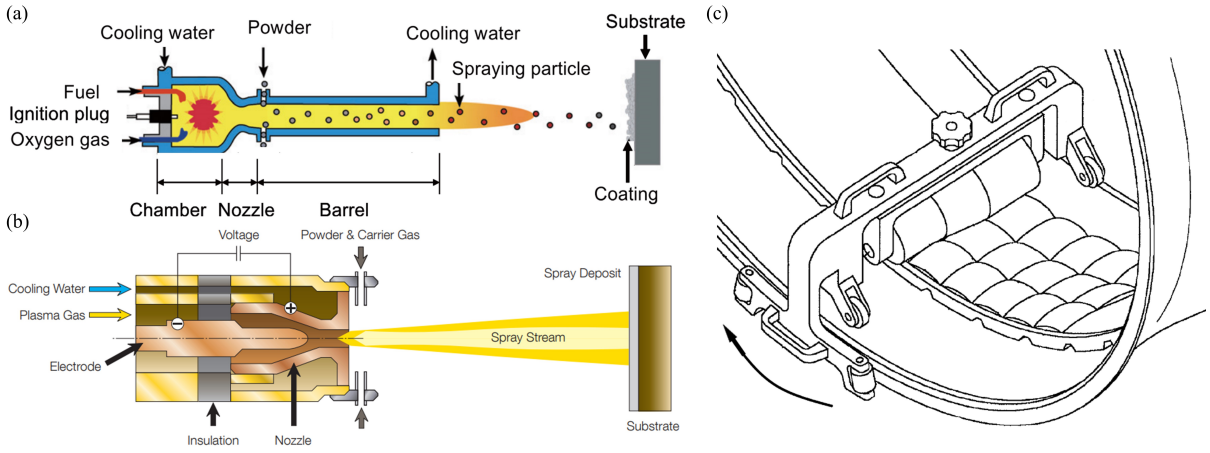

Figure 2.3 (a) High-velocity oxygen fuel thermal spray [51] and (b) Atmospheric plasma spray [49] methods for applying inorganic matrix abradable materials on the engine core shroud. (c) Jig for applying polymer matrix abradable coatings in the fan region, adapted from [8].

In the case of low temperature polymer matrix abradable materials, coatings are either cast or applied manually by means of successive roughing and finishing passes with a trowel [26]. Coating application by trowel is laborious and inefficient, due to potential coating material being torn away during passes and forming surface defects [52]. Figure 2.3 (c) presents a more efficient method for casting polymer matrix abradable coatings for the fan region with the aid of a patented jig [8]. Balls of polymeric abradable paste are first placed on the fan case. The jig is then mounted as shown in Figure 2.3 (c) and rolled over radially to spread the abradable coating using the edge flanges of the fan case as guide rails. A uniform distribution of coating is obtained by several passes of the tool over a given region and decreasing the height of the rollers in relation with the coating substrate. In some instances,

a filled metallic honeycomb liner configuration is used to provide structural support to the composite seal [7, 26, 52]. A honeycomb, made of Nomex for example, may also be used for absorbing part of the noise emitted in the fan region. In such case, the paste material would be rolled onto the honeycomb using the jig in Figure 2.3. Table 2.1 summarises abradable material groups, their respective location in the engine and application method.

Table 2.1 Summary of abradable materials used in aero-engines with suitability for different engine components and application method

Abradable material type	**Service temperature [°C]**	**Engine component**	**Manufacturing method**	**Ref.**
Epoxy or Silicone matrix + organic or inorganic fillers	<250	Fan and LP compressor	Cast or with a trowel (paste)	[8, 18, 26, 36–40, 42, 43, 52]
Metal matrix AlSi or MCrAlY + solid lubricants + polymer	250-800	HP compressor and LP turbine	HVOF or APS (powder)	[7, 18, 28, 32, 33, 33, 49–51]
Nickel/cobalt-based alloys + polymer	800-1200	HP turbine	Brazing or flame spray (wire/powder)	[17, 18, 26, 33]
Ceramic matrix YSZ or DSZ, Hastelloy	800-1500	HP turbine	HVOF or APS (powder)	[7, 17, 18, 34, 35, 49, 50]

2.2.5 Quantifying abradability

Abradability is a tribological property describing the ability of a coating to detach from the bulk material after being scratched [25], i.e. it is the measure of the ease with which a material can be removed [34, 53, 54]. Many simple indirect methods for quantifying abradability have been proposed in the literature, mostly through the evaluation of micro-hardness or scratch tests, as shown in Figure 2.4 (a) and (b), respectively [53, 54]. However, micro-hardness tests merely give an indication of material abradability; to a lower hardness corresponds a higher degree of abradability [25, 35]. A Rockwell HR15Y scale is usually used for evaluating the hardness of inorganic matrix abradable coatings [32, 35]; some authors have argued that Vickers hardness is more appropriate for abradable materials as Rockwell hardness includes a contribution from the coating substrate [34, 37, 53, 54]. Rockwell HR15Y scale values typically range from 35 for nickel/cobalt matrix abradable materials to 75 AlSi abradable materials, or up to 85 for YSZ and DSZ ceramic matrix materials [17, 35, 55]. In the case of organic matrix abradable materials, Shore A and Shore D tests are more suitable for elastomer matrix and thermoset matrix composites, respectively, as these materials are very soft compared to metal matrix materials [38, 56], although a Vickers scale has been used for an epoxy matrix abradable in [53].

Scratch tests quantify a specific energy - or Progressive abradability hardness - which is measured by the reaction forces of a stylus ploughing through a controlled thickness of coating, as presented in Figure 2.4 (b). The specific energy needed to produce a groove is obtained through the ratio of work done by the indenter over the volume of the material removed; a higher ratio suggests a lower abradability as more energy is required to remove a unit volume of coating [54]. Progressive abradability hardness has a strong correlation with mechanical properties such as stiffness and ultimate stress, hence abradability may also be gauged by tensile and compression tests, although these properties in of themselves do not guarantee a good tribological performance [25, 53, 57].

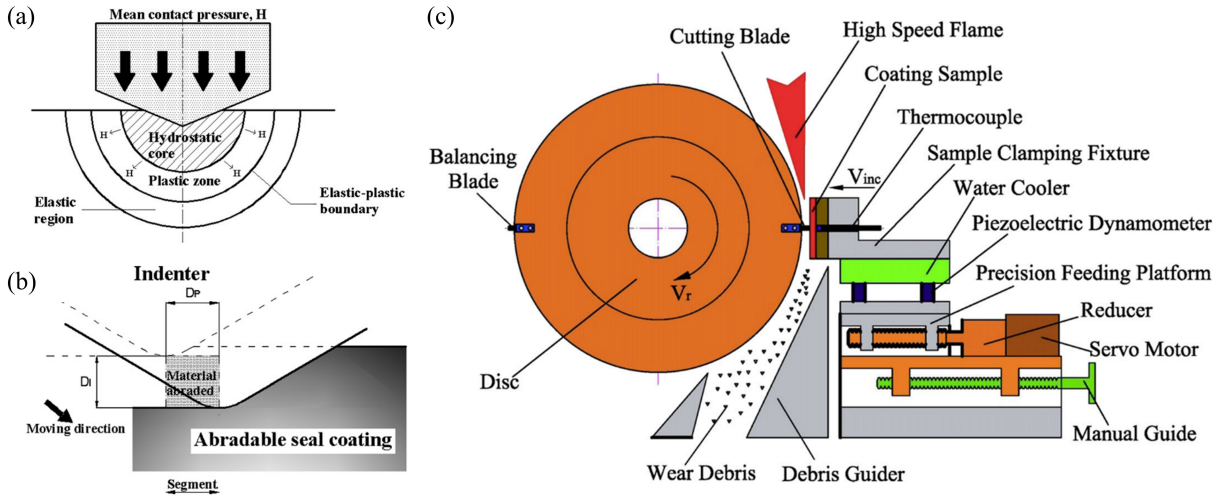

Figure 2.4 (a) Deformation mode encountered in a Vickers scale micro-hardness test for a nickel matrix abradable [53]. (b) Abradable coating removal by a moving indenter during a scratch test [54]. (c) Functioning principle of an abradability test bench simulating in-service conditions [32].

A more accurate physical representation of the material removal phenomenon in the engine requires specialised rigs to estimate abradability. In Figure 2.4 (c), strip of blade material is mounted onto a rotating disc, and a flat abradable coupon (specimen) is slid at a predetermined pace - or incursion rate - towards the blade. The depth of wear penetration is called incursion depth, and it is also a controlled test parameter. Depending upon the targeted stage of the engine, the coupon will be simultaneously subjected to wear and heating by a high-velocity stream of gas to simulate in-service conditions. During the incursion, contact forces between the coupon and the blade are gathered using a piezoelectric dynamometer, or a transducer that reads the frictional torque data on the test rig. The abradability property is computed by the ratio of energy per unit mass or volume used to wear the abradable coating, similar to the progressive abradability hardness method. The literature provides a broad

range of incursion depths (50 to 2000 μm), incursion rates (1 to 3000 μm.s^{-1}) and blade tip speeds (30 to 600 m.s^{-1}) [17, 25, 32, 35, 47, 55]. The choice of test parameters lies within the expected in-service conditions of temperature, desired seal gap height, blade and coating materials, etc. Selecting an excessive incursion rate would result in material transfer to blade tip, or undesirable blade grooving. In the case of the LEAP-1A engine fan, the maximum fan blade tip speed is 400 m.s^{-1} (or ∼3900 rpm), and temperatures reach 60 °C [58].

2.3 Additive manufacturing for thermoset composites

Additive manufacturing has found many applications in fields such as energy storage, tissue engineering, and rapid prototyping [59]. Versatility and design freedom in AM are increasingly exploited together with topology optimisation to produce structural parts that are lighter than machined equivalents [60]. The possibility to create part geometries and functionalities unattainable without AM is often cited as the most important advantage to justify the use of this technology [9, 61, 62]. The core principle behind building parts with AM is the successive stacking of material layers using computer-controlled stages, opposite to conventional manufacturing methods which remove layers from a raw bulk material. Prior to printing, a virtual part model is first sliced to extract the disposition of material in each layer. Once sliced, a G-code specifying the displacement of robotic stages and the control of accessories is obtained and fed to the AM system for printing.

At present, AM of thermosetting composites is mostly limited to extrusion-based and vat photopolymerisation technologies [61, 63, 64]. The latter requires fabrication systems equipped with ultraviolet (UV) lasers for *in situ* curing, for example in stereolithography and continuous light processing, and is beyond the scope of this work because of technical challenges arising from printing on a non-planar substrate. On the other hand, extrusion-based AM methods are relatively simpler to implement as they only necessitate an extrusion apparatus driven by either pneumatic or mechanical action (or both), and sometimes a material feeding system. In some cases however, *in situ* curing through UV, microwave or infrared radiation must be added to prevent printed shape loss [65–67]. Technologies making use of material extrusion at room temperature, i.e. no feedstock melting, are named direct ink writing (DIW).

2.3.1 Direct ink writing technologies

In the DIW process, 3D parts are shaped layer by layer by selectively depositing a continuous filament onto the substrate in the fashion of Figure 2.5 (a-b). Horizontal platforms move the substrate to the correct position, while the vertical axis places the tip of the dispensing nozzle at the correct height. Once a layer is completed, the material reservoir

(syringe) and the affixed nozzle are shifted upwards and the next layer is printed. The procedure is repeated until the full desired height is attained as in Figure 2.5 (c). Printing parameters such as the nozzle diameter, filament spacing, extrusion pressure, layer height and linear displacement speeds can be modified to tailor the process to the targeted application.

Material properties are also a paramount consideration in DIW. Specifically for thermoset composites, viscoelastic materials are preferred to ensure smooth extrusion [59,61,68]. Typical extrusion mechanism are piston-driven, air-driven or screw-driven depending upon the rheological properties of the extruded material [69]. For example, printing solid-like materials and viscoelastic pastes requires a physical contact to overcome the friction of the feedstock at the syringe wall. Viscoelastic materials are therefore extruded either with a plunger (actuated pneumatically or by a motor) or an Auger screw, like in Figure 2.5 (d,e), respectively. Printing systems using the pressure exerted by compressed air such as in Figure 2.5 (f) are reserved for liquid-like materials with lower opposing frictional forces [70]. Rheological properties will be explored more carefully in Section 2.4.

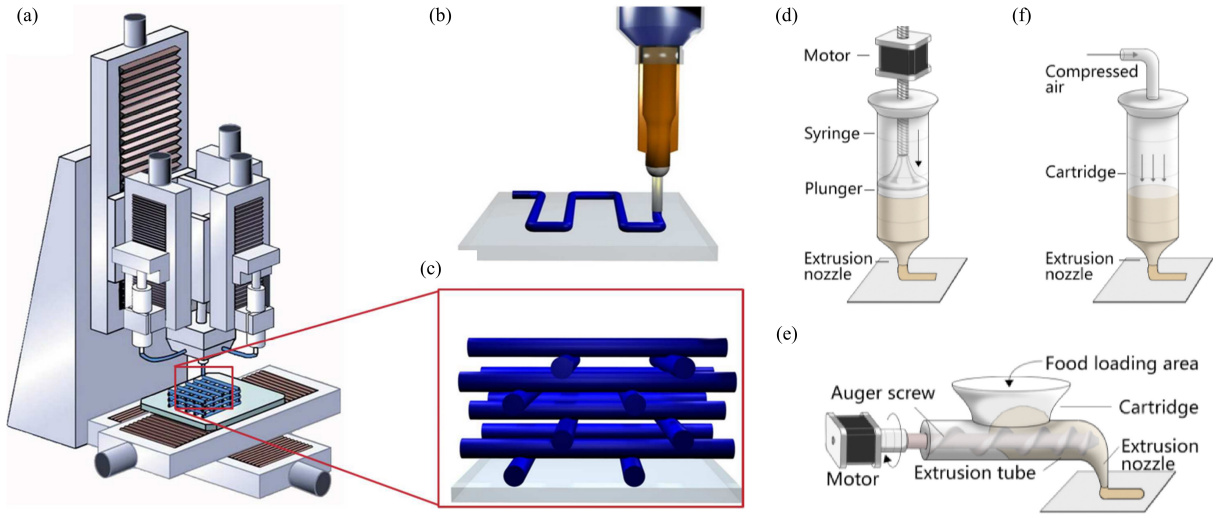

Figure 2.5 Direct ink writing additive manufacturing of porous samples: schematics of (a) a robotic positioning system for material extrusion, (b) a filament extruded onto a flat substrate, and (c) an enlarged view of a porous structure [71]. Extrusion mechanisms: schematics of a (d) piston-driven, (e) air-driven, and (f) screw-driven system, adapted from [70].

As synthesised in Table 2.2, many thermoset composites have been formulated for DIW, commonly using epoxy as a matrix. In most cases, either fumed silica or nanoclay particles introduced into the resins enable printed shape retention, in addition to reinforcing fillers. Printing speeds are limited to 40 $mm.s^{-1}$ with current technology, and successful printing of thermoset composites without post-curing and using nozzle tip diameters below 300 µm have been seldom reported in the literature.

Table 2.2 Literature summary of printable thermoset composites using DIW, with printing speeds, extrusion pressures, nozzle type and technology

Year	Material	Main process parameters	Nozzle type	Technology	Ref.
2010	UV-curable polyurethane, filled with 0.5 wt.% C-SWNTs and 5 wt.% fumed silica	$\sim$1mm.s^{-1}	150 µm cylindrical	Ultraviolet-assisted DIW	[65]
2014	Epoxy + nano-clay platelets + DMMP, reinforced with silicon carbide whiskers and/or milled carbon fibres up to 31 vol.%	Not reported	200-610 µm tapered	Piston-driven DIW	[68]
2017	Epoxy + glass spheres + fumed silica + acetone	<20 mm.s^{-1}, <0.7 MPa	150x350 µm rectangular	Air-driven DIW with acoustic focusing	[72]
2017	Epoxy + 15 wt.% fumed silica + 3-15 vol.% chopped carbon fibres	5-15 mm.s^{-1}, 0.15-0.4 MPa	250-610 µm tapered and 600 µm cylindrical	Piston-driven DIW with post-curing	[73]
2017	Epoxy + 5 wt.% MWCNT + 0-5.5 vol.% chopped carbon fibres	0.8 mm.s^{-1}	1.0 mm tapered	Piston-driven DIW with *in situ* microwave heating	[66]
2018	Epoxy/acrylate blend + 8 wt% of fumed silica	10 mm.s^{-1}, 0.23 MPa	250-410 µm tapered	Ultraviolet-assisted DIW	[74]
2018	Cyanate ester resin system + 20 wt.% fumed silica	<3 mm.s^{-1}, <0.48 MPa	250 µm tapered	Piston-driven DIW with post-curing	[75]
2018	Epoxy + up to 12.5 wt.% nanoclay platelets or + 10 wt.% fumed silica	<30 mm.s^{-1}	634 µm cylindrical	Piston-driven DIW	[76]
2019	Epoxy + 5 vol.% nanoclay + 0-5.5 vol.% chopped carbon fibres	15 mm.s^{-1}, <0.8 MPa	580 µm tapered	Piston-driven DIW	[77]
2020	Epoxy + 0-6.3 wt.% nanoclay + 5.5-10 wt.% Kevlar fibres	40 mm.s^{-1}	2.0 mm tapered	Vibration-assisted DIW (where a motor shakes the nozzle to avoid clogging)	[78]
2020	Epoxy + 0-40 vol.% milled carbon fibres + 1-10 vol.% nanoclay	40 mm.s^{-1}	600-864 µm tapered	Vibration-assisted DIW	[60]
2020	Epoxy + 56 vol.% GM + 15 vol.% short carbon fibres	40 mm.s^{-1}	0.58 mm tapered	Vibration-assisted DIW	[79]
2020	Epoxy + 1-10 wt.% fumed silica + 0-25 wt.% short carbon fibres	15-30 mm.s^{-1}, 0.15-0.4 MPa	440 µm tapered	Piston-driven DIW	[80]
2020	Epoxy + up to 58 vol.% GM	<10 mm.s^{-1}	1.2 mm tapered	Co-extrusion DIW	[81]
2021	Epoxy + 1-5 wt.% boron nitride nanobarbs + 5 wt.% fumed silica	30 mm.s^{-1}	577 µm tapered	Piston-driven DIW	[82]
2021	Polyimine resin system + 8-36 vol.% continuous carbon fibre bundle + nanoclay	<35 mm.s^{-1}	0.98-2.41 mm tapered	Continuous fibre DIW	[83]

2.3.2 Multifunctional abradable materials

Abradable materials have been presented until this point as purely bulk structures aiming at reducing the gap between the fan blades and the fan case to optimise fuel consumption. However, some previous developments have demonstrated the possibility of shaping epoxy-based abradable materials into porous sound absorbing structures to provide for coating multifunctionality [3]. To that end, a two-part commercial product (EC3524 B/A Blue, 3M, France) was modified by adding 8.5 wt.% of petroleum jelly and halving the hardener ratio recommended by the manufacturer. The porous structures in Figure 2.6 (a-d) were printed via piston-driven DIW using a 250 µm tapered nozzle with pore sizes (edge-to-edge filament distance) between 250 and 750 µm. Acoustic samples were printed as a square bounding volume, then cut into a cylinder of 30 mm diameter; thicknesses varied from 3 to 12 mm.

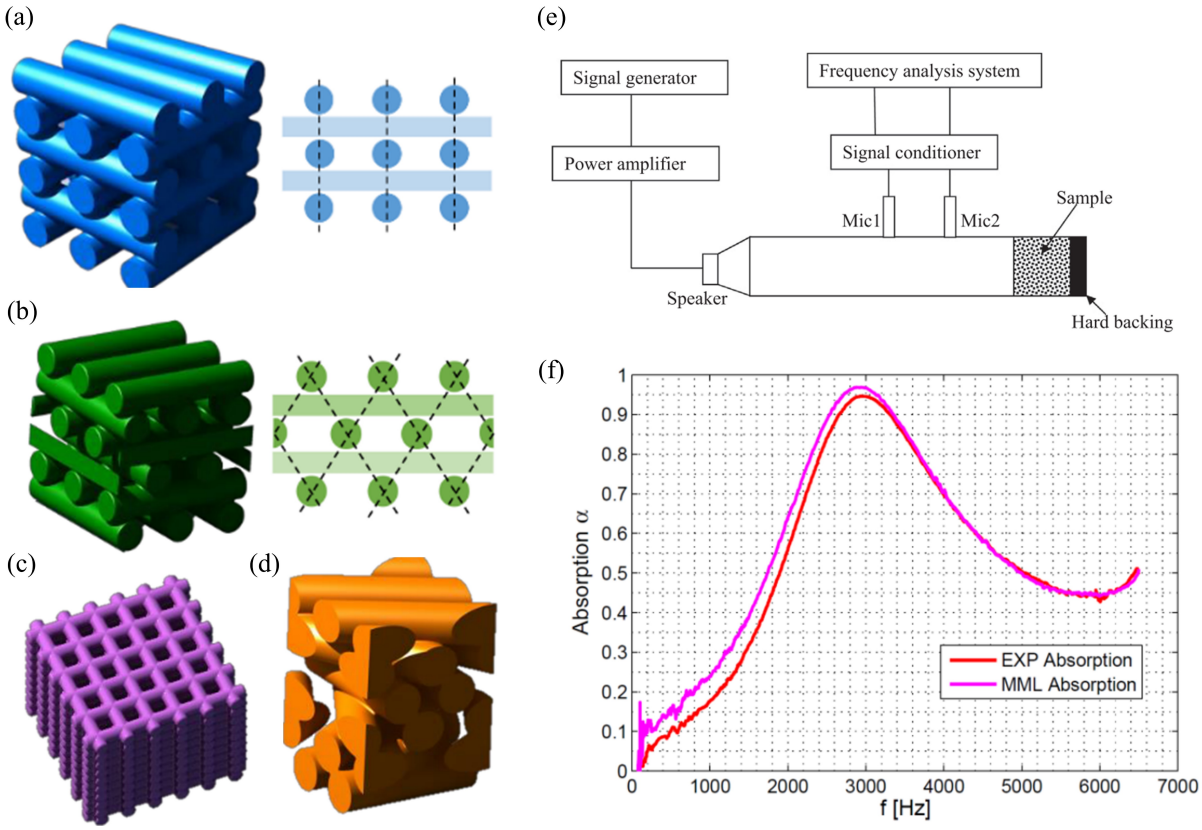

Figure 2.6 Sound absorbing networks in the configuration of a (a) Pure log-pile with aligned filaments (b) Log-pile with alternating filaments (c) Micro-channel stackup (d) Log-pile with rotating filaments [3]. (e) Schematic of a standard Kundt's (impedance) tube for acoustic characterisation [62]. (f) Comparison of the acoustic behaviour for a pure log-pile network printed with a commercial polymer abradable (EXP and MML designate experimental and simulated absorption coefficients, respectively) [3].

The acoustic properties of printed samples were characterised with a Kundt's tube to determine their respective sound absorption coefficient over the frequency range 200 to 6500 Hz. The working principle of the Kundt's tube in Figure 2.6 (e) is to send a array of sound waves towards a porous sample. Reflected waves are captured by a microphone system and compared against incident waves. Figure 2.6 (f) presents absorption coefficients α obtained for a pure log-pile configuration containing two 12 mm thick sections (pore size of 550 μm). Discrepancies generally observed between predicted and measured sound absorption performance were ascribed to process defects, i.e. structure deformation, filament discontinuities, closed pores, first layer sagging and intermittent nozzle clogging.

AM of abradable materials in [3] demonstrated many advantages over current technology (e.g. thermal spraying and casting), because of the tight and repeatable geometrical control of manufactured structures. AM limits production material losses due to a deposit-on-demand approach which removes the need for post-processing operations such as machining down the coating to the final thickness after spraying, as well as surface reworking and autoclave heat treatments described in Section 2.2.4.

2.4 Rheology of filled thermosets

Figure 2.7 (a) shows that fluids are mainly classified into three categories according to the effect of a deforming stimulus on their viscosity, e.g. a shear stress τ in the case of DIW. Newtonian fluids exhibit a constant viscosity, regardless of the applied deformation, as it is the case for ambient air, water and many unfilled thermosets. Shear-thinning fluids are characterised by a decrease of viscosity with increasing shear rate $\dot{\gamma}$, relative to their rest properties; conversely, shear-thickening materials oppose deformation more strongly for higher $\dot{\gamma}$. Combinations of those categories are also possible depending on the magnitude of the $\dot{\gamma}$, for example some materials display a shear-thinning behaviour with a Newtonian plateau [84].

The design of concentrated viscoelastic materials that exhibit significant shear-thinning like in Figure 2.7 (a) is essential in DIW [68]. Materials with a high viscosity are preferably shear-thinning to prevent requiring excessively high pressures for printing nozzles with inner tip diameters <1 mm [68,85]. Upon exiting the nozzle, shear-thinning materials must exhibit a high shear elastic modulus G' and yield shear stress τ_{YS} to retain the printed shape [86]. Therefore, material printability and its ability to retain a filamentary shape may be controlled by a careful adjustment of ink composition and rheology [87]. Specific shear-thinning viscosity models discussed in Section 2.4.1 are useful in describing the flow behaviour of materials for extrusion-based DIW.

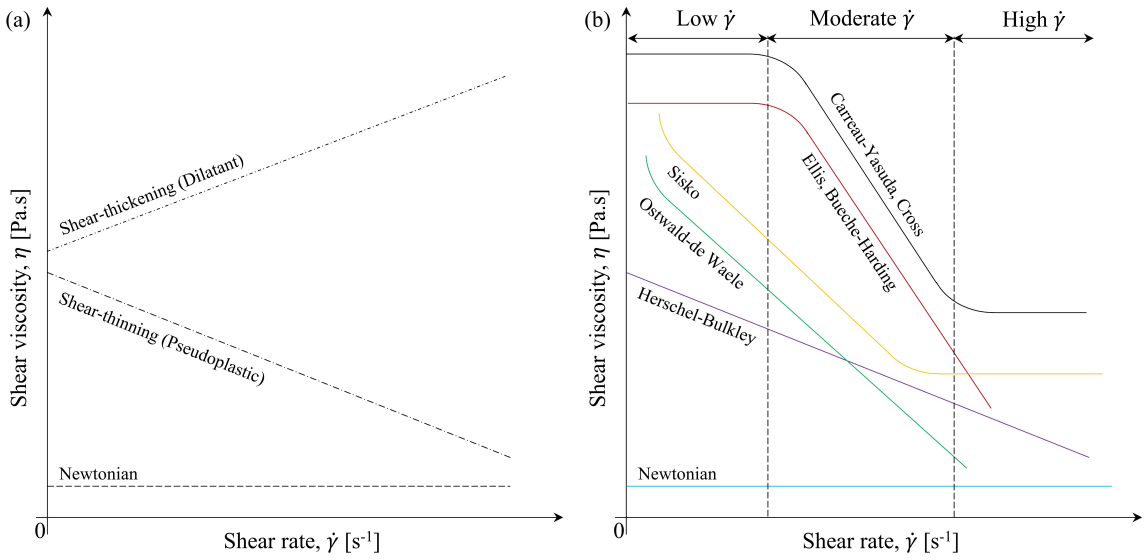

Figure 2.7 (a) Fluids classification according to the viscosity change with increasing deformation rates, adapted from [84]. (b) Summary of the main viscosity models for polymer-based composite materials, adapted from [88–91].

2.4.1 Viscosity models

Figure 2.7 (b) shows many well-known shear-thinning models used in polymer processing relating viscosity to shear rate in three operating regimes (low, moderate and high). The simplest representation of a viscoelastic shear-thinning material is the power-law model (sometimes called the Ostwald-de-Waele model) [88]:

$$\eta(\dot{\gamma}) = K\dot{\gamma}^{n-1}, \tag{2.1}$$

where parameter K is the consistency index and $0 < n < 1$, the dimensionless flow behaviour index, usually obtained by empirical regression fits. In cases where $n = 1$, the material is considered Newtonian; when $n > 1$, the material is shear-thickening. The main limitation of the power-law model is that it cannot predict a zero shear (rest) and infinite shear viscosity, or Newtonian plateaus at low/high shear rates as illustrated in Figure 2.7 (b). It is also not possible to compare the values of K between different materials, as the unit of this parameter (Pa.s^n) depends on the value of n itself. Another limitation of eq. (2.1) is that time effects such as relaxation and gelation are not accounted for. The power-law model has shown satisfactory agreement in predicting the viscosity drop at higher shear rates for a variety of polymer processing applications [84]. Specifically for DIW, eq. (2.1) has been used to model the behaviour of silica or nanoclay-laden epoxy composites [72, 76], as well as epoxy with fumed silica and short carbon fibres [73].

To overcome the problem of rest viscosity, the Herschel-Bulkley model introduces a rest yield stress parameter τ_0 [88, 92]. If the shear stress is below τ_0, the rest viscosity is η_0, such that the viscosity model take the conditional form

$$\eta(\dot{\gamma}) = \begin{cases} \frac{\tau_0}{\dot{\gamma}} + K\dot{\gamma}^{n-1}, & \text{if } \tau > \tau_0 \\ \eta_0, & \text{if } \tau < \tau_0. \end{cases} \tag{2.2}$$

Eq. (2.2) has proven accurate in some studies using DIW to print bioinks [93], boehmite (Al_2O_3) suspensions [86], and colloidal gels [94]. Although the Herschel-Bulkley model is not widely used in polymer processing, materials with a τ_0 are most suitable for DIW processes as printed features are more stable compared to materials without a rest yield stress [95].

Additional parameters are necessary to describe materials exhibiting viscosity plateaus at very high and/or very low $\dot{\gamma}$ [88, 89]. The widely accepted Carreau-Yasuda model introduces limiting boundary viscosities η_0 and η_∞ in low and high shear regimes, respectively:

$$\frac{\eta(\dot{\gamma}) - \eta_\infty}{\eta_0 - \eta_\infty} = \{1 + (\lambda\dot{\gamma})^\Gamma\}^{\frac{n-1}{\Gamma}}, \tag{2.3}$$

where λ is the material relaxation time and Γ represents how rapidly the material transitions between a shear-thinning behaviour and the shear rate-independent plateaus. The flexibility of the eq. (2.3) requires a simultaneous empirical estimation of five material parameters. It was successfully implemented, for example to capture the DIW fluid behaviour of epoxy systems containing fumed silica [73], polylactide acid dissolved in dichloromethane [96] and chitosan inks for solvent casting [97].

Many other viscosity models for thermosets are available, such as the Ellis model accounting for near monotonic viscosity at low shear rates followed by a shear-thinning behaviour [98], the Sisko model accounting for near monotonic viscosity at high shear rates [99] or the Buesche-Harding [98,100] and Cross models [88,89]. These viscosity models, which are less often used for polymer-based composites, are also presented in Figure 2.7 (b).

2.4.2 Extrusion process analysis

A rheometer in a parallel plates configuration is usually employed to obtain rotational data relating material viscosity $\eta(\dot{\gamma})$, here as a function of shear rate. However, studying filled thermosets is challenging, because materials often fracture, i.e. separate from the plates past a certain shear rate resulting in data instability [98, 101, 102]. One avenue to complete the data set of η against $\dot{\gamma}$ at higher stresses is to use process-related capillary rheology [103]. Capillary rheology requires the measurement of mass flow rates through a capillary DIW nozzle. Mass flow rates are taken at different pressure points corresponding to different wall

shear stresses τ_w, expressed as

$$\tau_w = \frac{\Delta P}{4(L/D_o)}, \tag{2.4}$$

where $\Delta P = P_e - P_{atm}$ is the pressure gradient (difference between the applied extrusion pressure P_e and the barometric pressure P_{atm}), L is the length of the capillary section, and D_o is the inner nozzle tip diameter [103]. Mass flow rates are then converted to volumetric flow rates Q with the density of the ink ρ known. Assuming the Hagen-Poiseuille law is applicable [84], i.e. that the flow is unidirectional and symmetrical in the nozzle and that the material is incompressible, the Newtonian shear rate at the nozzle wall $\dot{\gamma}_N$ is estimated with

$$\dot{\gamma}_N = \frac{32Q}{\pi D_o^3}. \tag{2.5}$$

For Newtonian Hagen-Poiseuille flows, the velocity profile in a tube develops into a parabolic geometry [103]. In the case of non-Newtonian fluids, the Weissenberg–Rabinowitsch correction must be applied to $\dot{\gamma}_N$ of eq. (2.5) in order to account for a non-parabolic flow velocity profile [84], that is, in a general form

$$\dot{\gamma}_w = \dot{\gamma}_N \frac{3}{4}\left[1 + \frac{\partial \ln(\dot{\gamma}_N)}{\partial \ln(\tau_w)}\right]. \tag{2.6}$$

Considering a power-law fluid flow, for example, the correction factor reduces the wall shear rate in eq. (2.6) to a strict dependency on the flow behaviour index [103] of the form

$$\dot{\gamma}_w = \dot{\gamma}_N \left[\frac{1+3n}{4n}\right]. \tag{2.7}$$

The apparent (process-related) viscosity, η_a, is finally calculated by combining eq. (2.4) and (2.6), such that

$$\eta_a = \frac{\tau_w}{\dot{\gamma}_w}. \tag{2.8}$$

In addition to the Weissenberg–Rabinowitsch, die swelling effects may be considered through the Bagley correction factor [84]. Some authors have suggested that pressure losses due to end effects account for less than 5% of the total applied pressure for L/D_o values greater than 20 [103, 104]; others found that pressure losses are negligible for L/D_o above 50 [105]. The Bagley correction factor must therefore be applied below a certain nozzle aspect ratio, but end effect are usually considered negligible in the modelling. Wall slip is another phenomenon which may have to be accounted for at very high processing shear rates or in lubricating flows, through the Mooney correction. As slipping reduces the deformation

experienced by the fluid, the phenomenon is quantified by measuring the flow rate of a given material for a range of extrusion pressures and needles lengths or needle diameters. Computing the wall slip correction factor requires estimating the difference between slip and average flow velocities [84].

2.4.3 Effects of nozzle geometry

The flow rate Q presented in eq. (2.5) is a expression encompassing all nozzle geometries, including cylindrical, tapered and rectangular capillary channels encountered in the literature (see Table 2.2). However, when using capillary rheology (for $\dot{\gamma}$ beyond which the materials lose adherence in the rheometer), the calculation of Q depends on the nozzle geometry, and become relatively complex for non-power-law materials (see Appendix A for further details). In the process of determining the parameters of the power-law viscosity model, flow rate measurements cannot be directly adjoined to rotational rheometry data. Empirical couples for Q and ΔP must first be fitted locally, i.e. in the range of shear rates in which the flow measurements were taken. A local fit will yield apparent power-law parameters n_a and K_a, which can then be inserted into eq. (2.4) and (2.7) to estimate apparent viscosity and shear rate couples. Only then can a general fit be performed for the full range of $\dot{\gamma}$ including rotational rheometer data. The volumetric flow rate Q_c for extrusion through a cylindrical nozzle [84, 106] is related to ΔP as

$$Q_c = \pi D_o^{\frac{3n_a+1}{n_a}} \left[\frac{\Delta P}{K_a L}\right]^{\frac{1}{n_a}} \left[\frac{n_a}{3n_a+1}\right] 2^{\frac{-(3n_a+2)}{n_a}}. \tag{2.9}$$

When a tapered nozzle is used, e.g. to enhance flow rate for highly viscous materials, additional geometrical parameters are required [107], such that

$$Q_T = \frac{\pi D_o^3 D_e^3}{32} \left[\frac{3n_a \Delta P \tan(\theta)}{2K_a \left(D_e^{3n_a} - D_o^{3n_a}\right)}\right]^{\frac{1}{n_a}}, \tag{2.10}$$

where D_e is the nozzle inlet diameter and θ is the half-cone angle. The Rabinowitsch correction must be also modified to account for a different geometry than the underlying assumption in eq. (2.6) and (2.7) accordingly giving the corrected apparent shear rate for tapered nozzle

$$\dot{\gamma}_a = \left[\frac{3n_a+1}{n_a}\right] \frac{8Q_T}{\pi D_o^3}. \tag{2.11}$$

In summary, by selecting the appropriate model from Section 2.4.1, and combining apparent viscosities found with eq. (2.8) to rheometer data, the viscosity of printing materials for a broad range of shear rates can be established. Such models can help in controlling

the printing process as a whole to determine the required pressures at a desired printing speed, for example, provided that the appropriate correction factors have been applied to the nozzle geometry. It must be noted that the aforementioned models and developments do not take into account the effects of cross-linking (cure), which is an important consideration for printing filled thermosets.

2.4.4 Chemorheology

Throughout Section 2.4, materials have been considered as non-reactive, i.e. that their viscoelastic behaviour remains constant over time. In practise, thermosets undergo a chemical reaction which leads to the formation of an infinite cross-linked network. The curing reaction (or simply *cure*) is initiated once the base resin and hardening agent are combined [108]. Therefore, viscosity is not only a function of shear rate, but also of time, and is the focus chemorheology, defined as the study of the viscoelastic behaviour of reacting systems [98].

Existing chemorheological models have been developed for thermoset injection moulding, resin transfer moulding and pultrusion [109]. There are two main model categories: time-dependent models and phenomenological cure-dependent kinetic models. The latter require relatively more complex characterisation involving several differential scanning calorimetry (DSC) tests repeated for a range of cure temperatures [110]. However, performing DSC sweeps gives insightful information about the reaction kinetics and material chemical properties, such as the glass transition temperature T_g and degree of cure ξ (i.e., the ratio of the instantaneous heat released by the reaction ΔH to the total heat of reaction ΔH_0 [111]).

In thermoset processing, it is frequently assumed that cure is an autocatalytic reaction, that is, the heat generated during cross-linking accelerates the formation of the infinite network [112]. The commonly used autocatalytic model is expressed as

$$\frac{d\xi}{dt} = (k_1 + k_2\xi^{m_1})(1-\xi)^{m_2} \quad \text{with} \begin{cases} \xi = \frac{1}{\Delta H_0}\int_0^t \frac{dH}{dt}dt \\ k_i = A_i \exp\frac{-E_i}{R_g T}, \quad i = 1,2 \end{cases} \tag{2.12}$$

where k_i are reaction constants, m_i are reaction orders, A_i are pre-exponential factors, E_i are activation energies, R_g is the universal gas constant and T is the reaction temperature. The heat flow H and ensuing ξ are obtained with isothermal DSC (time) sweeps at different temperatures, and ΔH_0 is measured through a dynamic (temperature) sweep. Having determined all the associated parameters, the differential kinetic equation (eq. (2.12)) is solved numerically for time. The resulting $\xi(t)$ function is manipulated to obtain a multiplication factor describing the increase of η relative to the η_0 of the thermoset, for example with the Castro-Macosko model [110].

The kinetic model in eq. (2.12) showed good agreement with experimental data for unfilled epoxy, vinyl-ester and polyester resins [112], phosphorylated epoxies [102], short carbon fibre-reinforced epoxy systems [109], epoxy with hollow glass microspheres [113] as well as epoxy-MWCNT suspensions [114]. All the reported studies using the autocatalytic model involved high processing temperatures (70-210 °C).

An approach requiring only time sweeps from oscillatory rheology is also proposed in the literature for neat and filled epoxy systems [98, 115]. The advantage characterising the effect of cure on viscosity with a rheometer rather than DSC is that a direct relationship between η and t may be established with a single empirical data fit at a fixed reaction temperature. For example, the first-order isothermal cure model may be used with time as an explicit variable:

$$\eta^*(t) = \eta^*(t_0) a \exp bt \tag{2.13}$$

where $\eta^*(t)$ is the complex (oscillatory) time-dependent viscosity, and a and b are empirical viscosity change parameters. Because $\eta^*(t)$ is not necessarily equal to $\eta(\dot{\gamma})$ [84], it is appropriate to rather express eq. (2.13) in the form of a relative viscosity $\eta^*(t)/\eta^*(t_0)$ [98,116]. The normalised viscosity can be interpreted as a coefficient reflecting the magnitude of change in viscosity through time from η^* at t_0 ($\eta^*(t_0)$, corresponding to the onset of cure at the time of mixing) to $\eta^*(t)$ at time t. The coefficient can then be applied as stated previously to apportion the viscosity change attributed to shear rate [98, 117]. For example, to predict the viscosity during the DIW process of an arbitrary power-law thermoset composite, a suitable model could be

$$\eta(\dot{\gamma}, t)|_T = K\dot{\gamma}^{n-1} \cdot \frac{a}{\eta^*(t_0)} \exp bt. \tag{2.14}$$

In eq. (2.14), the effects time (cure) and shear rate (extrusion) are superimposed to obtain a general rheological composite model. If required, temperature may also be considered as a variable through the pre-exponential factor a using an Arrhenius type equation similar to the k_i in eq. (2.12) [98].

CHAPTER 3 METHODOLOY AND SCOPE

3.1 General approach

One of the main objectives of the FACMO Chair is to print sound absorbing abradable coatings onto non-planar composite substrates, representative of an aircraft engine fan case. The projected large-scale printing infrastructure consists of a multinozzle printhead mounted on a robotic arm, which will allow material extrusion through an array of 250 µm cylindrical nozzles. This work addresses the fundamental need for a printable composite material which will be used in future works to demonstrate the large-scale feasibility of printing multifunctional porous coatings.

3.1.1 Objective 1: Develop a thermosetting abradable material compatible with a direct ink writing printing process

A commercial aerospace-grade product (EC3524 B/A Black, 3M™, France), hereafter the "benchmark", was modified to develop a printable abradable material. The benchmark is currently used as a hand-applied sacrificial coating on engine fan cases by the industrial partner. Here, the benchmark was extruded through a single 250 µm tapered nozzle and deposited into a pure log-pile network (see Figure 2.6 (a)), hereafter "micro-scaffold", using linear deposition platforms (two planar ALS25030 stages and one vertical ALS130-100 stage, Aerotech, USA). A tapered nozzle was selected to enhance material flowability, since the beanchmark could not be extruded using 250 µm cylindrical nozzles. The printed shape was lost prior to gelation, demonstrating that directly automating the production using the benchmark was not possible. Hence, the primary step here was to study the residual weight contents in the benchmark and the base epoxy system to establish the GM content, which was the starting point for formulation development. Materials with higher GM loadings than the benchmark were initially thought to provide the required consistency for the composite to hold a printed shape. However, increasing the loading was unsuccessful in achieving any shape retention, because of GM crushing during extrusion and subsequent shape loss.

The approach was instead reoriented towards decreasing the GM content and incorporating a secondary filler. GM loadings were selected using a design of experiments approach for mixture development with equidistant filler contents (0, 5, 10, 15 & 20 wt.% GM). Fumed silica (FS) was gradually blended in the mixtures to enable printed shape retention. The addition of FS was mainly limited by the available pneumatic system; beyond a certain combination of GM and FS, no material could be extruded at the maximum system pressure. Mixtures with different filler loadings were printed with both 250 µm cylindrical and tapered

nozzles, and their ability to retain a shape was assessed based on a qualitative scale rating.

All the tested formulations were arranged in a printability map specifying their process behaviour. Five blends - one per GM loading point - which exhibited the best stacking height and shape retention through time were retained for further characterisation. Extruded filaments were inspected with the aid of scanning electron microscopy (SEM) and micro-computed tomography (μCT), to assess the occurrence of GM crushing in the five blends. Only three blends, hereafter "star blends", were considered for further test campaigns.

Rheological models were computed for the three star blends based on oscillatory strain sweeps and separate time sweeps, as well as rotational and flow-rate capillary rheometry. Based on the developments summarised previously in Table 2.2, there are virtually no studies which take into account the effects of cure on material behaviour in thermoset DIW. However, in this project, quantifying the combined effects of time and shear rate is important for large area printing (i.e., for printing an abradable micro-structure on an engine fan case) because of the extended processing time. Internal studies estimated that up to 3 hours are needed to print the desired micro-structure on the full circumference of the LEAP-1A fan case for a deposition speed of 200 $mm.s^{-1}$ (see the abradable coating indicated with a yellow strip in Figure 2.2 (a)). Over the course of coating production, the material cures in the syringe, thus its viscosity is expected to increase significantly between mixing and the completion the extrusion process.

Another avenue was investigated in parallel of adjusting the GM content and adding FS. The benchmark itself was modified with the addition of petroleum jelly (PJ, Vaseline™ in this case). The rationale behind this approach was to identify the printability of all those mixtures using 250 μm tapered and cylindrical nozzles including SEM observations, so as to complete the works initiated in [3].

3.1.2 Objective 2: Evaluate the bulk mechanical properties of the new material and assess the predictability of acoustic properties for printed structures

The potential of the star blends for acoustic applications was demonstrated through Kundt's tube characterisation by printing samples with a 300 μm target pore size. Acoustic absorption coefficients and damping ratios were obtained for printed samples and compared against simulated values to verify that predictable sound absorption properties could be obtained when printing the star blends.

A characterisation of mechanical properties through micro-hardness (Shore D) and pullout strength measurements were also carried out to help selecting the ideal material between the three star blends.

As for the study of different PJ loadings in the benchmark, the effect of the grease-like non-reactive phase was also assessed. The mechanical performance of PJ-benchmark mixtures were compared to that of the star blends to give a complete overview of the possible solutions for a multifunctional abradable material.

3.2 Relation to the submitted paper

Chapter 4 presents the paper which brings together the most important results and findings of this project, i.e. the development of new thermosetting abradable composites for DIW. The paper thus encompasses the first objective of the thesis (see **O1** in Section 1.2). It was submitted to the peer-reviewed journal *Additive Manufacturing* on May 6 2021. Following review, the revised version in Chapter 4 was submitted on 6 July 2021, and made available online on 11 August 2021 at `https://doi.org/10.1016/j.addma.2021.102245`. Because the scope of the journal includes the development of multifunctional materials as well as the formulation and characterisation of new composite materials, *Additive Manufacturing* was identified as a suitable journal for publishing the results herein. In essence, the highlights of the submitted paper can be summarised as:

1. 3D printable epoxy systems contain hollow glass microspheres and/or fumed silica.
2. High fumed silica contents improve material elasticity and enable shape retention.
3. A modified empirical model predicts the flow behaviour of developed materials.
4. Printing speeds up to 175 $mm.s^{-1}$ pave the way for large area industrial production, while retaining high-resolution features.
5. Efficient sound absorbing micro-scaffolds are printed using the developed composites.

CHAPTER 4 ARTICLE 1: DESIGN OF THERMOSET COMPOSITES FOR HIGH-SPEED ADDITIVE MANUFACTURING OF LIGHTWEIGHT SOUND ABSORBING MICRO-SCAFFOLDS

David Brzeski[a,b], Iee Lee Hia[a], Jean-François Chauvette[a], Rouhollah D. Farahani[a], Nicola Piccirelli[c], Annie Ross[b], and Daniel Therriault[a,*]

[a]Laboratory for Multiscale Mechanics (LM^2), Mechanical Engineering Department, Polytechnique Montréal, Montréal, Québec H3T 1J4, Canada
[b]Laboratoire d'Analyse Vibratoire et Acoustique (LAVA), Mechanical Engineering Department, Polytechnique Montréal, Montréal, Québec H3T 1J4, Canada
[c]Safran Composites, a technology platform for Safran Tech, Itteville, 91760, France

Submitted 6 May 2021; Revised 6 July 2021; Accepted 11 August 2021.
Available online at `https://doi.org/10.1016/j.addma.2021.102245`

Abstract

Low printing speeds in extrusion-based additive manufacturing of thermosets, such as direct ink writing, are an obstacle for industrial-scale production. This work aims at developing lightweight thermoset composite materials compatible with the high-speed direct ink writing of porous microstructures featuring a sound absorbing functionality. The developed materials are blends of an aerospace-grade epoxy matrix filled with different loadings of hollow glass microspheres and fumed silica nanoparticles. The printability of the blends was assessed through microscopy and tomography scans, by studying the shape retention for different filler loadings and nozzle configurations. Oscillatory, rotational, and capillary rheological studies were conducted to obtain viscosity models relating extrusion pressures and printing speeds. Three promising blends containing a combination of 0-10 wt.% hollow glass microspheres and 0-12 wt.% fumed silica were selected based on their printability and shape retention. Printing speeds ranging from 110 to 175 mm.s^{-1} were attained using 250 μm tapered nozzles, which is over three time the highest speeds reported in the literature. An acoustic absorption characterisation using a Kundt's tube was carried out for printed porous microstructures resembling a log-pile network with 300 μm square pores. Average acoustic absorption coefficients above 0.6 were achieved for frequencies from 500 to 6000 Hz.

4.1 Introduction

Noise produced by commercial aviation, mostly originating from aircraft engines, has become an industry-wide concern over the past years, owing to strict noise pollution level targets set by regulatory bodies for the next decade [118]. Many solutions have been proposed to reduce the noise emitted by aircraft engines for mitigating the detrimental health effects of noise around airports [11]. For example, porous structures have demonstrated good sound absorbing capabilities in the frequency range of typical aircraft engine acoustic emissions [62, 119–122]. One such type of porous media are micro-scaffold structures, wherein straight cylindrical rods are placed parallel to each other across a given layer of material. The orientation of every other layer is perpendicular to the previous layer, thus forming a log-pile network that interferes with the propagation of sound waves. Friction between the air in the pores and the micro-scaffold causes thermal and viscous losses, which leads to acoustic energy dissipation, and thus sound absorption [120, 121].

Other types of designs, e.g. micro perforated plates [123, 124], sonic crystals [125] and Helmholtz resonators [126] have also demonstrated good noise reduction properties, albeit for frequencies below the range targeted in this work. Intricate sound absorbing geometries such as micro-scaffolds requiring high printing resolution can be produced by additive manufacturing (AM) [127]. Direct ink writing (DIW) is an extrusion-based AM process whereby material is forced through a micro-nozzle under pressure. Upon exiting the nozzle, the material is deposited according to the desired shape with the aid of positioning stages. DIW is a suitable method to shape paste-like viscoelastic materials [61, 128], and thus can be used to manufacture lightweight micro-scaffolds bearing a sound absorption function [3].

In aerospace applications, one avenue to obtain lightweight materials is to use thermosets filled with hollow glass microspheres (GM) to lower the density of the neat resin [114, 128–131]. Besides, fumed silica (FS) has been shown to act as a rheological thickener, thus providing the desired rheological properties for materials to exhibit higher shape fidelity after printing [72, 113, 132–134]. The addition of GM and, separately, FS was demonstrated to induce a viscoelastic shear thinning behaviour to the host resin [72, 76]. Shear thinning materials exhibit high viscosity at rest after extrusion, to enable filament shape retention, yet display a lower viscosity at high shear rates, to facilitate extrusion during the DIW process [74, 85, 128, 135, 136].

Low printing speeds impede industrial-scale applications of thermoset DIW, as manufacturing large porous structures is time-consuming and may exceed the material gelation phase. The necessity of this research is critical, as in the published studies of composite DIW, printing speeds are limited between 5 to 40 $mm.s^{-1}$ partly due to high material viscosities and low extrusion pressures [60, 74–76, 137]. For example, epoxy systems containing

8 wt.% fumed silica were printed at 10 mm.s^{-1} using UV-assisted DIW with 0.7 and 1.0 mm nozzles [74]. Epoxy systems containing up to 12.5 wt.% nanoclay were limited to 30 mm.s^{-1} when using DIW with 0.6 mm nozzles [76]. Vibration-assisted screw-extrusion DIW of epoxy composites with up to 46 vol.% milled-carbon fibre and nanoclay were also reportedly printed at 40 mm.s^{-1} using a 0.6 mm nozzle [60]. A similar technology was employed to print an epoxy system filled with 56 vol.% GM and 15 vol.% of short carbon fibres at a deposition speed of 40 mm.s^{-1} using a 0.58 mm nozzle [79]. A co-extrusion process was able to print structures containing 58 vol.% GM with a 1.2 mm nozzle, at an estimated speed of 10 mm.s^{-1} [81]. A DIW process with acoustic focusing enabled the printing of epoxy inks containing 5-10 wt.% FS, 4-19 wt.% GM (2-9 vol.% GM) and 8-24 wt.% acetone in [72]; yet speeds were limited to 20 mm.s^{-1} using a rectangular nozzle of 210 μm hydraulic diameter.

The objective of this paper is to identify suitable loadings of GM and FS dispersed in a commercial aerospace-grade epoxy matrix, for the high-speed additive manufacturing of fine acoustic micro-scaffolds. The material design process begins with an initial printability assessment by which the studied blends are evaluated based on (1) the quality of printed lines and (2) their ability to hold the desired printed shape over the duration of the composite's cross-linking. Tested blends are then categorised on a printability map highlighting different print quality zones as a function of filler loadings. A time-dependent viscosity model is computed from rheological studies to help select optimal printing parameters for the most promising materials. Sound absorption capabilities of the developed materials are also demonstrated experimentally using a micro-scaffold geometry.

4.2 Experimental methods

4.2.1 Materials

Two types of material systems manufactured by 3M™ were studied. First, a commercial thermoset "benchmark" (Scotch-Weld™ EC-3524 B/A Black) was used as a baseline material for control tests. The benchmark has a cured density ρ of 500 kg.m^{-3}, a pot life of 90 min and a cure period of 48 h at room temperature [41]. The benchmark consists of two components: an amine-based curing agent (part A) and a base epoxide compound (part B), both prefilled with GM (Glass Bubbles Floated Series, A20/1000, 3M™, France) [138]. Second, a two-part neat resin system (part A & B) similar to the benchmark but without fillers was used as the matrix for composite development (ρ = 1170 kg.m^{-3} and 3h pot life). The same GM used in the benchmark were supplied separately by 3M™ (ρ = 200 kg.m^{-3} and a diameter of $25 - 90$ μm) for filling the neat resin. Hydrophilic FS (Aerosil 200, Evonik, USA) was utilised as a rheological thickener in this study (tapped density of 0.5 kg.L^{-1}, diameter of $12 - 14$ nm) [139].

4.2.2 Sample preparation

Material mixing

Parts A and B were hand mixed separately with the desired loadings of GM and/or FS to prevent GM crushing. Filled part A and part B were then mixed with a weight ratio of 94:100, per manufacturer guidelines. The paste-like material obtained was loaded immediately into 3 cm^3 syringes (Nordson EFD Co.) for printing.

Sample printing

Two types of nozzle were utilised: cylindrical (#7018333, Nordson, USA) and tapered (#7018391, Nordson, USA). Nozzle geometries were measured with an optical microscope (SZX12, Olympus, USA). Cylindrical nozzles have a 250 µm inner tip diameter D_i and 6.35 mm length L, whereas tapered tips have a $D_i = 250$ µm, 2.7 mm entry diameter D_e and 5.7° half cone angle θ. A 250 µm tip diameter was selected to reduce nozzle clogging caused by the GM, while allowing for a satisfactory sound absorption performance (i.e., filament diameters of $100 - 400$µm were recommended in previous works [3, 62, 120]).

As shown in Figure 4.1 (a) were printed with a linear stage system (Aerotech, USA) made of two planar ALS25030 stages and one vertical ALS130-100 stage, controlled via the Automation 3200 software (version 2.13). The Aerobasics G-code supplied to the Aerotech system was generated using a custom slicing algorithm (Matlab R2008a) specifying the displacement commands of the positioning stages. The material dispensing system installed on the vertical axis of the Aerotech system was controlled by a pressure regulator (HP-7X, EFD).

The printability of designed blends was assessed by varying two main process parameters: the linear speed of the build platforms ($1 - 300$ mm.s^{-1}) and the extrusion pressure ($0.15 - 4.55$ MPa). The clearance between the nozzle tip and the substrate, i.e. the first layer height, was set at 0.26 mm; subsequent layer height was 0.20 mm. At a given pressure, linear displacement speeds were adjusted according to the achievable flow rate to deposit straight, smooth and continuous 250 µm diameter filaments on glass substrates. Filament width measurements were made using an optical microscope and post-processed with ImageJ. The rheological model was validated by studying highest printing speed achievable with the system, i.e. by adjusting the printing speed to obtain filaments of 250 µm diameter at the maximum dispensing pressure of 4.55 MPa available on the HP-7X system.

For acoustic tests, micro-scaffolds were printed into cylindrical shells (1.2 mm thickness) with a 30 mm outer diameter (to fit inside the Kundt's tube, see Section 4.2.7) and a 5 mm thickness. As indicated in Figure 4.1 (c) square pore size of 300 µm, equivalent to a nominal volume infill of 45%, was selected for the demonstration of sound absorption capabilities.

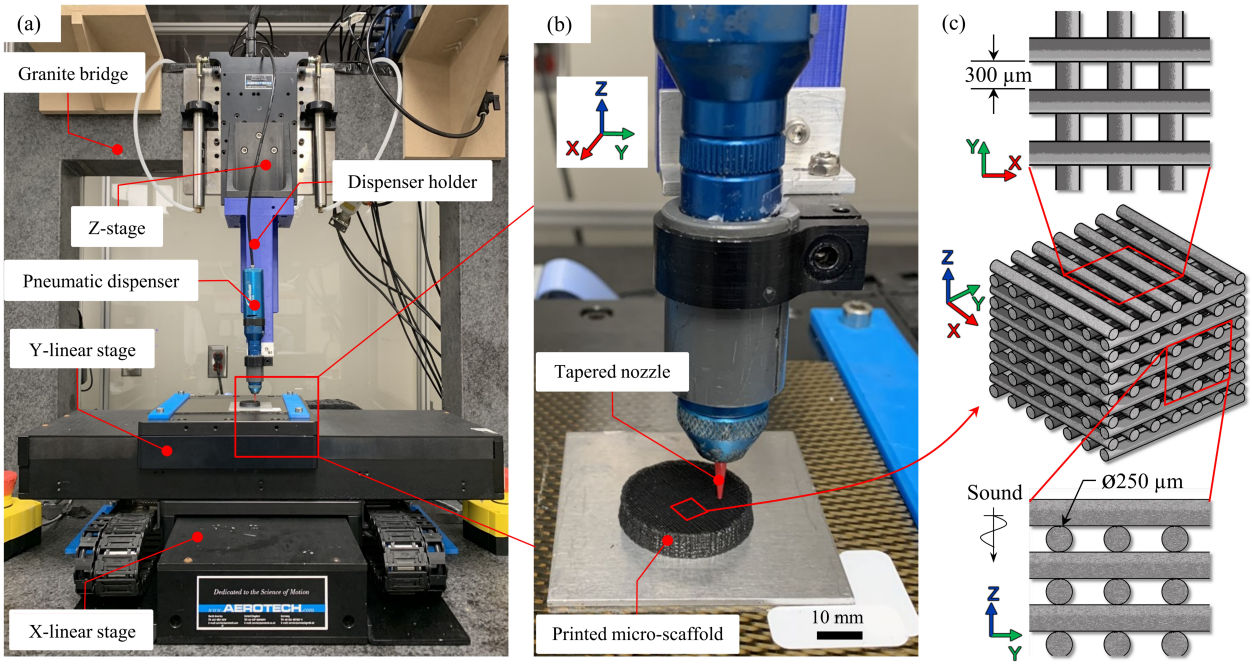

Figure 4.1 (a) Linear deposition system with an air-operated pressure dispenser mounted with a holder on the Z-stage. The vertical stage is mounted on an overhead granite bridge. Robotic X & Y-stages on the granite platform move on the horizontal plane during the printing of each layer. The displacement of all three stages is controlled through an Aerobasics G-code specifying displacement commands. (b) Enlarged view shows a 250 µm tapered nozzle shaping the 0GM:12FS blend into a 5 mm thick acoustic micro-scaffold at 50 mm.s^{-1} and 2.8 MPa. (c) Cut-out schematic of the acoustic samples, including the designed pore size and filament diameter with sound propagation along the Z-axis.

For this sample design, the volume of material contained in a syringe (3 cm^3) limited sample thickness to 5 mm. Consequently, the desired total sample height was divided into 5 mm thick sections, as in Figure 4.1 (b). Once cured, 5 sections for a given blends were stacked vertically to form a 25 mm tall cylinder for the Kundt's tube.

4.2.3 Selecting filler loadings

Thermogravimetric analysis (TGA)

A TGA (Q500, TA Instruments, USA) was carried out to investigate the GM content in the benchmark as well as the residual content of additives in the neat resin. The compositional analyses were performed in accordance with ASTM E2550-17, whereby approximately 10 mg of cured samples were heated from room temperature to 800 °C at a rate of 20 °C.min^{-1} under nitrogen atmosphere. The test for neat resin was stopped at 600 °C where no more visible weight variation was observed (see Figure B.1 for details).

Studied filler loadings

The most crucial aspects for screening printable blends were the ability to flow through a 250 μm nozzle and the ability to retain a given shape post-printing. With these criteria as guidance, GM loadings within neat resin were first selected as 0, 5, 10, 15 and 20 wt.%. The maximum GM loading (20 wt.%) was based on the GM content in the benchmark measured by TGA (∼22.5 wt.%); higher GM loadings resulted in frequent nozzle clogging or post-deposition shape loss when printing was possible. Different FS loadings were then added until a 3D micro-scaffold could be printed. At a set GM content, materials with too low FS loadings could not hold a filamentary shape upon extrusion, while too high FS loadings could not be extruded by the dispensing system (HP-7X). Hence, FS content was maximised to improve filament shape retention, whilst remaining extrudable through both tapered and cylindrical 250 μm nozzles. The blends reported in Table 4.1 displayed the best post-printing shape retention and so were further investigated in this work. Designed blends are named according to their fillers loading; for example, 5GM:10FS refers to a blend with 5 wt.% GM and 10 wt.% FS, completed with neat resin. Volume contents in Table 4.1 were calculated using the Rule of mixtures.

Table 4.1 GM and FS loadings with measured cured density of the studied blends.

Studied blend	**GM weight content, [wt.%]**	**GM volume content, [vol.%]**	**FS weight content, [wt.%]**	**FS volume content, [vol.%]**	**Cured density, ρ [kg.m^{-3}]**
0GM:12FS	0	0	12	5.0	1272
5GM:10FS	5	28.2	10	4.1	973
10GM:8FS	10	45.4	8	3.2	837
15GM:7FS	15	56.9	7	2.8	758
20GM:6FS	20	65.2	6	2.4	642
Benchmark	22.5	68.5	0	0	505

Bulk density measurements

The bulk density of each blend was obtained using an AccuPyc II 1340 helium gas displacement pycnometer (Micrometrics, USA). For a given blend, about 1 g of cured bulk material was weighed, inserted into a 3.5 cm^3 chamber, and placed inside the apparatus. The densities presented herein were averaged from 100 data points.

4.2.4 Microstructure observations

Scanning electron microscopy (SEM)

The shape retention and filament microstructure of candidate blends were investigated using SEM observations (TM3030, Hitachi, USA) on extruded filaments and micro-scaffolds. Samples were coated with a 10 nm layer of chrome before the imaging analysis. All the imaging analyses were performed at a 5 kV voltage supply. Filler dispersion and integrity were analysed based on the cross-sectional views of printed filaments which were fractured manually at room temperature. Scaffolds shape fidelity was studied based on sample top and side cross-sections which were obtained by cutting into the scaffolds with a sharp razor blade.

Micro-computed tomography (μCT)

μCT scans were used to assess the presence of crushed fillers and manufacturing defects within printed filaments and micro-scaffolds by non-destructive means. Volumetric measurements were performed with an Xradia 520 Versa 3D Xray microscope (Zeiss Canada, Canada). Samples were analysed at an acceleration voltage ranging from 50 kV to 80 kV, with a power between 4 W and 7 W, using 0.4× and 4× objectives. Scan parameters and conditions for all images presented in this work may be found in Table B.1. The exposure time was adjusted in the interval 1.8 s and 11 s depending on the size of the scanned sample. Animations (see Vid. 1 & 2 in Appendix B) and μCT images in this work were generated using the Dragonfly Software (Object Research Systems ORS, Canada).

4.2.5 Rheology

Oscillatory and steady shear rheological studies were performed on the benchmark and the studied blends using an MCR502 modular rheometer (Anton Paar, Germany) fitted with a parallel plate geometry (25 mm diameter, 1.0 mm gap) at 25 °C. Oscillatory shear tests were carried out to first determine the linear viscoelastic region of the sample with amplitude sweeps at shear strains γ in the range $\gamma = 0.01 - 100$ mm/mm , and an angular frequency $\omega = 10$ rad.s^{-1}. The amplitude sweeps were also used to identify the yield stress of the developed materials, which is related to the onset of material flow. Oscillatory time sweeps were performed at a shear strain below the linear viscoelastic region limit of each material ($\omega = 10$ rad.s^{-1}) identified from amplitude sweeps. Time sweeps were used to study the relationship between the shear storage modulus G', shear loss modulus G'', complex viscosity η^*, and time t. The pot life of each material for the printing process was estimated at the point when η^* had doubled. Rotational shear-viscosity measurements were performed in

the shear rate range $\dot{\gamma} = 0.001 - 10\ s^{-1}$ to study the behaviour of the blends at low and moderate shear rates in order to model the flow behaviour of the blends. Rotational viscosity measurements were recorded within 7 min. after mixing part A and part B to minimise the effect of time on viscosity due material cross-linking.

4.2.6 Capillary flow analysis

Following the method proposed by Bruneaux et al. [103], each blend was extruded through a 250 µm tapered nozzle between 15 and 100 s employing the HP-7X extrusion system. The extruded material was then weighed on a high precision balance. The mass was divided by the corresponding extrusion time to obtain the mass flow rate at a given pressure, which was then converted to volumetric flow rate with measured blend densities reported in Table 4.1. For each blend, five equally spaced pressure points were selected, and each mass flow rate measurement was taken three times.

4.2.7 Kundt's tube characterisation

Acoustic absorption coefficients for the three best blends were measured with an Kundt's (impedance) tube according to the ASTM E1050-19 standard, using the setup shown in Figure 4.2. A two-microphones technique with hard back-wall was used to measure the absorption coefficients. Sound absorption coefficients were measured in the range of frequencies $f = 500 - 6000$ Hz. All samples were subjected to the absorption test three times, each time being removed and installed back again in the Kundt's tube.

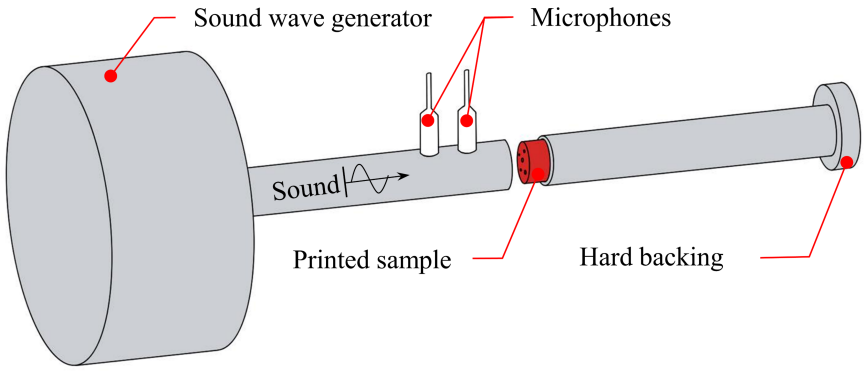

Figure 4.2 Kundt's tube measurement setup, with a hard backing and two microphones, adapted from [62].

4.3 Theory and calculations

4.3.1 Viscosity behaviour of shear-thinning fluids

Time-dependant model

Viscosity is a time dependent property in thermoset systems during the material cross-linking reaction. Viscosity changes during the gelation phase can be captured for example with the first-order isothermal model [98,115], represented as a sum of exponential functions:

$$\eta^*(t) = a_1 e^{b_1 t} + a_2 e^{b_2 t}, \tag{4.1}$$

where η^*(t) represents complex time-dependent viscosity, t is the time elapsed since mixing, and a_1,a_2,b_1,b_2 are empirical constants obtained by oscillatory time sweeps. To link complex viscosity and shear viscosity into a rheological model for DIW, $\eta^*(t)$ is expressed as a non-dimensional relative viscosity, following the approach adopted in [116,117,129]. Dimensionless viscosities over time are derived from eq. (4.1) by dividing η^*(t) by the initial blend viscosity $\eta^*(t_0)$ (at $t = 0$, from oscillatory time sweeps), such that

$$\frac{\eta^*(t)}{\eta^*(t_0)} = \frac{a_1}{\eta^*(t_0)} e^{b_1 t} + \frac{a_2}{\eta^*(t_0)} e^{b_2 t}. \tag{4.2}$$

Normalised values $\eta^*(t)/\eta^*(t_0) \geq 1$ from eq. (4.2) represent the magnitude of viscosity change through time, which can be used as a multiplication factor for the effect of shear rate on the viscosity.

Shear rate-dependant model

A common assumption for filled polymers is that a power-law (Ostwald-de Waele) model can describe their shear-thinning behaviour [85, 102, 106, 107, 116]. The power-law model relates shear viscosity η to shear rate $\dot{\gamma}$ as

$$\eta = K\dot{\gamma}^{n-1}, \tag{4.3}$$

where $0 < n < 1$ is the flow exponent, and K is the consistency index [84]. Parameters n and K in eq. (4.3) are usually obtained from rotational rheology tests by a power-law fit. In this study, material instabilities occurred in the rheometer for $\dot{\gamma} > 10^0$ s^{-1}, making direct rotational shear viscosity measurements difficult. Hence, viscosity was characterised indirectly through flow rate capillary rheometry for $\dot{\gamma} > 10^0$ s^{-1} (see Section 4.3) therefore combines rotational rheology data ($10^{-3} < \dot{\gamma} < 10^0$ s^{-1}) and capillary rheology results ($10^0 < \dot{\gamma} < 10^4$ s^{-1}) to capture the full range of $\dot{\gamma}$ expected for high-speed printing.

The first step to obtain overall parameters n and K is to model the behaviour for $\dot{\gamma} > 10^0$ s^{-1} by determining apparent parameters n_a and K_a. Tapered nozzles are preferred for this operation as they improve material flowability by gradually decreasing the capillary diameter and converging the flow towards the nozzle tip, unlike cylindrical nozzles [140]. High flow rates are necessary to enable the decoupling of the effects of $\dot{\gamma}$ from curing time during flow rate measurements. The volumetric flow rate through a tapered nozzle Q_T for a power-law material is related to the corresponding extrusion pressure gradient ΔP [140, 141] through

$$Q_T = \frac{\pi D_i^3 D_e^3}{32} \left[\frac{3n_a \Delta P \tan(\theta)}{2K_a \left(D_e^{3n_a} - D_i^{3n_a} \right)} \right]^{\frac{1}{n_a}}, \tag{4.4}$$

where D_i is the inner tip diameter of the nozzle, D_e the nozzle entry diameter and θ the nozzle half cone angle. Because eq. (4.4) is dependent on the two modelling parameters n_a and K_a, an array of values for n_a is set, and corresponding parameters K_a are calculated based on empirical couples of Q_T and ΔP. The n_a minimising the standard deviation of approximated K_a among all tested pressures, and the associated K_a are retained. From experimental Q_T data, the apparent shear rates $\dot{\gamma}_a$ are then evaluated with the relation proposed in [107] for non-Newtonian fluids to account for a non-parabolic flow velocity profile (Weissenberg-Rabinowitsch correction):

$$\dot{\gamma}_a = \left[\frac{3n_a + 1}{n_a} \right] \frac{8Q_T}{\pi D_i^3}. \tag{4.5}$$

To model the flow behaviour attributed to the capillary data points, apparent viscosity η_a is also obtained from the approximated n_a, K_a, and $\dot{\gamma}_a$ a evaluated from eq. (4.5). Lastly, a power-law fit is performed for the combined data ($10^{-3} < \dot{\gamma} < 10^4$ s^{-1}) to obtain n and K in eq. (4.3). Note that nozzle end effects such as swelling were neglected in the modelling, because the L/D_o ratio is 25 for cylindrical tips and 98 for tapered tips. Pressure losses due to end effects account for less than 5% of the total applied pressure for L/D_o values greater than 20 [103, 104]. Neglecting end effects for an L/D_o of 25 and 98 therefore seems to be a valid approximation.

Time and shear rate superposition

A time-dependent flow behaviour model can be constructed from the description of dimensionless viscosity change through time (due to curing) and the effect of shear rate on viscosity (due to extrusion), by introducing eq. (4.2) as a scaling factor for eq. (4.3). The time and shear rate superposition model proposed in this work takes the following form:

$$\eta = K\dot{\gamma}^{n-1} \cdot \frac{1}{\eta^*(t_0)}(a_1 e^{b_1 t} + a_2 e^{b_2 t}). \tag{4.6}$$

Empirical parameters in eq. (4.6) are derived from oscillatory time sweeps, rotation shear rate sweeps, as well as volumetric flow rate measurements.

4.4 Results and discussion

4.4.1 Materials development and printability

Filament microstructure

The printability of the studied blends with different GM and FS loadings was mainly evaluated by observing the microstructure of printed filaments and the shape fidelity of the micro-scaffolds under μCT and SEM. Figure 4.3 highlights the μCT and SEM observations made on filaments extruded using a 250 μm tapered nozzle. Images assembled in the left column of Figure 4.3 show longitudinal cross-sections of studied blends obtained by μCT. SEM transverse cross-sections of extruded filaments for each blend are shown in the central column of Figure 4.3, with a corresponding digital enlargement in the right column. The absence of any significant resin-rich regions in Figure 4.3 confirms the homogeneous distribution of GM within the epoxy matrix. μCT images show that filament microstructure is highly dependent on the GM content. A dispersed material morphology is observed in the 5GM:10FS blend (Figure 4.3 (d)), but higher GM loadings as in the benchmark result in an inhomogeneous microstructure highlighted by the presence of crushed fillers (Figure 4.3 (p)).

Physical contact between fillers during mixing and extrusion possibly lead to GM crushing inside the extruded filaments. Debris and shells (white arcs between unbroken microspheres) are spread throughout the filaments in Figure 4.3 (j-r), indicating the occurrence of filler crushing above 10 wt.% GM ($\gtrsim$ 45 vol.% GM) in the 15GM:7FS and 20GM:6FS blends, and in the benchmark. A visual comparison of the effect of nozzle geometry on GM crushing is available in Figure B.3 using 250 μm tapered and cylindrical nozzles. For 0GM:12FS, 5GM:10FS, and 10GM:8FS blends, a similar material microstructure with no visible crushing is extruded for both 250 μm tapered and cylindrical nozzles. The presence of crushed GM for both types of nozzles is observed for 15GM:7FS, 20GM:6FS blends and the benchmark. Hence, due to filler integrity, only blends with 0 to 10 wt.% GM (0GM:12FS, 5GM:10FS and 10GM:8FS) were further investigated.

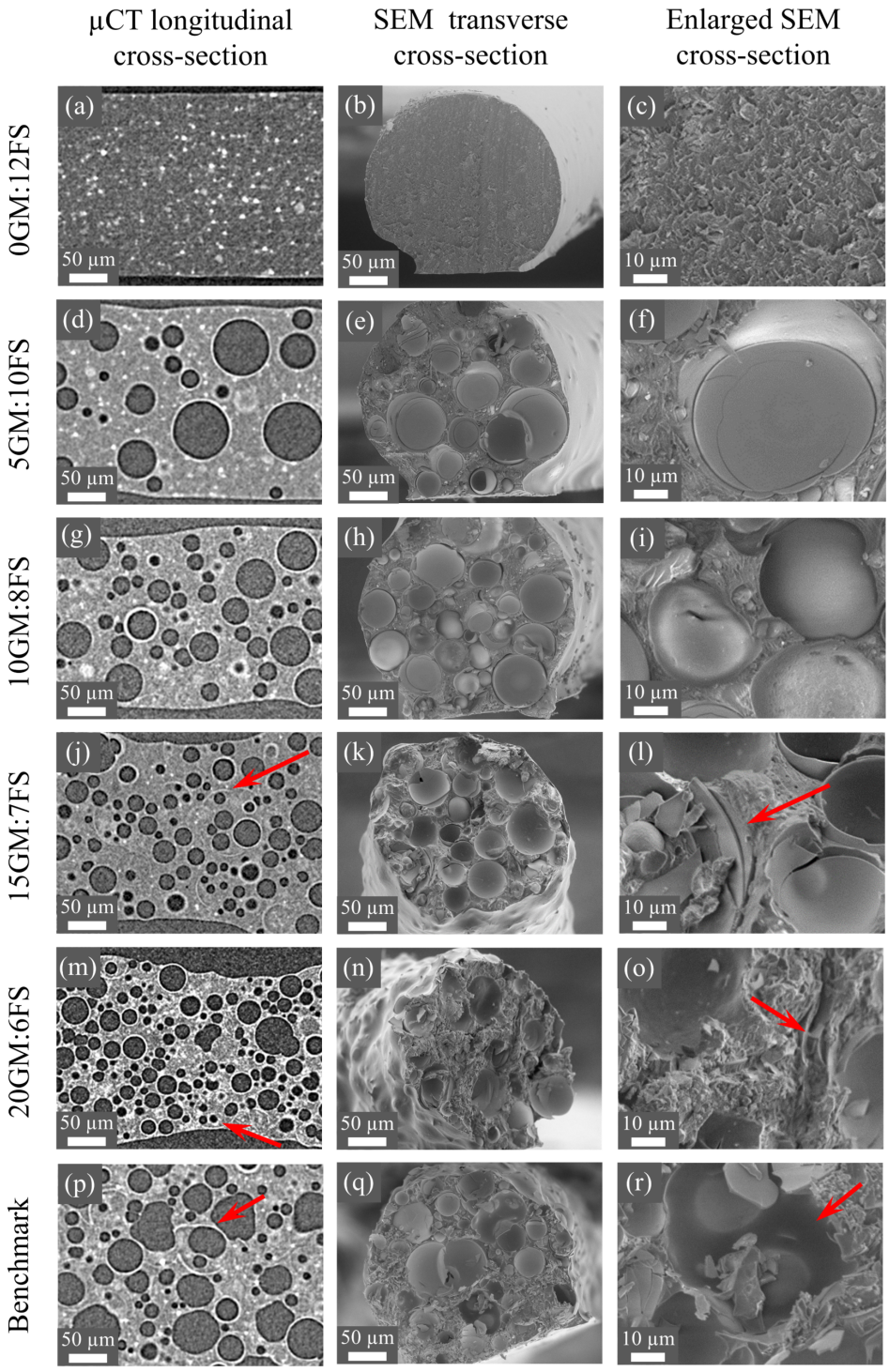

Figure 4.3 µCT and SEM cross-section images of filaments extruded with a 250 µm tapered nozzle at maximum system pressure for (a-c) 0GM:12FS, (d-f) 5GM:10FS, (g-i) 10GM:8FS, (j-l) 15GM:7FS, (m-o) 20GM:6FS blends and (p-r) the benchmark material. Detailed views (right column) were digitally enlarged to show the integrity of GM at low loadings and the microspheres crushing at high loadings, indicated by red arrows.

Shape retention after printing

Figure 4.4 shows SEM images of top and side views of 3D scaffolds printed using the three selected blends: 0GM:12FS, 5GM:10FS and 10GM:8FS. For the top views in Figure 4.4 (a-c), printed filaments form straight lines in agreement with the desired shape. Side views in Figure 4.4 (d-f) show that the three blends can produce spanning segments without visible bending deformation. Side views also demonstrate that individual filaments hold the circular shape after extrusion and stacking of multiple material layers. The uniformity in layer thickness for printed micro-scaffolds is also visible from Vid. S1 & S2. Top views indicate however that the printed geometry deviates slightly from the desired square shape with increasing GM content, as filaments appear to have a rougher surface with increasing microsphere content. A numerical printability score is used to assess the general shape fidelity for a fixed geometry using the developed blends.

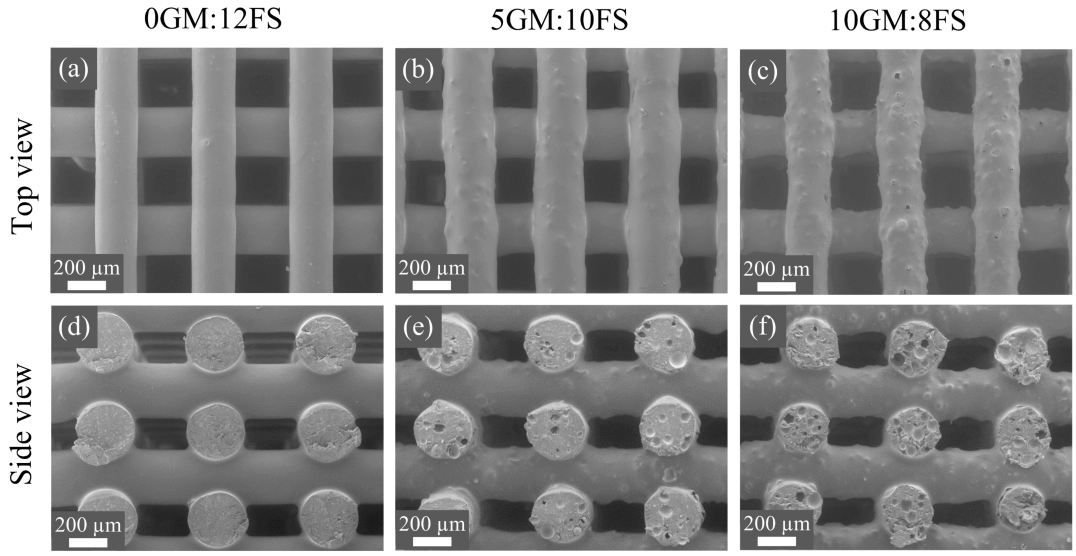

Figure 4.4 SEM images of 3D printed micro-scaffolds with top and side views, showing post-deposition shape retention. Blends presented are (a,d) 0GM:12FS, (b,e) 5GM:10FS, and (c,f) 10GM:8FS, respectively. The structures were printed at 50 mm.s^{-1} with a 250 µm pore size and 250 µm tapered nozzle.

First, filament circularity is estimated by comparing the average filament cross-section area A_p^f to the average cross-section perimeter of printed filaments l, according to the technique used by Ouyang et al. [142]. Circularity was used to gauge both the printability and the surface roughness in this work. Individual filament printability ψ^f is computed by measuring a circularity ratio based on side views as seen in Figure 4.4 (d-f). Hence, the ratio representing filament circularity is $\psi^f = 4\pi A_p^f / l^2$, where $\psi^f = 1$ designates a perfect circular shape, and $\psi^f < 1$ is indicative of circumferential filament deviations.

For interlayer shape retention, some deviation from the expected geometry is observed, as reflected by the slightly rounded corners at interlayer contact points in Figure 4.4 (d-f). A ratio $\psi^{side} = h_p/h_e$ comparing average printed interlayer height h_p to expected height h_e is calculated to assess the shape retention of pore features.

Following developments by M'Barki et al. [86], the average pore area A_p from a top view perspective enclosed by printed filaments is measured and divided by the expected design area A_e. A top view printability index is then defined as $\psi^{top} = A_p/A_e$, where $\psi^{top} = 1$ indicates that the projected area enclosed by four filaments is perfectly square.

To provide a quantitative basis to estimate the global printability index ψ for the blends, i.e. the ability to retain a given shape, the ratios developed so far are combined, such that

$$\psi = c_1\left[\psi^{top}\right] + c_2\left[\psi^{side} + \psi^{f}\right] = \frac{1}{2}\left[\frac{A_p}{A_e}\right] + \frac{1}{4}\left[\frac{h_p}{h_e} + \frac{4\pi A_p^f}{L^2}\right] \tag{4.7}$$

where weights c_1 and c_2 denote the relative importance of shape fidelity for top views and side views, respectively. The weights are distributed so that both directions normal and transverse to the layer stacking are equally important, that is, $c_1 = 1/2$ and $c_2 = 1/4$. Elemental printability indices ψ^{top}, ψ^{side} and ψ^{f} of the three selected blends are summarised in Table 4.2, and the combined effects thereof are computed as the weighted index ψ for each blend using eq. (4.7). Calculation errors from optical measurements are also indicated in Table 4.2 for all indices. Values for studied blends with filler crushing are also presented for comparison. The printability index is highest for the 0GM:12FS blend, which indicates that this blend closely matches (∼90% fidelity) the design geometry as per Figure 4.4 (a,d). Blends 5GM:10FS and 10GM:8FS seem to exhibit a similar ψ around 85%, slightly lower than the blend containing FS only. A decreased printability is attributed to the presence of GM that create ridges and valleys on the printed filaments.

Table 4.2 Printability indices of studied blends as an indicator of shape fidelity.

Blend	**Normal index,** ψ^{top} [-]	**Transverse index,** ψ^{side} [-]	**Filament index,** ψ^{f} [-]	**Weighted index,** ψ [-]
0GM:12FS	0.92 ± 0.03	0.88 ± 0.03	0.90 ± 0.05	0.90 ± 0.02
5GM:10FS	0.87 ± 0.10	0.84 ± 0.07	0.87 ± 0.04	0.86 ± 0.05
10GM:8FS	0.88 ± 0.06	0.75 ± 0.09	0.85 ± 0.05	0.84 ± 0.04
15GM:7FS	0.74 ± 0.14	0.70 ± 0.12	0.90 ± 0.02	0.77 ± 0.08
20GM:6FS	0.74 ± 0.11	0.70 ± 0.11	0.85 ± 0.05	0.76 ± 0.06

Processing map

Figure 4.5 (a) shows the printability of blends containing different loadings of GM and FS. Based on the printability study and microscopy observations of the printed micro-scaffolds, different printing zones were established. Figure 4.5 (b-d) show photographs of typical samples printed in this processing study. Zone I represents blends that are too liquid-like for the DIW process. Blends within this region either form droplets at the tip of the nozzle or may be shaped into filament, but immediately spread out on the substrate. In Zone II, increasing the GM content up to 20 wt.% (∼65 vol.% GM) or adding 5 to 8 wt.% of FS to the neat resin allows for moderate shape retention and vertical layer stacking. However, materials in Zone II feature a behaviour similar to Zone I, because filaments lose their circular shape and touch each other between printing and gelation. For example, the 20GM:0FS blend holds a scaffold structure for approximately 20 min, but printed features are lost prior to material cure, as seen in Figure 4.5(c).

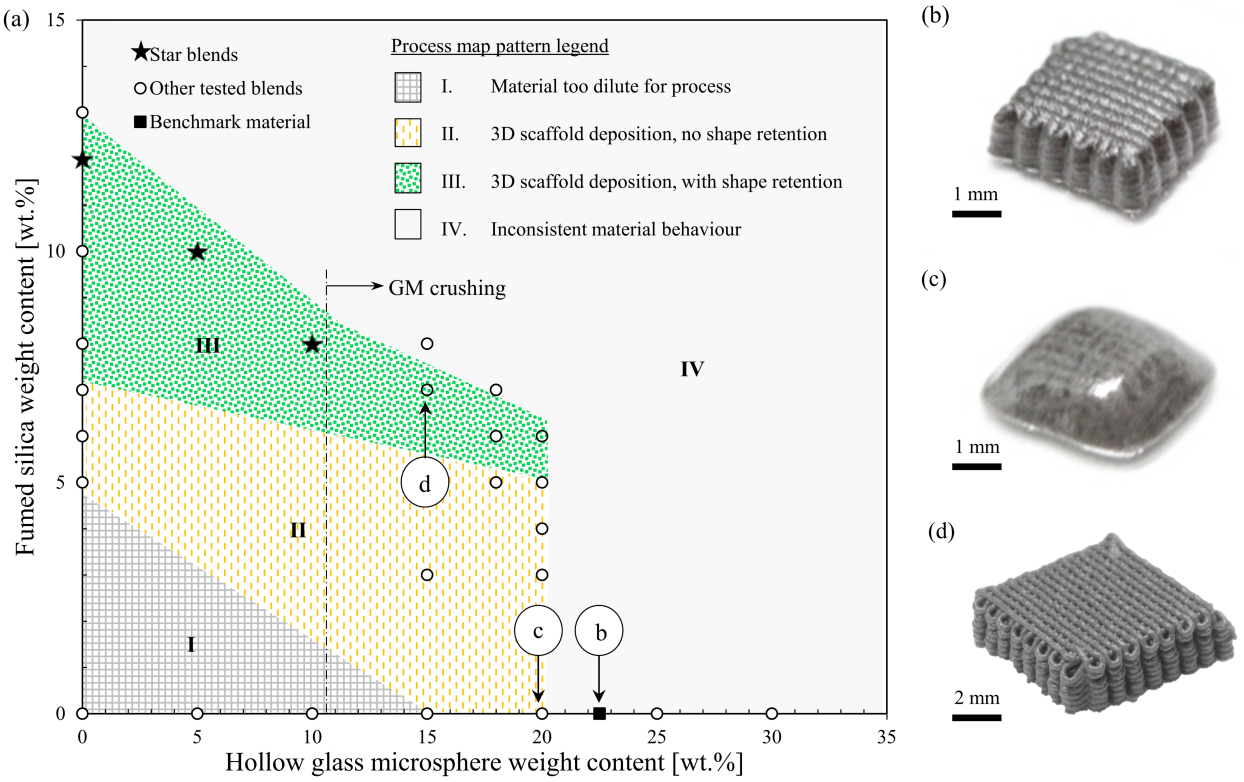

Figure 4.5 (a) Process map showing the printability of epoxy containing different loadings of GM and FS using a 250 μm nozzle. Roman numerals indicate the printability type and circled letters refer to printed scaffolds shown on the right. The three best materials are identified by a star symbol. (b) Benchmark with a Type IV printability. (c) 20GM:0FS blend with a Type II printability. (d) 15GM:7FS blend with a Type III printability (later rejected due to GM crushing).

Further increasing loadings of GM into Zone IV leads to an inconsistent printing behaviour most likely driven by three mechanisms: GM crushing, nozzle clogging, and high material rest viscosity. Prints using blends in Zone IV most often result in structures which are unable to keep the desired shape when extrusion is possible. For example, the benchmark in Figure 4.5 (b) loses all printed features within 10 min after printing. The loss of shape for the benchmark – and other blends containing over 20 wt.% GM – is attributed to the GM crushing observed earlier in Figure 4.3 (j-r). Indeed, upon crushing, air previously entrapped inside the hollow GM is replaced by resin in printed filaments, leaving fewer intact GM within the printed filaments to contribute to shape retention. The second mechanism for process inconsistency in Zone IV is unpredictable nozzle clogging that makes printing of micro-scaffolds difficult. Intermittent clogging for 250 μm nozzles is observed only at higher GM fractions (>20 wt.%, $\gtrsim$65 vol.%) and with 0 wt.% FS. The final mechanism for process inconsistency in Zone IV occurs for FS added beyond 20 wt.% of GM. Since FS has a known thickening effect [72], i.e. FS increases the rest viscosity of the neat resin, blends containing any FS and over 20 wt.% GM are not extrudable with the HP-7X system.

Blends combining less than 20 wt.% GM and at least 7 wt.% FS located inside Zone III can retain their printed shape until material cure. Materials such as 15GM:7FS in Figure 4.5 (d) are desirable because of their dimensional stability after printing, unlike blends without FS (Figure 4.5 (b,c)) which display poor shape retention after deposition. Filler integrity remains the main limitation of the 15GM:7FS and 20GM:6FS blends, with a moderate printability (ψ ~75%) compared to the three other studied blends. Shortlisted star blends 0GM:12FS, 5GM:10FS and 10GM:8FS, represented by stars symbols in Figure 4.5 (a), were then subjected to further rheological and acoustic characterisations.

4.4.2 Viscosity characterisation and modelling

Oscillatory shear rate sweeps

The effect of adding FS and GM on the rheological properties of the neat resin was investigated through oscillatory rheometry. Figure 4.6 (a) shows the storage and loss moduli with respect to the shear stress obtained by oscillatory strain sweeps over the shear strains of $\gamma = 0.01 - 100$ mm/mm. The relative measurement errors on G' and G'' are at most 0.7% and 0.5% across the dataset, respectively (not shown in Figure 4.6 (a)). The apparent yield stress τ_{YS} of the composite materials is defined at the crossover point between G' and G'' [133]. Without any fillers, the neat resin acts as a Newtonian fluid of near-constant viscosity (~14 Pa.s, data not shown). Adding both FS and GM into the neat resin changes the rheological behaviour from Newtonian to viscoelastic behaviour with a specific τ_{YS} as indicated by the vertical dashed lines in Figure 4.6 (a). The yield stress was found to increase

twelve-fold from 450 Pa to 5390 Pa with increasing FS loadings, i.e. from 0% (Benchmark) to 12 wt.% (0HGM:12FS). Although the presence of GM in the blends may increase τ_{YS}, the observed phenomenon appears more related to an increased FS content, rather than GM loadings. The observed increase indicates that τ_{YS} is more dependent on FS than on GM loadings. The addition of FS as the rheological modifier thus is crucial in providing the desired rheological properties for producing 3D scaffolds with high shape retention ability.

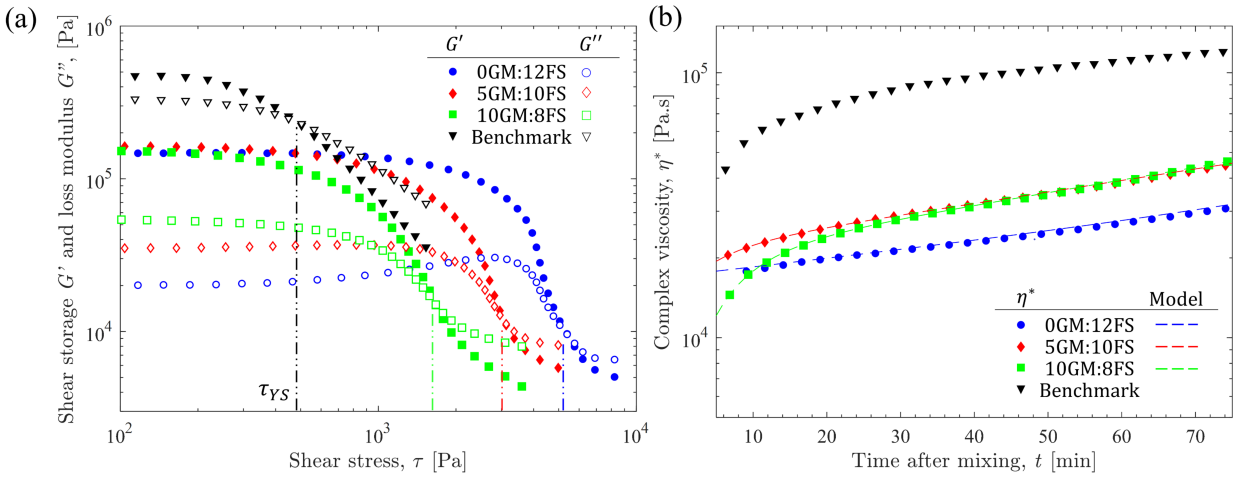

Figure 4.6 (a) Oscillatory rheological measurements of the shear storage and loss moduli for star blends and the benchmark with respect to shear stress; vertical lines indicate the yield stress τ_{YS}, defined where $G' = G''$. (b) Complex viscosity of the star blends and the benchmark over time after mixing; 1 data point shown per 5 measurements to enhance legibility. Fitted first-order isothermal cure models for the star blends (dashed lines) are overlaid for comparison. Data obtained by oscillatory rheometry (parallel plates with 1 mm gap, $\omega = 10$ rad.s^{-1}, at 25 °C).

Oscillatory time sweeps

Figure 4.6 (b) presents the effect of time on the complex viscosity η^* for the benchmark and the star blends, measured with oscillatory sweeps over time. The relative measurement error on η^* is at most 0.7% across the dataset (not shown in Figure 4.6 (b)). The η^* of all materials presented increases with time from mixing until the end of the test at 75 min. The benchmark continuously displays a higher η^* than the star blends for the duration of the test. From mixing up to 30 min, the benchmark experiences a steep increase in viscosity, whereafter η^* seems to increase at a constant rate. The star blends 5GM:10FS and 10GM:8FS also exhibit a steep increase in η^* (∼20%) from mixing until an inflection point at ∼15 min. In the same period, the 0GM:12FS blend η^* increases moderately by ∼8%. The 5GM:10FS and 10GM:8FS blends appear to have a similar η^* past 35 min and remain higher than that

of 0GM:12FS throughout the test. For example, after 45 min, the 0GM:12FS blend has η^*∼2.4·10^4 Pa.s (36% increase from $\eta^*(t_0)$), whereas the 5GM:10FS and 10GM:8FS blends have a η^*∼3.3·10^4 Pa.s (60% and 100% increase from $\eta^*(t_0)$, respectively). From 30 to 75 min, the η^* of 5GM:10FS and 10GM:8FS increases at an accelerating rate. An accelerating rate is problematic for DIW as the extrusion pressure must be increased at non-constant rate through time for prints with bigger dimensions. A more stable reaction seems to occur for the 0GM:12FS blend, as the η^* appears to increase steadily from mixing up to 30 min, then increasing at an accelerating rate.

The pot life t^* is defined as the time after mixing required to double the viscosity of a given blend after mixing ($\eta^*(t)/\eta^*(t_0) = 2$), which can also be obtained from Figure 4.6 (b). For the star blends, t^* is ∼90, 60 and 45 min, for 0GM:12FS, 5GM:10FS and 10GM:8FS respectively, against just 20 min for the benchmark. In this study, the pot life is deemed equivalent to the material working life, because the DIW process is highly dependent on viscosity. Longer working lives are desirable for DIW because more time is available to print the blends prior to material blockage within the syringe. Utilising eq. (4.2) to model the effect of time after mixing on η^* gives the dashed lines in Figure 4.6 (b), and the corresponding fitted parameters are presented in Table 4.3. The fits obtained up to 75 min show excellent agreement (coefficient of determination R^2> 0.995) with oscillatory data as they capture the exponential behaviour at the beginning of the cross-linking and near the accelerating reaction 30 min after mixing. The parameters in Table 4.3 can be used to predict by which factor $\eta^*(t)/\eta^*(t_0)$ the viscosity of a given blend has increased relative to its initial value, as explained in Section 4.3.1. Parameter errors in Table 4.3 pertain to the confidence intervals from the modelling step.

Table 4.3 Viscosity change parameters of star blends for the first-order isothermal cure model (data from Figure 4.6 (b)).

Blend	$\boldsymbol{a}_1$ [**Pa.s**]·10^4	$\boldsymbol{b}_1$ [**min**$^{-1}$]·10^1	$\boldsymbol{a}_2$ [**Pa.s**]·10^4	$\boldsymbol{b}_2$ [**min**$^{-1}$]·10^1	$\eta^*(t_0)$ [**Pa.s**]·10^4
0GM:12FS	1.704 ± 0.003	0.068 ± 0.002	0.011 ± 0.009	0.418 ± 0.044	1.760 ± 0.001
5GM:10FS	2.141 ± 0.007	0.099 ± 0.006	-0.773 ± 0.137	-1.518 ± 0.236	2.020 ± 0.001
10GM:8FS	2.036 ± 0.015	0.108 ± 0.001	-1.762 ± 0.132	-1.287 ± 0.083	1.640 ± 0.001

Rotational and capillary rheometry

Figure 4.7 reports the effect of shear rate on the viscosity of the star blends and the benchmark using data from rotational and capillary rheometry. Tests for low shear rates

($\dot{\gamma} < 10^0$ s^{-1}, solid symbols, rotational rheometry) and high shear rates ($\dot{\gamma} > 10^0$ s^{-1}), open symbols, capillary rheometry) provide the data for modelling material behaviour during extrusion. Taking the rotational rheometry data, the 0GM:12FS and 5GM:10FS blends display a higher shear rotational viscosity relative to the benchmark (~$5.5{\cdot}10^5$ Pa.s against $2.5{\cdot}10^5$ Pa.s, respectively). The opposite trend is observed for higher $\dot{\gamma}$ values, where the benchmark has a higher shear rotational viscosity than the star blends. For example, at $\dot{\gamma}$ ~$2{\cdot}10^3$ Pa.s (representing a printing speed of 50 mm.s^{-1}), the benchmark exhibits a viscosity of 141 Pa.s, higher than for the 0GM:12FS (87 Pa.s), 5GM:10FS (109 Pa.s) and 10GM:8FS (128 Pa.s) blends. The addition of FS and GM in star blends changes the base epoxy from a Newtonian fluid, for which the viscosity is mostly unaffected by shear rate (data not shown), to a shear-thinning system. Both star blends and the benchmark exhibit such shear-thinning behaviour shown by a negative slope in Figure 4.7. The data gap observed in the region of $\dot{\gamma} = 10^0 - 10^1$ s^{-1} is due to measurement instabilities in the rheometer caused by material yielding and separating from the parallel plates. Neither was it possible to bridge the discrepancy with the capillary method, because the onset of material flow through the nozzle required higher extrusion pressures.

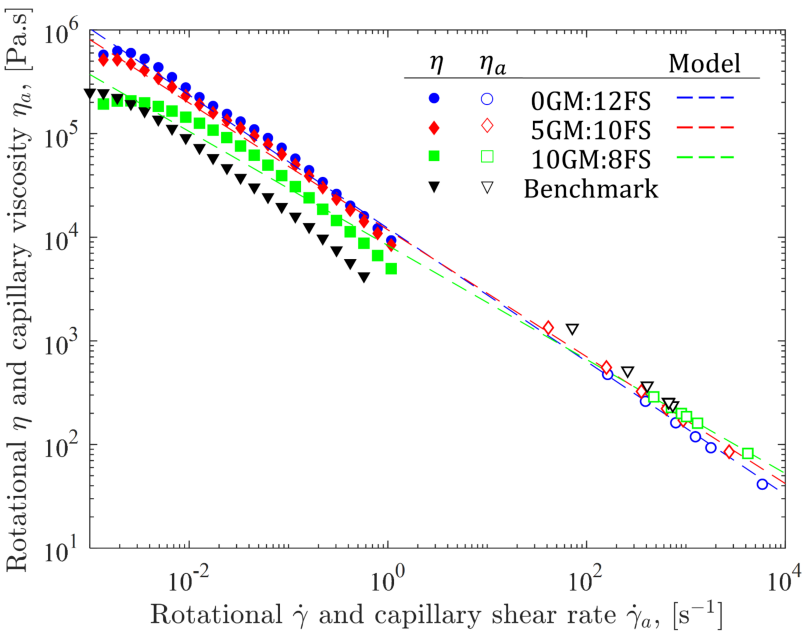

Figure 4.7 Rotational viscosity and apparent viscosity as a function of shear rate for the star blends and the benchmark. Solid symbols represent data obtained through rotational rheometry and open symbols report results from capillary rheometry using mass flow rate measurements. Benchmark data is shown as a reference. Fitted shear-thinning power-law models for the star blends (dashed lines) are also overlaid.

The combined apparent and shear viscosities of the star blends are fitted to $\dot{\gamma}$ using eq. (4.3), as shown by the dashed lines in Figure 4.7. The benchmark was not subjected to modelling as it is an unsuitable material for printing. The respective fitted power-law parameters n and K are presented in Table 4.4. Values for n underline the shear-thinning nature of the star blends as $n < 1$. The viscosity-shear rate fits in Figure 4.7 show very good agreement ($R^2 > 0.985$) with the rheometry data points in both low and high $\dot{\gamma}$ regions, and confirm the choice of a power-law type viscosity model to describe the star blends. A complete material model tracking the viscosity of each star blend is obtained by combining the shearing effects of extrusion and the time elapsed since mixing, as expressed by eq. (4.6). All the parameters from empirical fits listed Table 4.3 and Table 4.4 can be used to predict the flow behaviour of the star blends during the high-speed printing phase of the DIW process. Parameter errors in Table 4.3 pertain to the confidence intervals from the modelling step.

Table 4.4 Parameters of the power-law fits for the star blends (data from Figure 4.7).

Blend	**Flow index, n [-]**	**Consistency index K [Pa.s^n]**
0GM:12FS	0.358 ± 0.010	12 188 ± 10
5GM:10FS	0.388 ± 0.008	11 784 ± 10
10GM:8FS	0.450 ± 0.012	8 330 ± 1

High-speed printing

The printing speed for a given pressure gradient ΔP and time after mixing t can be predicted from the time-shear rate viscosity model of eq. (4.6) using the fitted parameters obtained from oscillatory, rotational and capillary rheometry. First, the viscosity change ratio $\eta^*(t)/\eta^*(t_0)$ is estimated for t through eq. (4.2). The flow rate Q_T in eq. (4.4) is then computed with ΔP and a known nozzle geometry. Further, $Q_T|_t$ is obtained by the ratio of Q_T over the viscosity change factor, to account for a lower flow rate with increasing time. From the definition of volumetric flow rate, the corresponding printing speed prediction u is calculated dividing $Q_T|_t$ by the nozzle outlet area A_o.

Figure 4.8 compares the measured printing speeds of the star blends against the predicted speeds for a 250 μm tapered nozzle for three different times after mixing using eq. (4.4) and the method described above. The validation step shown was performed at the maximum system pressure of 4.55 MPa at 10 min (10GM:8FS), 20 min (0GM:12FS) and 45 min (5GM:10FS) after mixing. For measured speed values, the error bars represent standard deviations resulting from taking the average of measured filament diameters (see method in

Section 4.2.2). Errors for the predicted speeds are derived from parameter confidence intervals and error propagation obtained during modelling. Measured printing speeds and speeds predicted by the time-shear rate model appear to be in good agreement for the selected time steps as no significant differences were found. The model therefore offers a satisfactory description of the flow behaviour through time for the star blends when printing with tapered nozzles.

Up to 15 min after mixing, the star blends were printed between $110 - 175$ mm.s^{-1} at 4.55 MPa, with the highest speed achieved by the 0GM:12FS blend (175 mm.s^{-1}), followed by the 5GM:10FS (130 mm.s^{-1}), and 10GM:8FS (110 mm.s^{-1}) blends, respectively. Past 90 min, printing speeds are significantly lower because higher viscosities restrict the flow rates (i.e., 96 mm.s^{-1}, 77 mm.s^{-1}, and 36 mm.s^{-1} for the 0GM:12FS, 5GM:10FS and 10GM:8FS blends, respectively). For comparison, Figure B.2 shows the significance of nozzle geometry on material flowability when printing with tapered nozzles. Tapered nozzles greatly enhance the ability of the materials to flow, allowing for high-speed deposition compared to $\sim$1 mm.s^{-1} when using cylindrical tips with the same inner tip diameter at the nozzle exit.

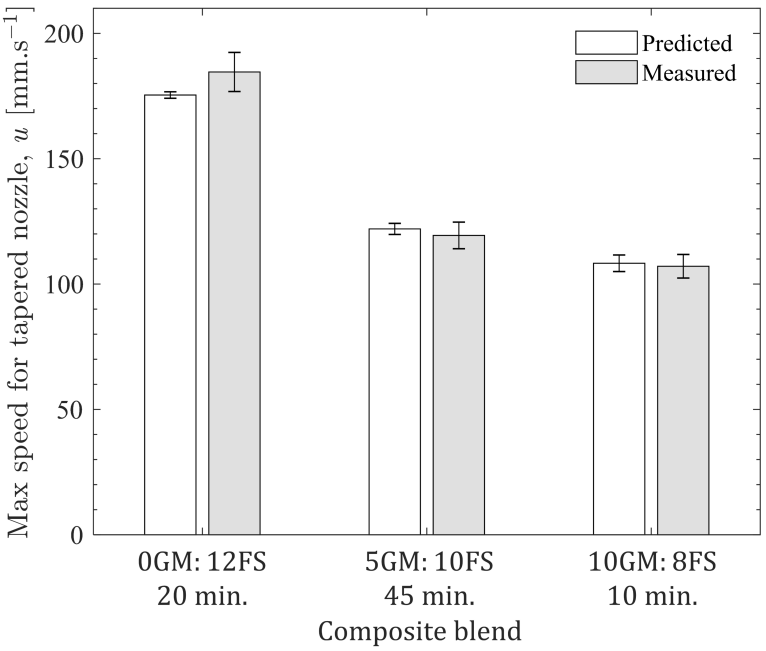

Figure 4.8 Comparison between predicted and measured printing speeds for the star blends at maximum system pressure (4.55 MPa) through a 250 μm tapered nozzle for different times after mixing. Predicted values are computed from the viscosity models using parameters and their respective confidence intervals. Presented model validation times are $t = 20$ min for 0GM:12FS, $t = 45$ min for 5GM:10FS, and $t = 10$ min for 10GM:8FS. Measured speeds taken for a filament diameter equal to the nozzle tip diameter based on optical microscope measurements.

4.4.3 Acoustic absorption

Boulvert et al. developed algorithms to predict the sound absorption coefficient of micro-scaffolds, using the Johnson-Champoux-Allard-Lafarge (JCAL) model. The six JCAL model parameters (i.e., structure porosity, tortuosity, characteristic thermal and viscous lengths, and thermal and viscous permeabilities) are obtained numerically using finite element simulations [120]. Based on this work, the micro-scaffolds geometry is designed with a target pore size of 300 µm, 250 µm diameter filaments and 0.2 mm layer height.

Figure 4.9 (a) shows a representative sample for the sound absorption characterisation of micro-scaffolds printed at 50 mm.s^{-1} using the 5GM:10FS blend, with a magnified top view in Figure 4.9 (b). The printing accuracy was evaluated by first measuring the average pore size in Table 4.5 (50 locations both on the top and bottom layers of each printed 5 mm thick section). The average porosity of printed sections for star blends was also assessed. The porosity ϕ refers to the volume of functional voids forming the micro-scaffold [62], and is defined as

$$\phi = 1 - \frac{\rho_{app}}{\rho_{bulk}} \tag{4.8}$$

where ρ_{app} is the mass of a 5 mm thick sample divided by its cylindrical volume, and ρ_{bulk} is the density of the blend from pycnometer measurements. As the bounding cylindrical shell (outer wall) does not contribute to sound dissipation, the volume does not include the outer walls, leading to a porosity of 45%. The average pore size from measurements taken on the top and bottom layers of each sample section and the porosities calculated with eq. (4.8) are reported in Table 4.5. Both pore size and ϕ appear to match the target value for the 0GM:12FS and 10GM:8FS blends; however, the values deviate for 5GM:10FS.

Figure 4.9 (c) shows measured and simulated absorption coefficients α for printed micro-scaffolds using the star blends tested in the range of frequencies from 500 to 6000 Hz with a Kundt's tube. The simulated absorptions were obtained using the JCAL model. Simulated geometrical parameters were selected as the target printed values, i.e. 25 mm high stacks with 300 µm pores, and the true outer wall thickness of 1.2 mm. The average sound absorption $\bar{\alpha}$ in Table 4.5 is over 0.6 for the tested frequency range (calculated from three replications per 25 mm stack with a 1 Hz discretisation), compared to the simulated 0.52 average absorption. The difference in average absorptions is attributed to surface roughness, which affects the viscous and thermal losses in the micro-scaffolds by increasing the contact surface area between the air and the structure. More surface area could explain why $\bar{\alpha}$ is higher for the star blends than the simulation, as the increase in filament roughness observed in Figure 4.4 (a-c) results in a higher absorption, on average, compared to perfectly circular filaments assumed by the JCAL simulation [120, 143].

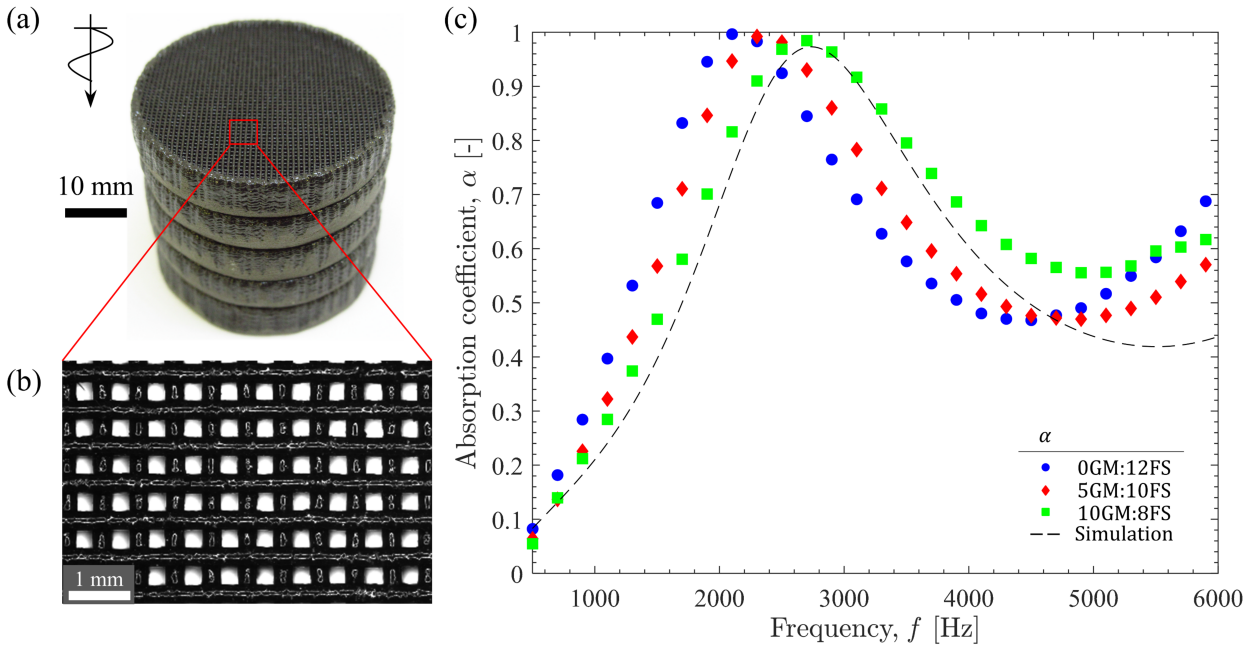

Figure 4.9 (a) Representative micro-scaffold sections (30 mm diameter) stacked in a 25 mm thick sample (∼250 µm filament diameter, ∼300 µm pore size, and 50 mm.s^{-1} printing speed using 5GM:10FS). Arrow points the direction of soundwave propagation for Kundt's tube tests. (b) Optical microscope image of the top layer of the acoustic stack. (c) Hard-backed acoustic absorption coefficients of the star blends compared to the simulated absorption using the JCAL model (dashed line). Absorption values shown were averaged from 3 replications; 1 data point shown per 200 measurements to enhance legibility.

Between 1900 and 3000 Hz, an excellent absorption of $\alpha > 0.95$ was measured for the star blends, as expected from the simulation. Printed structures also exhibit a near perfect peak acoustic absorption ($\alpha_p > 0.98$) in the vicinity of the peak frequency f_p ∼2400 Hz, yet the peak occurred at frequencies lower than predicted for the simulated geometry. The shift in peak frequency between materials, which ranges from ∼40 Hz to over 500 Hz, is attributed to the difference in stack heights, pores sizes and porosities highlighted in Table 4.5. The actual stack heights range from 25.4 mm (10GM:8FS) to 26.4 mm (0GM:12FS), all higher than the target 25.0 mm that was simulated. A taller stacking contributes to a significant shift of f_p towards lower frequencies compared to the simulated curve in Figure 4.9 (c), according to the quarter-wave principle [144]. A secondary effect attributed to the spectrum of pore size among printed samples, also contributes to shifting f_p. Due to the time required to print the acoustic sections (∼20 min), material viscosity effectively changes inside the syringe (+12% for 0GM:12FS, +27% for 5GM:10FS, and +46% for 10GM:8FS). As a result, the extrusion pressure had to be manually adjusted throughout the manufacturing process.

Filaments with an inconsistent size were obtained by trying to keep an extrusion flow rate matching the constant printing speed, leading to variable pore size and porosity. Average top and bottom layer pore size and the average thereof, outlined in Table 4.5, give an indication of the difficulty in controlling geometrical features for time-dependent materials. Reported pore size errors represent standard deviations obtained from multiple optical microscopy measurements. For an assembled 25 mm stack, the pore size varies up to 40% (for the 5GM:10FS blend) between top and bottom layers. The total average pore size of printed sample ($\sim$275 µm) may somewhat contribute to the f_p shift away from the simulated curve (300 µm pores), because smaller pores are more effective for absorbing lower frequencies. As for the simulated curve, the JCAL model considers that printed filaments are perfectly circular, when in reality the printed star blends exhibit a varying degree of surface roughness (Figure 4.4 (a-c)). A higher surface roughness increases the tortuosity of the micro-scaffold, and thus further contributes to shifting f_p towards lower frequencies with respect to simulated absorptions [120, 145].

Effective absorption bandwidths are used to define the range of acceptable absorption frequencies, around a resonance frequency peak. Acoustic damping ratios ζ are shown in Table 4.5, such that

$$\zeta = \frac{|f_1 - f_2|}{2f_p} \tag{4.9}$$

where f_1 and f_2 represent the two half-power frequencies taken at $\alpha_p/\sqrt{2}$ for each sample [146]. From eq. (4.9), the damping ratios for the star blends ($\sim$0.35) exhibit some scattering and are all higher than the predicted value, most likely due to the geometric discrepancies seen from the average pore size and stack heights for printed samples. Therefore, the difference between simulated and experimental sound absorption coefficients arise from said geometric discrepancies, i.e. pore size, stacking height and surface roughness (resulting from the presence of GM in the filaments). The impact of each parameter on the overall sound absorption properties could not be assessed separately. Nevertheless, the characterisation of sound absorption capabilities demonstrates that the star blends can be used to print structures with a fixed pore size and porosity to obtain a predictable performance in terms of acoustic absorption coefficients, peak frequency, and damping ratio.

Table 4.5 Geometrical features averaged from top and bottom layers, and Kundt's tube results with JCAL simulation parameters for printed blends.

Blend	**Stack height [mm]**	**Top layer pore size [μm]**	**Bottom layer pore size [μm]**	**Average pore size [μm]**	**Porosity, ϕ [-]**	**Average absorption, $\bar{\alpha}$ [-]**	**Peak frequency, f_p [Hz]**	**Damping ratio, ζ [-]**
0GM:12FS	26.4 ± 0.3	305 ± 9	331 ± 12	318 ± 24	0.45 ± 0.02	0.624 ± 0.002	2154 ± 9	0.354 ± 0.002
5GM:10FS	26.0 ± 0.3	286 ± 13	211 ± 13	251 ± 42	0.38 ± 0.02	0.600 ± 0.003	2350 ± 7	0.347 ± 0.004
10GM:8FS	25.4 ± 0.3	302 ± 22	279 ± 12	290 ± 27	0.45 ± 0.02	0.633 ± 0.006	2687 ± 9	0.366 ± 0.004
Simulation	25.0	300	300	300	0.45	0.520	2730	0.320

4.4.4 Lightweight properties

The star blends containing GM are advantageous due to their lower bulk density (973 kg.m^{-3} for 5GM:10FS and 837 kg.m^{-3} 10GM:8FS, from Table 4.1) compared to the neat resin (1170 kg.m^{-3}). The 0GM:12FS blend has a higher bulk density (1272 kg.m^{-3}) than the neat resin. However, higher bulk densities compared to the benchmark (505 kg.m^{-3}) are compensated by printing porous structures such as the micro-scaffolds used for sound absorption. Here, an arbitrary volume of the benchmark, which can only be used as bulk material, is replaced by a printed porous structure containing only 55% of lightweight material. For example, the 10GM:8GFS blend allows for a weight saving of 25% with the selected micro-scaffold geometry; with more FS in the 5GM:10GFS blend, the weight saving is 13%. As for the 0GM:12GFS blend, a weight gain of 13% is obtained with the selected geometry, which might be offset by the new acoustic functionality previously impossible with bulk the benchmark volume.

4.5 Conclusions

In this work, lightweight composite materials made of aerospace-grade epoxy with hollow glass microspheres and/or fumed silica were developed for DIW. High printing speeds in the range of $110 - 175$ mm.s^{-1} were reached using our star blends 0GM:12FS, 5GM:10FS and 10GM:8FS with 250 μm tapered nozzles and extrusion pressures up to 4.55 MPa. The printing speeds achieved herein are a significant improvement from published data, previously limited to 40 mm.s^{-1} and larger nozzles. Star blends exhibit a good shape retention with a printability index ψ>80% when stacked into 3D micro-scaffolds without filler crushing. The 0GM:12FS blend has a smoother surface roughness than the 5GM:10FS and 10GM:8FS blends, allows for finer details to be printed and higher printing speeds, but is heavier. By contrast, the 10GM:8GFS is lighter than the 0GM:12FS and 5GM:10FS blends yet displays a shorter working time. Acoustic peak absorption coefficients above 0.98 were obtained experimentally in printed micro-scaffolds, for frequencies ranging between 2100 and 2700 Hz.

The transient material model developed in this work relates the effects of printing speed and curing time to the viscosity of the star blends. The model can be used to predict the required extrusion pressure for a desired printing speed, for example, in developing industrial large-area printing. However, the current infrastructure restricts the part build volume and the geometric fidelity of printed features. An improved large-volume printing infrastructure could feature a self-correcting capability, relying on the transient model to adjust the extrusion pressure so to better control the accuracy of the DIW process. High-speed printing increases the throughput of the process, and thus paves the way for depositing large-area

structures in less time than previously available composite materials.

The sound absorption functionality of printed blends demonstrated in this work has potential applications, such as aircraft noise reduction. Hence, once the best trade-off blend is identified in future works, large area structures with optimised broadband acoustic designs may be investigated, for instance by printing on non-planar surfaces (e.g., on aircraft engines). Additional studies (e.g., mechanical tests and ageing) will help in determining which blend features the best trade-off between physical properties, manufacturing capabilities and functional constraints in the context of industrial-scale aerospace applications.

CHAPTER 5 GENERAL DISCUSSION

Chapter 4 addressed most of **O1** from a bottom-up approach, using the neat resin with a modified filler content to obtain printable composite materials. The first part of Chapter 5 thus completes **O1** with unpublished data, identifying suitable proportions of PJ (petroleum jelly) in the benchmark, which enable micro-scaffold DIW. The second part of Chapter 5 discusses **O2** based on preliminary results, which were obtained in collaboration with another member of the FACMO Chair. The effects of different loadings of PJ on abradability are estimated through pullout tests and microhardness measurements. As for the star blends, an abradability assessment, also through pullout and microhardness studies, is presented and discussed.

5.1 Methodology

5.1.1 Printability study

The printability of the benchmark containing 2.5, 5, 7.5, 10, 12.5 & 15 wt.% PJ was assessed by the same method as for the neat resin filled with GM and FS described in Section 4.2.2. At a given pressure, linear displacement speeds were adjusted according to the achievable flow rate to deposit straight, smooth and continuous ∼250 µm diameter filaments on glass substrates. Filament width measurements were made using an optical microscope (SZX12, Olympus, USA) and post-processed with ImageJ. The clearance between the nozzle tip and the substrate, i.e. the first layer height, was set at 0.26 mm; subsequent layer height was 0.20 mm. Hand-fractured cross-sections of extruded filament were observed under SEM (TM3030, Hitachi, USA) with a 15 kV supply voltage. No chrome coating was required on the fracture surface of those filaments to produce clear images.

5.1.2 Material density

The bulk density of the benchmark with different loadings of PJ was obtained using an AccuPyc II 1340 helium gas displacement pycnometer (Micrometrics, USA). For a given blend, about 1 g of cured bulk material was weighed, inserted into a 3.5 cm^3 chamber, and placed inside the apparatus. The densities presented were averaged from 100 data points.

5.1.3 Pullout tests

Prior to printing, aluminium substrates (7075-T6 G11, McMaster, USA) were sanded using a P120 grade paper to remove surface oxidation, and wiped clean with acetone to remove

contaminants. One-layer bulk coatings of the benchmark containing $0-15$ wt.% PJ and the star blends were printed onto the substrates using a cylindrical nozzle of $D_o = 1.54$ mm. The coatings were allowed to cure for 48h, after which the top surface was sanded with a ScotchBrite™ sponge (3M™, USA). A dolly of 20 mm diameter was then glued on the coating with an epoxy adhesive (Hysol 1C, Loctite™, USA) and left to cure for 48h. Pullout tests were then performed in accordance with ASTM 4541-17. The pullout rate was set at 1 MPa.s^{-1} using an adhesion tester (PosiTest AT-A, DeFelsko, USA). Failure types were determined using image analysis (ImageJ) based on optical microscope observations. The portion of bright areas on the dolly was added to the portion found on the coating surface to calculate the percentage of adhesive failure. The test was performed 4 times for each formulation.

5.1.4 Micro-hardness tests

Samples printed for the pullout tests were also used to take micro-hardness measurements in regions away from the fractured zone, on the virgin coating surface. Micro-hardness tests for the benchmark containing different loadings of PJ as well as the star blends were conducted in accordance with ASTM 2240-15 using a hand-held Shore D durometer (AD-100-D, Checkline, USA). The sampling area was sanded with a ScotchBrite™ sponge (3M™, USA), and the indentor tip was pressed against the coating to obtain a micro-hardness reading. The test was performed 5 times for each formulation.

5.2 Results and discussion

5.2.1 Printability study - Modified benchmark

Figure 5.1 shows a comparison of extruded filament cross-sections under SEM and photographs of printed 3D micro-scaffolds for both 250 μm cylindrical and tapered nozzles. From the photographs, the micro-scaffolds exhibit a varying degree of compliance with the target geometry (250 μm pore size). Localised poor shape retention is visible in regions where pores features are lost for ≤10.0 wt.% PJ (cylindrical nozzle) and ≤2.5 wt.% PJ (tapered nozzle). Closer inspection of extruded filaments using SEM reveals that the benchmark is able keep a circular shape after deposition for loadings ≥12.5 wt.% PJ (cylindrical nozzle) and ≥7.5 wt.% PJ (tapered nozzle). Nevertheless, significant GM crushing is observed in the cross-sectional views for all PJ loadings. Filler crushing is manifested by the semi-circular debris embedded in the filaments. Such filler behaviour was expected based on the observations in Section 4.4.1. Crushing was stated to occur for ≥10 wt.% GM, regardless of nozzle geometry, and the lowest GM content is ∼19 wt.% corresponding to the 15 wt.% PJ

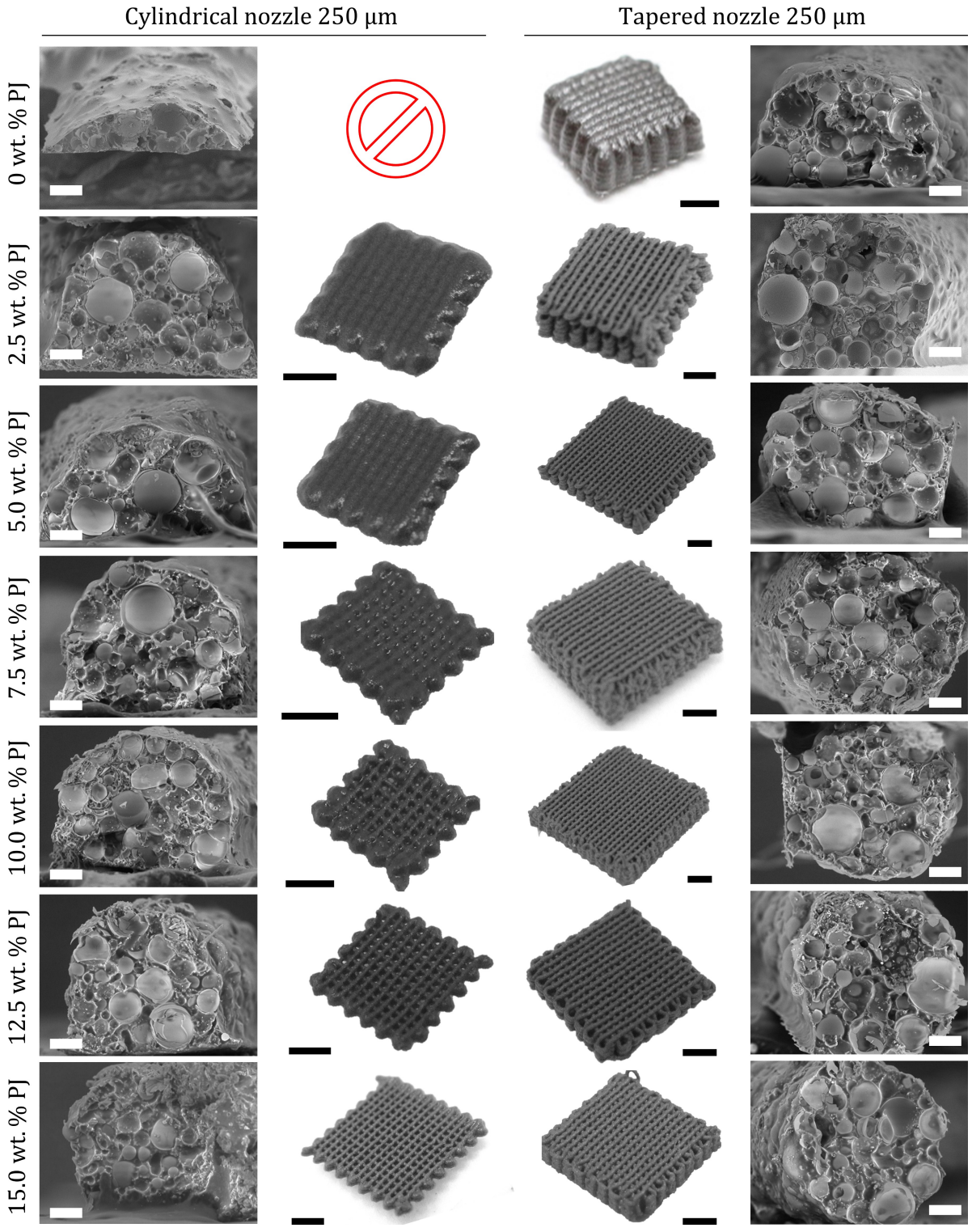

Figure 5.1 Printability assessment for the benchmark containing $0 - 15.0$ wt.% PJ, using 250 µm cylindrical and tapered nozzles. SEM images are placed in the left and right columns; corresponding scale bars represent 50 µm. Macroscopic photographs are presented in the two central columns; corresponding scale bars represent 5 mm.

formulation. Beyond a certain PJ loading threshold, the addition of PJ seems to counteract the loss of printed shape resulting from the presence of crushed GM in the benchmark. Therefore, the printed benchmark can be shaped into micro-scaffolds with a satisfactory shape retention using both 250 μm cylindrical and tapered nozzles when at least 12.5 wt.% PJ and 7.5 wt.% PJ are added, respectively. It must be noted that stacking height was not considered in this printability assessment, which may lead to different conclusions if taken into account.

5.2.2 Material density - Modified benchmark

Table 5.1 summarises the measured densities of the benchmark containing various loadings of PJ. The densities increase gradually with the PJ content, as expected. For 15 wt.% PJ, the material density rises marginally by 12.7% from 505 kg.m^{-3} to 569 kg.m^{-3}, as a portion of lightweight GM in the benchmark is diluted with PJ. The estimated GM loadings indicate that the minimum GM weight content (19 wt.%) is above the 10 wt.% threshold where filler crushing during printing starts to occur.

Table 5.1 Calculated GM loadings with measured cured density of the studied formulations.

Nominal PJ content, [wt.%]	**Calculated GM content, [wt.%]**	**Measured cured density, ρ [kg.m^{-3}]**
0 (Benchmark)	22.5	505.0
2.5	21.9	528.0
5.0	21.4	544.4
7.5	20.8	556.5
10.0	20.3	560.9
12.5	19.7	564.0
15.0	19.1	569.0

5.2.3 Pullout tests - Modified benchmark

Figure 5.2 (a) shows a representative fracture surface obtained during pullout tests, together with the test dolly. Figure 5.2 (b) reports the percentage of cohesive coating failure and the pullout strength for different loadings of PJ in the benchmark. The percentage of cohesive to adhesive failure (Cohesive% = 100%−Adhesive%) seems to decrease with higher PJ content in the benchmark. The proportion of failure is predominantly cohesive for loadings up to 7.5 wt.% PJ (above ∼60%), thereafter shifting to a mostly adhesive failure. An almost completely adhesive failure was found for the benchmark containing 15 wt.% PJ.

The pullout strength can be correlated to the ultimate tensile stress the material, and thus give an indication about the abradability level of that material [25, 53]. Here, no

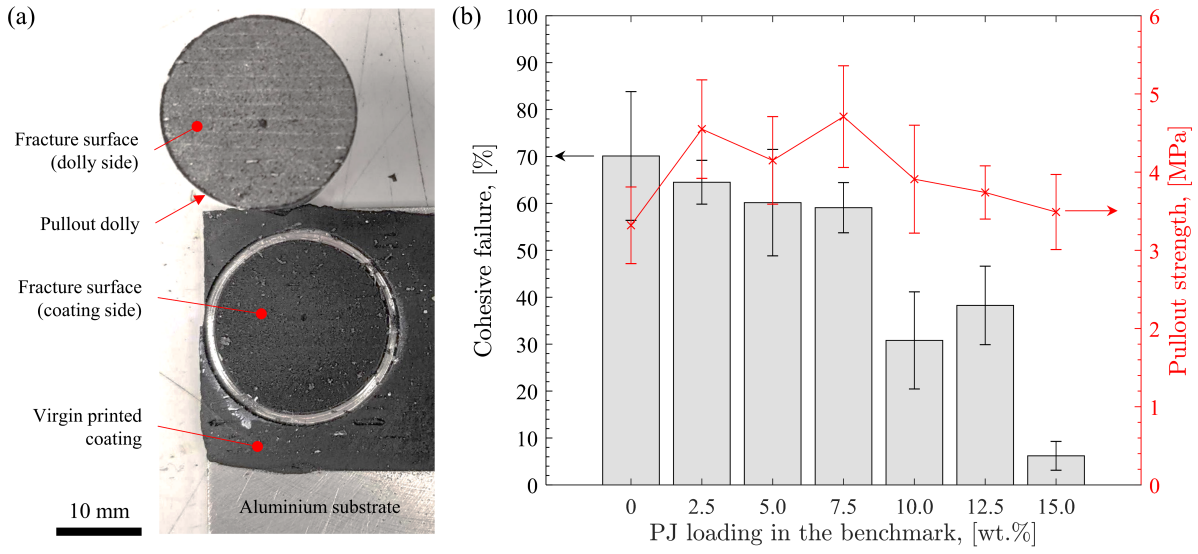

Figure 5.2 (a) Representative fracture surface for adhesion tests, here for of the the benchmark containing 15 wt.% PJ, printed with a 1.54 mm nozzle on the Aerotech deposition system. (b) Comparison of the cohesive failure percentage and pullout strength of the benchmark with different loadings of PJ. Error bars represent the 95% confidence intervals obtained from 4 replications.

significant difference in pullout strengths was measured in the studied range of PJ loadings, which is 4.0 $\pm$ 0.5 MPa on average, suggesting a similar level of abradability.

Although the addition of PJ does not appear to affect the pullout strength of the modified benchmark compared to the baseline product, the type of mechanical failure is increasingly adhesive in nature with higher PJ content at the 95% confidence level. A higher percentage of adhesive failure entails that fractures tend to occur at the interfaces rather than within the bulk of the coating, which is not desirable in this project. Rather, a cohesive failure is sought in abradable materials for mainly two reasons:

1. Particles removed by adhesive wear tend to transfer to the blade tip and aggregate, instead of being ingested downstream. These aggregates could plough through the coating as the blade revolves, thus contributing to premature coating wear, shroud grooving and friction heating [17]. The aggregates may also form particles large enough to cause damage to downstream components [25].

2. Coating fracture (usually by shearing for abradable materials) may occur beneath the blade-to-coating contact surface for materials failing in an adhesive mode. In such case, a layer of material which is thicker than the incursion depth may be removed by the blade [5]. As a result, the aerodynamic seal may exhibit a lower performance compared to its design point, as the true gap height could be higher than expected [24].

Consequently, PJ loadings >7.5 wt.% in the benchmark might be unsuitable to obtain a material fulfilling an abradable functionality, based on the adhesion failure mode observed.

5.2.4 Micro-hardness tests - Modified benchmark

Figure 5.3 (a) shows a comparison of the Shore D hardness for the benchmark containing different loadings of PJ. The 0 wt.% PJ material has a hardness of 54.4 ± 0.8 D. On average, the Shore D hardness for $2.5 - 15.0$ wt.% PJ is 53.0 ± 0.9 D (± the standard deviation), which is not significantly different than the baseline benchmark. Figure 5.3 (b) reports the normalised Shore D hardness values taken from Figure 5.3 (a), relative to the baseline benchmark. The horizontal lines represent the 95% confidence interval for the normalised experimental hardness values. There is no clear relationship between the measured hardness and the PJ content; increasing the amount of PJ does not appear to significantly affect the Shore D hardness of the benchmark, at the 95% confidence level.

Consider the PJ loadings for minimal material density (Table 5.1), yet that allow for a satisfactory shape retention based on observations from Figure 5.1. For printing using tapered nozzles, the presence of 7.5 wt.% PJ in the benchmark has no significant incidence on the cohesive failure percentage, pullout strength or Shore D hardness (Figures 5.2 and 5.3). In the case of the printing with a cylindrical nozzle, incorporating 12.5 wt.% PJ does not affect either the pullout strength or the Shore D hardness of the benchmark, but significantly degrades the interfacial resistance (lower cohesive percentage). The benchmark containing 7.5 wt.% PJ seems to be the only formulation with a potential for abradability, but it is only printable using a 250 μm tapered nozzle.

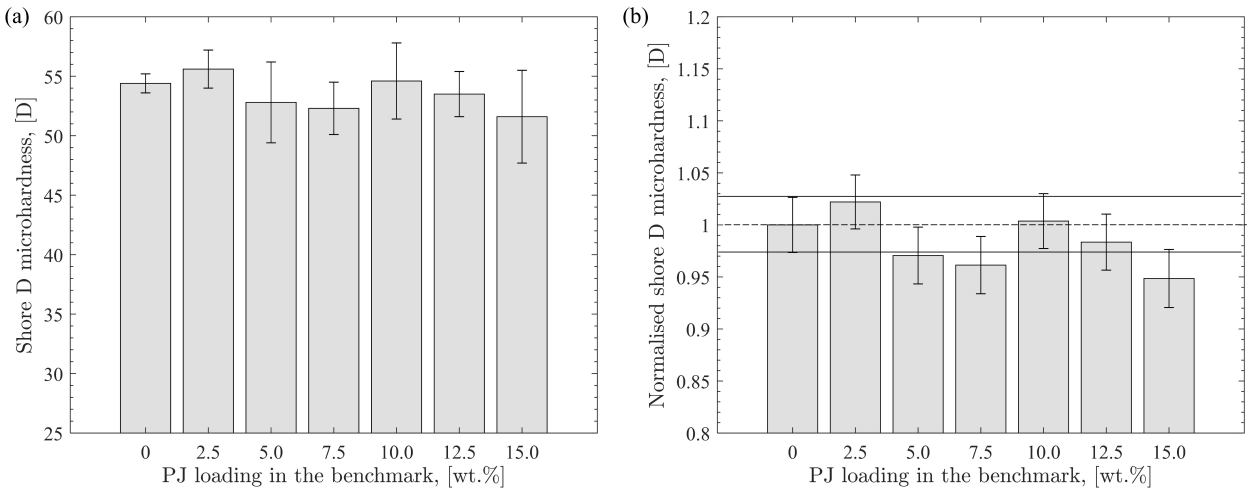

Figure 5.3 Comparison of the (a) Shore D hardness and (b) Normalised Shore D hardness for the benchmark containing different loadings of PJ. Error bars represent the 95% confidence intervals obtained from 5 replications.

Nevertheless, the occurrence of GM crushing during printing cannot be overcome by the addition of PJ, irrespective of the geometry of the nozzle and PJ weight content. Considering that the hollow GM provide a degree of porosity to the coating, and that abradability is highly dependant on the porosity, GM crushing is expected to be detrimental to the abradable functionality of the materials, including the 7.5 wt.% PJ formulation. A larger nozzle diameter could alleviate the crushing phenomenon, but a loss of performance in the sound absorption functionality is expected for higher filament diameters with other micro-scaffold geometrical parameters held constant [3, 120]. Therefore, adding PJ to the benchmark is not a good solution to attain the objectives of this project whatsoever.

5.2.5 Analysis of the modified benchmark

To render the benchmark printable, PJ must be present to the amount of 12.5 wt.% and 7.5 wt.% for extrusion using 250 μm cylindrical nozzles and tapered nozzles, respectively. From the mechanical properties above, even though the pullout strength and micro-hardness do not appear to be affected by the presence of PJ, adhesive failure and GM crushing constitute two major impediments to purse testing with the benchmark containing PJ. In essence, it is not possible to produce abradable sound absorbing micro-scaffolds with DIW (for 250 μm filaments) by adding PJ to the benchmark material.

5.2.6 Pullout tests - Star blends

Figure 5.4 (a) shows a representative fracture surface obtained during pullout tests, together with the dolly used for these tests. Figure 5.4 (b) reports the percentage of cohesive coating failure and the pullout strength for different loadings of GM and FS in the neat resin. The percentage of cohesive to adhesive failure appears to be lower on average for the star blends relative to the benchmark, but remains above ∼45%. The 5GM:10FS blend exhibits a predominantly adhesive failure, which is not the case for the 0GM:12FS and 10GM:8FS blends or the benchmark.

Significantly higher pullout strengths were measured for the star blends (6.4 ± 1.8 MPa on average), compared to the baseline benchmark (3.3 ± 0.5 MPa). Although the star blends tend to fail closer to an adhesive fracture mode, they offer a increased pullout strength at the 95% confidence level. A higher mechanical resistance provides evidence for a potentially lower abradability for the developed composites against the benchmark, because more energy must transferred from the blade to the coating for material wear.

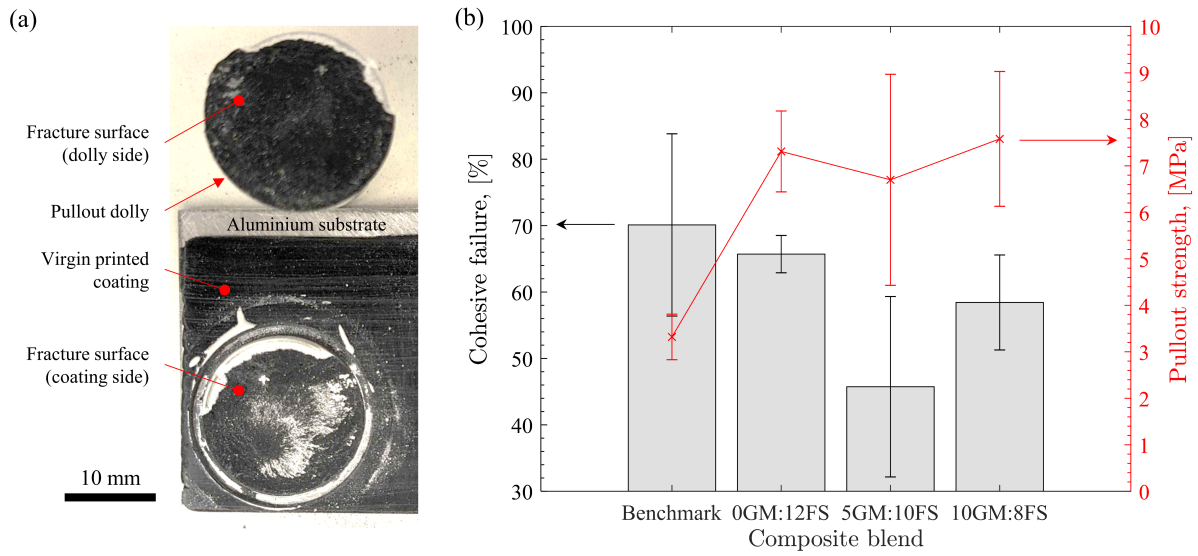

Figure 5.4 (a) Representative fracture surface for adhesion tests, here for the 10GM:8FS blend, printed with a 1.54 mm nozzle on the Aerotech deposition system. (b) Comparison of the cohesive failure percentage and pullout strength of the star blends and the benchmark. Error bars represent the 95% confidence intervals obtained from 4 replications.

5.2.7 Micro-hardness tests - Star blends

Figure 5.5 (a) shows the Shore D hardness of the three star blends compared to the benchmark. The 0GM:12FS blend exhibits the highest hardness among the four materials (75.2 ± 2.1 D), followed by the 5GM:10FS and 10GM:8FS (66.7 ± 2.1 D and 61.0 ± 1.7 D, respectively). The benchmark appears to have the lowest Shore D hardness at 54.4 ± 0.8 D. Figure 5.5 (b) presents the normalised Shore D hardness values for the star blends and the benchmark, relative to the latter. The horizontal lines represent the 95% confidence interval for the normalised experimental hardness values. The 0GM:12FS blend features a Shore D hardness ∼40% higher than the benchmark, compared to ∼25% for the 5GM:10FS and ∼15% for the 10GM:8FS blend. Therefore, the star blends offer a significantly higher Shore D hardness than the benchmark, at the 95% confidence level.

A higher hardness for the star blends supports that they are less abradable than the benchmark. In other words, the amount of GM in the star blends appears to insufficient to generate enough porosity within the bulk material to match the abradability of the highly loaded benchmark (∼22.5 wt.% GM), based on the measured mechanical properties. In addition to abradability, a higher micro-hardness for the star blends also indicates a potentially improved erosion resistance over the benchmark [17]. However, harder materials have the potential to cause localised wear the blade during low speed incursions [55], for example during engine ignition or idling. Further mechanical characterisation is required to draw definite

conclusions, because the aforementioned abradability indicators (pullout strength, cohesive failure percentage and micro-hardness) merely provide a relative comparison between materials. The true abradability must be assessed by more direct means, such as through the progressive abradability hardness [53, 54] for an accurate comparison to the benchmark.

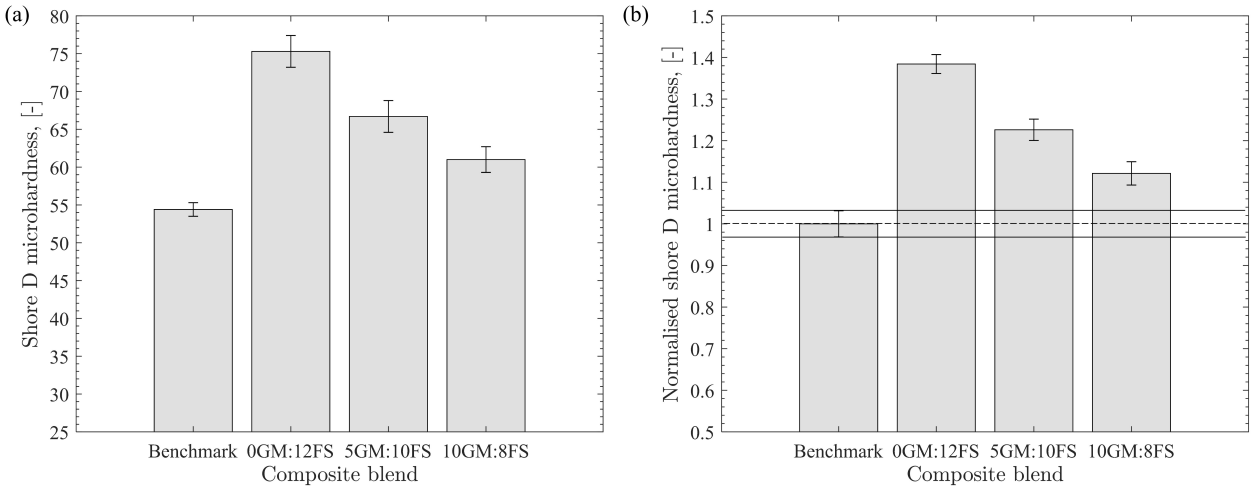

Figure 5.5 Comparison of the (a) Shore D hardness and (b) Normalised Shore D hardness for the star blends and the benchmark. Error bars represent the 95% confidence intervals obtained from 5 replications.

5.2.8 Analysis of the star blends

In Chapter 4, the star blends were printed as sound absorbing micro-scaffolds with DIW using both 250 μm cylindrical or tapered nozzles. Based on rheology measurements, the available time to extrude the star blends prior to gelation in the syringe follows the trend such that 0GM:12FS > 5GM:10FS > 10GM:8FS (i.e., the time after mixing to double the initial viscosity). The pot life is a crucial parameter in determining the feasibility of a large-area print, e.g. for covering a fan case with a sound absorbing coating, considering the quantity of material needed for this operation. It must also be noted that autocatalytic effects (acceleration of cure rate) could result in lowering the pot lives reported in Chapter 4. As printing large-area micro-structures requires mixing a considerable amount of material, the heat generated by the cure might decrease the t^* during industrial-scale production. Nevertheless, the strong shear-thinning behaviour of the star blends paves the way for large-area high-speed printing with the multinozzle system, because these materials act as liquids during extrusion but return to a solid-like paste with filamentary shape once deposited.

The star blends were subjected to mechanical tests to establish a bulk comparison with the commercial abradable material from which their development is drawn. Pullout and micro-hardness tests both point to the same conclusion: the star blends appear to be

less abradable than the benchmark. Lowering the GM content relative to the benchmark and substituting in FS is critical to obtain materials suitable for printing sound absorbing structures. Yet, modifying the fillers and their loading comes at expense of abradability, hinted at by the superior adhesion strength and hardness of the star blends. Hypothetically, the proportion of GM could be slightly increased to improve the abradability of the star blends by using smaller GM.

5.3 Limitations

Kundt's tube micro-scaffolds could not printed at high speeds, corresponding to maximum dispensing pressure, due to limitations of the deposition system. Additional work is needed to better control the acceleration/deceleration movements of the robotic system. The current infrastructure is not able prevent significant material over-extrusion for curved features (e.g., the outer wall of acoustic samples). The infrastructure also did not allow to produce a 25 mm height acoustic sample in one print, because the available material volume was limited to 3 cm^3, against the required $\sim$12cm^3. Moreover, the printed pore size was not completely controllable due to material cure, which required a manual adjustment of the pressure in an attempt to keep a constant extrusion flow rate. The acoustic properties reported herein therefore do not reflect the full potential performance of the star blends. As for the theoretical JCAL model, the acoustic absorption results presented in Chapter 4 are not fully representative of the tested sample, because the model does not account for filament surface roughness, local filament shape loss and stacking misalignment.

The fitness of the transient material model introduced in Chapter 4 was assessed to a limited extent. Instead of probing one time step per blend, a time series for each material would be more appropriate to compare the measured speed – or better, using the experimental flow rate – to the values predicted by the model.

The abradability was not measured directly, but rather gauged with indicators provided by mechanical properties (micro-hardness and pullout strength). The abradable functionality remains to be fully characterised and compared to the benchmark with a direct method such as progressive abradability hardness. The star blends could not be printed with the multinozzle, because of raw material availability issues and delays incurred from COVID-19.

CHAPTER 6 CONCLUSION AND RECOMMENDATIONS

6.1 Summary of works

This work presented the development of lightweight composite materials suitable for depositing abradable sound absorbing micro-structure onto non-planar surfaces by high-speed direct ink writing. The first objective of this work was to develop a thermosetting abradable material compatible with a direct ink writing printing process. Objective **O1** was mostly addressed by adding different loadings of hollow glass microspheres and/or fumed silica to the base resin of a commercial abradable product, which was not printable initially. μCT and SEM observations were used to verify and quantify the geometrical fidelity of the studied blends, defining a new printability index. Using shape retention and filler integrity as design criteria, three suitable blends were thus identified: 0GM:12FS, 5GM:10FS and 10GM:8FS. The three blends could be printed between 110 and 175 $mm.s^{-1}$ and a pressure of 4.54 MPa employing a single 250 μm tapered nozzle dispensing system. These printing speeds were also accurately predicted by combining oscillatory, rotational and capillary rheology data into a single governing flow behaviour model for the star blends, including the time after mixing as a modelling variable.

To complement the work associated with objective **O1**, petroleum jelly was also added to the commercial product in different weight loadings to allow post-printing shape retention. Two loadings were determined as optimal process-wise, i.e. 7.5 wt.% PJ for 250 μm tapered nozzles and 12.5 wt.% for 250 μm cylindrical nozzles. Although the addition of PJ below 15 wt.% did seem to affect the bulk hardness or pullout strength of the benchmark, GM crushing and the cohesive failure percentage for printable formulations were deemed incompatible with the desired abradable functionality. Therefore, directly functionalising the benchmark was not a viable solution.

The second objective of this work was to evaluate the bulk mechanical properties of the new material and assess the predictability of acoustic properties for printed structures. Therefore, building upon the results of **O1**, sound absorption properties were characterised using a Kundt's tube to address part of **O2**. Micro-scaffold printed with the star blends demonstrated the potential of the composite materials developed in this work for noise reduction applications. Sound absorption coefficients above 0.6 were achieved in the tested frequency range ($500 - 6000$ Hz). The damping ratios and sound absorption coefficients of printed micro-scaffolds could be predicted with the JCAL acoustic model for the targeted geometrical parameters. The discrepancies observed between simulated and measured acoustic performances were ascribed to human intervention during the printing process (i.e., adjusting

the extrusion pressure to compensate for cure effects, which affects pore size, stacking height and porosity), and filament surface roughness unaccounted for in the JCAL model.

To verify the abradable functionality of the star blends, in line with **O2**, Shore D micro-hardness and pullout (adhesion) tests were also carried out. Considering the properties obtained from these preliminary mechanical tests, the 10GM:8FS blend appears to be the composite material best-suited among the star blends for producing abradable micro-scaffolds. Unlike the benchmark, the 10GM:8FS blend is printable, and has a longer working time. However, the 10GM:8FS blend is ∼15% harder and has a pullout strength twice that of the benchmark, which could result in a reduced abradability compared to the the benchmark. More direct mechanical characterisations are needed to validate this conclusion.

6.2 Future research

Regarding the aforementioned limitations, the following steps should be considered critical in selecting the star blend that satisfies best the targeted application:

1. Measure flexural and tensile properties to help establish additional indicators for abradability. Mechanical properties will be useful if modelling or simulation works are undertaken in the future, e.g. to predict the vibration modes of blade-to-coating interactions.

2. Carry out micro-indentation (scratch tests) to compute the progressive abradability hardness, which can be used for quantifying abradability.

3. Repeat DSC and TGA sweeps as well as scratch and pullout test for pre and post hygrothermal ageing to assess the effects of environmental degradation.

4. Conduct abradability tests on micro-scaffolds and coatings using a specialised test bench to evaluate the performance of the star blends compared to be benchmark. Likewise, impact and erosion tests should be considered to evaluate the damage induced by rain, hail, or ice becoming detached from the fan. These tests should also be carried out on pre and post hygrothermally aged samples with the desired acoustic geometry.

5. Investigate the effects on sound absorption of abraded particles and fluid retained within the micro-scaffolds pore for structures printed with the star blends.

6. Reduce the mean GM diameter by sieving. The potential positive effects are three-fold: (1) filtering out larger GM for a diameter $\leq$50 µm should further reduce the occurrence of nozzle clogging, (2) finer nozzles could be tested (e.g. $D_o = \{200, 185\}$ µm) to obtain thinner filament which would allow for absorbing lower frequency sound waves, and (3) increase the GM volume content for improved abradability.

7. Scale up the single nozzle production of samples by transferring the work done for the star blends to a multinozzle system. The star blends should also be printed on non-planar composite surfaces to confirm that printing on a fan case is feasible.

8. Perform a parametric study to verify the versatility of the star blends for printing other geometries, e.g. micro-channels and graded porous structures (wherein pore sizes vary through the thickness). Such structures can be tailored to capture a larger bandwidth of sound waves than simple micro-scaffolds, in the frequency range representative of turbofan noise emissions.

6.3 Project outcomes and significance

The research methodology outlined herein enabled the formulation of lightweight 3D-printable thermoset composite materials. This same methodology can be applied for the development of multifunctional composite materials for DIW in other industries, beyond aerospace applications, such as in the marine or ground transportation sectors. Large-scale structures may be printed with the star blends, perhaps even with additional functionalities currently explored in the literature. For instance, a future multi-material process could integrate conductive inks into the networks printed star blends to produce smart structures capable of monitoring the wear of porous abradable coatings. Alternatively, to reduce maintenance down times and ensure an optimal aerodynamic performance of abradable seals, self-healing elements could also be included in the star blends so to regrow excessively worn out coating sections.

The multifunctional composite materials developed in this work will ultimately help reducing the consumption of polluting fossil fuels in commercial aviation. The reduction of anthropogenic CO_2 emissions, which accelerate the global rise in temperatures and sea levels, is paramount to secure a liveable environment for future generations. The massive release of nitrogen oxides (NO_x) and black carbon by commercial aviation exacerbates climate change through an increased concentration of green house gasses in the atmosphere, and leads to the formation of toxic aerosols that degrade the air quality worldwide. Optimising aircraft fuel consumption will help in the short term to mitigate these harmful environmental effects of air travel, until reliable *green* alternatives are scaled up for passenger aircraft, be it with disruptive technologies like completely electrical engines or with hydrogen gas propulsion. The developed composite materials will also contribute to further reduce aircraft engine noise to provide a quieter and safer environment for communities living around airports, as noise can disturb sleep patterns, impact the academic performance of children, and adversely affect psychological and physical health in those communities.

REFERENCES

[1] International Civil Aviation Organization, "ICAO ENVIRONMENTAL REPORT 2016: AVIATION AND CLIMATE CHANGE," Environment Branch of the International Civil Aviation, Montréal, Canada, Tech. Rep., jul 2016. [Online]. Available: https://www.icao.int/environmental-protection/documents/ICAOEnvironmentalReport2016.pdf

[2] Directorate-General for Research and Innovation, "Flightpath 2050 Europe's Vision for Aviation Report of the High-Level Group on Aviation Research," EUROPEAN COMMISSION, Brussels, Belgium, Tech. Rep., 2011. [Online]. Available: https://ec.europa.eu/transport/sites/default/files/modes/air/doc/flightpath2050.pdf

[3] A. Dubourg-Cassagne, "Intégration de structures absorbantes acoustiques innovantes au sein d'une turbosoufflante," Ph.D. dissertation, Polytechnique Montréal, Montréal, Canada, 2015.

[4] P. Dowson, M. S. Walker, and A. P. Watson, "Development of abradable and rub-tolerant seal materials for application in centrifugal compressors and steam turbines," *Sealing Technology*, vol. 2004, no. 12, pp. 5–10, apr 2004. [Online]. Available: https://linkinghub.elsevier.com/retrieve/pii/S1350478904004519http://files/219/Dowsonetal.-2004-Developmentofabradableandrub-tolerantsealmat.pdf

[5] B. Berthoul, A. Batailly, L. Stainier, M. Legrand, and P. Cartraud, "Phenomenological modeling of abradable wear in turbomachines," *Mechanical Systems and Signal Processing*, vol. 98, pp. 770–785, jan 2018. [Online]. Available: https://linkinghub.elsevier.com/retrieve/pii/S0888327017302753

[6] Y. Kang, W. Lee, J. Hwang, and Y. Lee, "Influence of Glass Microsphere Filler on the Rheological Behavior of an Epoxy Resin," *International Polymer Processing*, vol. 33, no. 2, pp. 146–152, jun 2018. [Online]. Available: http://www.hanser-elibrary.com/doi/10.3139/217.3338http://files/295/Kangetal.-2018-InfluenceofGlassMicrosphereFillerontheRheol.pdf

[7] D. W. Bill, R. C.;Wisander, "Friction and wear of several compressor gas-path seal movements," NASA, Cleveland, OH, Tech. Rep., 1978. [Online]. Available: https://ntrs.nasa.gov/citations/19780007286

[8] R. Mathon, R. Jaussaud, and D. M. Serge, "Device for applying abradable material to a surface of a turbine engine casing," 2019. [Online]. Available: http://files/164/Mathonetal.-2019-Deviceforapplyingabradablematerialtoasurfac.pdf

[9] I. GIbson, D. W. Rosen, and B. Stucker, "Introduction and Basic Principles," in *Additive Manufacturing Technologies: Rapid Prototyping to Direct Digital Manufacturing*. New York (NY), USA: Springer, 2010, pp. 1–16.

[10] S. A. Morrison, C. Winston, and T. Watson, "Fundamental Flaws of Social Regulation: The Case of Airplane Noise," *Journal of Law and Economics*, vol. 42, no. 2, pp. 723–743, jul 1999. [Online]. Available: https://ideas.repec.org/a/ucp/jlawec/v42y1999i2p723-43.html

[11] Y. Li, X. Wang, and D. Zhang, "Control strategies for aircraft airframe noise reduction," *Chinese Journal of Aeronautics*, vol. 26, no. 2, pp. 249–260, 2013. [Online]. Available: http://dx.doi.org/10.1016/j.cja.2013.02.001

[12] S. Martens, "JET NOISE REDUCTION TECHNOLOGY DEVELOPMENT AT GE AIRCRAFT ENGINES," in *23rd Congress of International Council of the Aeronautical Sciences*, vol. 8, jul 2002, p. 10. [Online]. Available: https://www.icas.org/ICAS{_}ARCHIVE/ICAS2002/ABSTRACTS/842.HTMhttp://files/369/Martens-JETNOISEREDUCTIONTECHNOLOGYDEVELOPMENTATGEA.pdf

[13] D. Wimpenny, I. Pandey, P. M. Kumar, and L. Jyothish, *A review on status of research in metal additive manufacturing*. Singapore: Springer Science, 2017. [Online]. Available: https://www.springer.com/gp/book/9789811008115{#}aboutAuthors

[14] M. Kamal and G. Rizza, "4 - Design for metal additive manufacturing for aerospace applications," in *Additive Manufacturing for the Aerospace Industry*, F. Froes and R. Boyer, Eds. Elsevier, jul 2019, pp. 67–86. [Online]. Available: http://www.sciencedirect.com/science/article/pii/B9780128140628000054

[15] S. Singamneni, Y. LV, A. Hewitt, R. Chalk, W. Thomas, and D. Jordison, "Additive Manufacturing for the Aircraft Industry: A Review," *Journal of Aeronautics & Aerospace Engineering*, vol. 08, no. 01, 2019.

[16] E. Brothers, "Stratasys to 3D print Airbus A350 XWB parts," *Aerospace Manufacturing and Design*, pp. 1–5, oct 2017. [Online]. Available: https://www.aerospacemanufacturinganddesign.com/article/stratasys-to-3d-print-airbus-a350-xwb-parts/

[17] S. Wilson, "Thermally sprayed abradable coating technology for sealing in gas turbines," in *Future of gas turbine technology, 6th International Conference*, Brussels, Belgium, 2012, pp. 1–9. [Online]. Available: https://api.semanticscholar.org/CorpusID:102502114

[18] T. Jorquera, J.-P. George, M.-P. Gleizes, and C. Regis, "A Natural Formalism and a Multi-agent Algorithm for Integrative Multidisciplinary Design Optimization," in *2013 IEEE/WIC/ACM International Joint Conferences on Web Intelligence (WI) and Intelligent Agent Technologies (IAT)*, vol. 2, no. November. IEEE, nov 2013, pp. 146–154. [Online]. Available: http://ieeexplore.ieee.org/document/6690783/

[19] CFM International SA, "The LEAP engine overview," CFM, Cinicinnati, OH, Tech. Rep., 2017. [Online]. Available: https://www.cfmaeroengines.com/wp-content/uploads/2017/09/Brochure{_}LEAPfiches{_}2017.pdf

[20] Federal Aviation Administration, "Transition to Turbopropeller-Powered Airplanes," in *Airplane Flying Handbook FAA (Federal Aviation Administration)-H-8083-3B*. Washington, D.C.: U.S. Department of Transportation, 2016, ch. Transition, pp. 1–31. [Online]. Available: https://www.faa.gov/regulations{_}policies/handbooks{_}manuals/aviation/airplane{_}handbook/

[21] Y. A. Cengel and M. A. Boles, "Thermodynamics: an Engineering Approach 8th Edition," in *McGraw-Hill*, 2015, pp. 524–526.

[22] R. T. Sataloff, M. M. Johns, and K. M. Kost, "Continued development of abradable gas path seals," Pratt&Whitey Aircraft, Cleveland, OH, Tech. Rep., 1975. [Online]. Available: https://ntrs.nasa.gov/citations/19760004187

[23] S. Skiba, L. Faure, S. Philippon, and J. Papasidero, "Experimental Investigation of the Mechanical Behavior of an AlSi-PE Abradable Coating at High Strain Rates for a Large Range of Temperatures," *Journal of Dynamic Behavior of Materials*, vol. 6, no. 2, pp. 213–223, jun 2020. [Online]. Available: https://doi.org/10.1007/s40870-020-00242-yhttp://link.springer.com/10.1007/s40870-020-00242-y

[24] M. Borel, A. Nicoll, H. Schlapfer, and R. Schmid, "The wear mechanisms occurring in abradable seals of gas turbines," *Surface and Coatings Technology*, vol. 39-40, no. C, pp. 117–126, dec 1989. [Online]. Available: https://linkinghub.elsevier.com/retrieve/pii/0257897289900467

[25] S. Baïz, "Etude expérimentale du contact aube/abradable : Contribution à la caractérisation mécanique des matériaux abradables et de leur interaction dynamique sur banc rotatif avec une aube," Ph.D. dissertation, Ecole Centrale de Lille, 2011. [Online]. Available: https://tel.archives-ouvertes.fr/tel-00605091

[26] R. E. Chupp, R. C. Hendricks, S. B. Lattime, and B. M. Steinetz, "Sealing in turbomachinery," NASA, Cleveland, OH, Tech. Rep., 2006. [Online]. Available: https://ntrs.nasa.gov/api/citations/20060051674/downloads/20060051674.pdf

[27] M. Legrand, A. Batailly, and C. Pierre, "Numerical Investigation of Abradable Coating Removal in Aircraft Engines Through Plastic Constitutive Law," *Journal of Computational and Nonlinear Dynamics*, vol. 7, no. 1, jan 2012. [Online]. Available: https://asmedigitalcollection.asme.org/computationalnonlinear/article/doi/10.1115/1.4004951/465827/Numerical-Investigation-of-Abradable-Coating

[28] A. Vardelle, C. Moreau, J. Akedo, H. Ashrafizadeh, C. C. Berndt, J. O. Berghaus, M. Boulos, J. Brogan, A. C. Bourtsalas, A. Dolatabadi, M. Dorfman, T. J. Eden, P. Fauchais, G. Fisher, F. Gaertner, M. Gindrat, R. Henne, M. Hyland, E. Irissou, E. H. Jordan, K. A. Khor, A. Killinger, Y.-C. Lau, C.-J. Li, L. Li, J. Longtin, N. Markocsan, P. J. Masset, J. Matejicek, G. Mauer, A. McDonald, J. Mostaghimi, S. Sampath, G. Schiller, K. Shinoda, M. F. Smith, A. A. Syed, N. J. Themelis, F.-L. Toma, J. P. Trelles, R. Vassen, and P. Vuoristo, "The 2016 Thermal Spray Roadmap," *Journal of Thermal Spray Technology*, vol. 25, no. 8, pp. 1376–1440, dec 2016. [Online]. Available: http://link.springer.com/10.1007/s11666-016-0473-x

[29] R. Hendricks, B. M. Steinetz, and M. J. Braun, "Turbomachine Sealing and Secondary Flows Part 1—Review of Sealing Performance, Customer, Engine Designer, and Research Issues," NASA, Cleveland, OH, Tech. Rep. July, 2004. [Online]. Available: https://ntrs.nasa.gov/api/citations/20040086704/downloads/20040086704.pdf

[30] S. Lattime and B. Steinetz, "Turbine Engine Clearance Control Systems: Current Practices and Future Directions," in *38th AIAA/ASME/SAE/ASEE Joint Propulsion Conference & Exhibit*, no. July. Reston, Virigina: American Institute of Aeronautics and Astronautics, jul 2002. [Online]. Available: http://arc.aiaa.org/doi/abs/10.2514/6.2002-3790

[31] Oerlikon Metco, "Solutions Flash: Corrosion-Resistant Compressor Abradable Reduces Maintenance and Operating Costs The Oerlikon Metco solution," Oerlikon Metco, Tech. Rep. September, 2019. [Online].

Available: https://www.oerlikon.com/ecomaXL/files/metco/oerlikon{_}SF-0028.0{_}Corrosion-Resistant{_}LPC{_}Abradable.pdf{&}download=1

[32] J. Liu, Y. Yu, T. Liu, X. Cheng, J. Shen, and C. Li, "The Influence of Composition and Microstructure on the Abradability of Aluminum-Based Abradable Coatings," *Journal of Thermal Spray Technology*, vol. 26, no. 6, pp. 1095–1103, aug 2017. [Online]. Available: http://files/165/Liuetal.-2017-TheInfluenceofCompositionandMicrostructureon.pdfhttp://link.springer.com/10.1007/s11666-017-0526-9

[33] D. Aussavy, R. Bolot, G. Montavon, F. Peyraut, G. Szyndelman, J. Gurt-Santanach, and S. Selezneff, "YSZ-Polyester Abradable Coatings Manufactured by APS," *Journal of Thermal Spray Technology*, vol. 25, no. 1-2, pp. 252–263, jan 2016. [Online]. Available: http://link.springer.com/10.1007/s11666-015-0358-4

[34] E. Scrinzi, I. Giovannetti, N. Sheng, and L. Leblanc, "Development of New Abradable/Abrasive Sealing Systems for Clearance Control in Gas Turbines," in *ASME 2013 Turbine Blade Tip Symposium*. Hamburg, Germany: American Society of Mechanical Engineers, sep 2013, pp. 1–10. [Online]. Available: https://asmedigitalcollection.asme.org/TBTS/proceedings/TBTS2013/56079/Hamburg,Germany/285505

[35] U. Bardi, C. Giolli, A. Scrivani, G. Rizzi, F. Borgioli, A. Fossati, K. Partes, T. Seefeld, D. Sporer, and A. Refke, "Development and Investigation on New Composite and Ceramic Coatings as Possible Abradable Seals," *Journal of Thermal Spray Technology*, vol. 17, no. 5-6, pp. 805–811, dec 2008. [Online]. Available: http://link.springer.com/10.1007/s11666-008-9246-5

[36] G. D. P. Daniel P. Rose and Alexander Bosna, "DEVELOPMENT OF A NONMETALLIC ABRADABLE MATERIAL SYSTEM FOR GAS TURBINE APPLICATIONS," in *International Gas Turbine and Aeroengine Congress and Exposition*. ASME, 1993.

[37] Y. Q. Tong, Q. S. Shi, M. J. Liu, G. R. Li, C. J. Li, and G. J. Yang, "Lightweight epoxy-based abradable seal coating with high bonding strength," *Journal of Materials Science and Technology*, vol. 69, pp. 129–137, 2021. [Online]. Available: https://doi.org/10.1016/j.jmst.2020.05.077

[38] N. Merriman, "ABRADABLE LINER FOR A GAS TURBINE," 2013. [Online]. Available: https://patentimages.storage.googleapis.com/6a/c0/6e/4e0f90fd519cfa/WO2013075954A1.pdf

[39] Edward F Lapac and Byron H Shinn, "Composite abradable seal," 1969. [Online]. Available: https://patentimages.storage.googleapis.com/94/ec/a8/37738b96b8208a/US3575427.pdf

[40] A. A. Bosna, "ABRADABLE NON-METALLIC SEAL FOR ROTATING TURBINE ENGINES," 1994. [Online]. Available: https://patents.google.com/patent/US5304032A/en

[41] 3M, "3M Scotch-Weld Structural Void Filling Compound EC-3524 B/A," 2020. [Online]. Available: https://www.3m.com/3M/en{_}US/company-us/all-3m-products/{~}/3M-Scotch-Weld-Structural-Void-Filling-Compound-EC-3524-B-A/?N=5002385+3292668520{&}rt=rud

[42] John W. Putnam and Charles R. Watson, "Turbine friendly abradable material," 2011. [Online]. Available: https://patentimages.storage.googleapis.com/5a/5e/64/eef8ac562a4c1f/US20070197719A1.pdf

[43] P. Biez, "TURBINE ENGINE STATOR WALL COVERED IN AN ABRADABLE COATING," 2011. [Online]. Available: https://patentimages.storage.googleapis.com/ec/a8/bd/ea209195392547/FR2979664A1.pdf

[44] M. Yi, J. He, B. Huang, and H. Zhou, "Friction and wear behaviour and abradability of abradable seal coating," *Wear*, vol. 231, no. 1, pp. 47–53, jun 1999. [Online]. Available: https://linkinghub.elsevier.com/retrieve/pii/S0043164899000939

[45] R. E. Chupp, F. Ghasripoor, N. A. Turnquist, M. Demiroglu, and M. F. Aksit, "Advanced Seals for Industrial Turbine Applications: Dynamic Seal Development," *Journal of Propulsion and Power*, vol. 18, no. 6, pp. 1260–1266, nov 2002. [Online]. Available: https://arc.aiaa.org/doi/10.2514/2.6061

[46] R. E. Johnston, "The Sensitivity of Abradable Coating Residual Stresses to Varying Material Properties," *Journal of Thermal Spray Technology*, vol. 18, no. 5-6, pp. 1004–1013, dec 2009. [Online]. Available: http://link.springer.com/10.1007/s11666-009-9378-2

[47] B. Berthoul, "Prise en compte du comportement des materiaux abradables dans la modelisation de l'interaction aube/carter." Ph.D. dissertation, Universit´e Nantes Angers Le Mans, 2016. [Online]. Available: https://hal.archives-ouvertes.fr/tel-01390192

[48] F. Ghasripoor, R. Schmid, and M. Dorfman, "Abradables improve gas turbine efficiency," *Materials World*, 1997.

[49] Sulzer Metco, "An Introduction to Thermal Spray," Oerlikon, Tech. Rep. 6, 2013. [Online]. Available: https://www.oerlikon.com/metco/en/products-services/coating-equipment/thermal-spray/processes/controlled-atmospheric-plasma/

[50] D. Kumar, "Optimization of spray parameters for high-velocity oxy-fuel spraying (HVOF) sprayed abradable coating," Master's Thesis, Thapar University, 2014. [Online]. Available: http://tudr.thapar.edu:8080/jspui/bitstream/10266/2773/4/2773.pdf

[51] S. Kuroda, J. Kawakita, M. Watanabe, and H. Katanoda, "Warm spraying—a novel coating process based on high-velocity impact of solid particles," *Science and Technology of Advanced Materials*, vol. 9, no. 3, p. 033002, jul 2008. [Online]. Available: http://www.tandfonline.com/doi/full/10.1088/1468-6996/9/3/033002

[52] J. M. Forrester, B. R. Love, J. W. Baldwin, and W. Chester, "Seal including a non-metallic abradable material," 1995. [Online]. Available: https://patents.google.com/patent/US5388959A/en

[53] X. Ma and A. Matthews, "Investigation of abradable seal coating performance using scratch testing," *Surface and Coatings Technology*, vol. 202, no. 4-7, pp. 1214–1220, dec 2007. [Online]. Available: https://linkinghub.elsevier.com/retrieve/pii/S0257897207007992

[54] X. Ma and A. Matthews, "Evaluation of abradable seal coating mechanical properties," *Wear*, vol. 267, no. 9-10, pp. 1501–1510, sep 2009. [Online]. Available: https://linkinghub.elsevier.com/retrieve/pii/S004316480900283X

[55] N. Fois, M. Watson, and M. Marshall, "The influence of material properties on the wear of abradable materials," *Proceedings of the Institution of Mechanical Engineers, Part J: Journal of Engineering Tribology*, vol. 231, no. 2, pp. 240–253, apr 2017. [Online]. Available: http://journals.sagepub.com/doi/10.1177/1350650116649528

[56] L. Y. Zhou, Q. Gao, J. Z. Fu, Q. Y. Chen, J. P. Zhu, Y. Sun, and Y. He, "Multimaterial 3D Printing of Highly Stretchable Silicone Elastomers," *ACS Applied Materials and Interfaces*, vol. 11, no. 26, pp. 23 573–23 583, 2019.

[57] A. Dadouche, M. J. Conlon, W. Dmochowski, B. Liko, and J.-P. Bedard, "Experimental Evaluation of Abradable Seal Performance at High Temperature," in

Volume 5: Structures and Dynamics, Parts A and B. ASMEDC, jan 2008, pp. 143–150. [Online]. Available: https://asmedigitalcollection.asme.org/GT/proceedings/GT2008/43154/143/324605

[58] European Aviation Safety Agency, "TYPE-CERTIFICATE DATA SHEET for Engine LEAP-1A & LEAP-1C series engines," CFM International SA CFM, Brussels, Belgium, Tech. Rep. March, 2016. [Online]. Available: https://www.easa.europa.eu/document-library/type-certificates/engine-cs-e/easae110

[59] X. Kuang, Z. Zhao, K. Chen, D. Fang, G. Kang, and H. J. Qi, "High-Speed 3D Printing of High-Performance Thermosetting Polymers via Two-Stage Curing," *Macromolecular Rapid Communications*, vol. 39, no. 7, p. 1700809, apr 2018. [Online]. Available: http://doi.wiley.com/10.1002/marc.201700809

[60] N. Nawafleh and E. Celik, "Additive manufacturing of short fiber reinforced thermoset composites with unprecedented mechanical performance," *Additive Manufacturing*, vol. 33, no. February, p. 101109, 2020. [Online]. Available: https://doi.org/10.1016/j.addma.2020.101109

[61] M. Rafiee, R. D. Farahani, and D. Therriault, "Multi-Material 3D and 4D Printing: A Survey," *Advanced Science*, vol. 7, no. 12, pp. 1–26, 2020.

[62] E. R. Fotsing, A. Dubourg, A. Ross, and J. Mardjono, "Acoustic properties of periodic micro-structures obtained by additive manufacturing," *Applied Acoustics*, vol. 148, pp. 322–331, may 2019. [Online]. Available: https://doi.org/10.1016/j.apacoust.2018.12.030https://linkinghub.elsevier.com/retrieve/pii/S0003682X18307357

[63] R. Dermanaki Farahani and M. Dubé, "Printing Polymer Nanocomposites and Composites in Three Dimensions," *Advanced Engineering Materials*, vol. 20, no. 2, p. 1700539, feb 2018. [Online]. Available: http://doi.wiley.com/10.1002/adem.201700539

[64] D. Lei, Y. Yang, Z. Liu, S. Chen, B. Song, A. Shen, B. Yang, S. Li, Z. Yuan, Q. Qi, L. Sun, Y. Guo, H. Zuo, S. Huang, Q. Yang, X. Mo, C. He, B. Zhu, E. M. Jeffries, F.-L. Qing, X. Ye, Q. Zhao, and Z. You, "A general strategy of 3D printing thermosets for diverse applications," *Materials Horizons*, vol. 6, no. 2, pp. 394–404, 2019. [Online]. Available: http://xlink.rsc.org/?DOI=C8MH00937F

[65] L. L. Lebel, B. Aissa, M. A. E. Khakani, and D. Therriault, "Ultraviolet-Assisted Direct-Write Fabrication of Carbon Nanotube/Polymer Nanocomposite Microcoils,"

Advanced Materials, vol. 22, no. 5, pp. 592–596, feb 2010. [Online]. Available: http://doi.wiley.com/10.1002/adma.200902192

[66] M. G. Odom, C. B. Sweeney, D. Parviz, L. P. Sill, M. A. Saed, and M. J. Green, "Rapid curing and additive manufacturing of thermoset systems using scanning microwave heating of carbon nanotube/epoxy composites," *Carbon*, vol. 120, pp. 447–453, aug 2017. [Online]. Available: https://linkinghub.elsevier.com/retrieve/pii/S0008622317305225http://files/378/Odometal.-2017-Rapidcuringandadditivemanufacturingofthermos.pdf

[67] B. Wang, Z. Zhang, Z. Pei, J. Qiu, and S. Wang, "Current progress on the 3D printing of thermosets," *Advanced Composites and Hybrid Materials*, vol. 3, no. 4, pp. 462–472, dec 2020. [Online]. Available: http://link.springer.com/10.1007/s42114-020-00183-z

[68] B. G. Compton and J. A. Lewis, "3D-Printing of Lightweight Cellular Composites," *Advanced Materials*, vol. 26, no. 34, pp. 5930–5935, sep 2014. [Online]. Available: http://doi.wiley.com/10.1002/adma.201401804

[69] R. S. Jordan and Y. Wang, "3D printing of conjugated polymers," *Journal of Polymer Science Part B: Polymer Physics*, vol. 57, no. 23, pp. 1592–1605, dec 2019. [Online]. Available: https://onlinelibrary.wiley.com/doi/abs/10.1002/polb.24893

[70] J. Sun, W. Zhou, L. Yan, D. Huang, and L.-y. Lin, "Extrusion-based food printing for digitalized food design and nutrition control," *Journal of Food Engineering*, vol. 220, pp. 1–11, mar 2018. [Online]. Available: https://doi.org/10.1016/j.jfoodeng.2017.02.028https://linkinghub.elsevier.com/retrieve/pii/S0260877417300730

[71] R. D. Farahani, K. Chizari, and D. Therriault, "Three-dimensional printing of freeform helical microstructures: a review," *Nanoscale*, vol. 6, no. 18, p. 10470, jun 2014. [Online]. Available: http://xlink.rsc.org/?DOI=C4NR02041C

[72] L. Friedrich, R. Collino, T. Ray, and M. Begley, "Acoustic control of microstructures during direct ink writing of two-phase materials," *Sensors and Actuators, A: Physical*, vol. 268, pp. 213–221, 2017. [Online]. Available: https://doi.org/10.1016/j.sna.2017.06.016

[73] J. P. Lewicki, J. N. Rodriguez, C. Zhu, M. A. Worsley, A. S. Wu, Y. Kanarska, J. D. Horn, E. B. Duoss, J. M. Ortega, W. Elmer, R. Hensleigh, R. A. Fellini, and M. J. King, "3D-Printing of Meso-structurally Ordered Carbon Fiber/Polymer Composites

with Unprecedented Orthotropic Physical Properties," *Scientific Reports*, vol. 7, no. 1, p. 43401, mar 2017. [Online]. Available: http://www.nature.com/articles/srep43401

[74] K. Chen, X. Kuang, V. Li, G. Kang, and H. J. Qi, "Fabrication of tough epoxy with shape memory effects by UV-assisted direct-ink write printing," *Soft Matter*, vol. 14, no. 10, pp. 1879–1886, 2018.

[75] S. Chandrasekaran, E. B. Duoss, M. A. Worsley, and J. P. Lewicki, "3D printing of high performance cyanate ester thermoset polymers," *Journal of Materials Chemistry A*, vol. 6, no. 3, pp. 853–858, 2018.

[76] N. S. Hmeidat, J. W. Kemp, and B. G. Compton, "High-strength epoxy nanocomposites for 3D printing," *Composites Science and Technology*, vol. 160, pp. 9–20, 2018. [Online]. Available: https://doi.org/10.1016/j.compscitech.2018.03.008

[77] H. A. Pierson, E. Celik, A. Abbott, H. De Jarnette, L. Sierra Gutierrez, K. Johnson, H. Koerner, and J. W. Baur, "Mechanical Properties of Printed Epoxy-Carbon Fiber Composites," *Experimental Mechanics*, vol. 59, no. 6, pp. 843–857, 2019.

[78] N. Nawafleh, F. K. E. Elibol, M. Aljaghtham, E. Oflaz, A. J. Ciciriello, C. M. Dumont, E. Dauer, R. M. Gorguluarslan, T. Demir, and E. Celik, "Static and dynamic mechanical performance of short Kevlar fiber reinforced composites fabricated via direct ink writing," *Journal of Materials Science*, vol. 55, no. 25, pp. 11 284–11 295, sep 2020. [Online]. Available: https://doi.org/10.1007/s10853-020-04826-w

[79] N. Nawafleh, W. Wright, N. Dariavach, and E. Celik, "3D-printed thermoset syntactic foams with tailorable mechanical performance," *Journal of Materials Science*, vol. 55, no. 33, pp. 16 048–16 057, 2020. [Online]. Available: https://doi.org/10.1007/s10853-020-05111-6

[80] Y. Guo, Y. Liu, J. Liu, J. Zhao, H. Zhang, and Z. Zhang, "Shape memory epoxy composites with high mechanical performance manufactured by multi-material direct ink writing," *Composites Part A: Applied Science and Manufacturing*, vol. 135, no. April, p. 105903, aug 2020. [Online]. Available: https://doi.org/10.1016/j.compositesa.2020.105903

[81] R. C. Pack, S. K. Romberg, A. A. Badran, N. S. Hmeidat, T. Yount, and B. G. Compton, "Carbon Fiber and Syntactic Foam Hybrid Materials via Core–Shell Material Extrusion Additive Manufacturing," *Advanced Materials Technologies*, vol. 5, no. 12, pp. 1–8, 2020.

[82] B. G. Compton, J. K. Wilt, J. W. Kemp, N. S. Hmeidat, S. R. Maness, M. Edmond, S. Wilcenski, and J. Taylor, "Mechanical and thermal properties of 3D-printed epoxy composites reinforced with boron nitride nanobarbs," *MRS Communications*, vol. XX, no. xx, pp. 1–6, jan 2021. [Online]. Available: https://doi.org/10.1557/s43579-020-00005-9

[83] X. He, Y. Ding, Z. Lei, S. Welch, W. Zhang, M. Dunn, and K. Yu, "3D printing of continuous fiber-reinforced thermoset composites," *Additive Manufacturing*, vol. 40, no. November 2020, p. 101921, apr 2021. [Online]. Available: https://linkinghub.elsevier.com/retrieve/pii/S2214860421000865

[84] F. A. Morrison, "No Memory: Generalized Newtonian Fluids," in *Understanding rheology*, 5th ed. New York: Oxford University Press, 2001, pp. 225–256.

[85] K. Reinhardt, N. Hofmann, and M. Eberstein, "The importance of shear thinning, thixotropic and viscoelastic properties of thick film pastes to predict effects on printing performance," *EMPC 2017 - 21st European Microelectronics and Packaging Conference and Exhibition*, vol. 2018-Janua, no. September, pp. 1–7, 2018.

[86] A. M'Barki, L. Bocquet, and A. Stevenson, "Linking Rheology and Printability for Dense and Strong Ceramics by Direct Ink Writing," *Scientific Reports*, vol. 7, no. 1, p. 6017, dec 2017. [Online]. Available: http://www.nature.com/articles/s41598-017-06115-0

[87] N. W. Solís Pinargote, A. Smirnov, N. Peretyagin, A. Seleznev, and P. Peretyagin, "Direct Ink Writing Technology (3D Printing) of Graphene-Based Ceramic Nanocomposites: A Review," *Nanomaterials*, vol. 10, no. 7, p. 1300, jul 2020. [Online]. Available: https://www.mdpi.com/2079-4991/10/7/1300

[88] Q.-H. Nguyen and N.-D. Nguye, "Incompressible Non-Newtonian Fluid Flows," in *Continuum Mechanics - Progress in Fundamentals and Engineering Applications*, 1st ed. Shanghai: InTech, mar 2012, pp. 47–72. [Online]. Available: http://www.intechopen.com/books/continuum-mechanics-progress-in-fundamentals-and-engineering-applications/non-newtonian-fluid-flows

[89] E. Baur, T. A. Osswald, and N. Rudolph, "Plastics Handbook," in *Plastics Handbook*. München: Carl Hanser Verlag GmbH & Co. KG, jan 2019, ch. Mechanical, pp. 69–89. [Online]. Available: https://www.hanser-elibrary.com/doi/10.3139/9781569905609.fm

[90] A. W. Sisko, "The Flow of Lubricating Greases," *Industrial & Engineering Chemistry*, vol. 50, no. 12, pp. 1789–1792, apr 1958. [Online]. Available: https://doi.org/10.1021/ie50588a042http://files/176/Sisko-1958-TheFlowofLubricatingGreases.pdf

[91] M. T. Gallagher, R. A. J. Wain, S. Dari, J. P. Whitty, and D. J. Smith, "Non-identifiability of parameters for a class of shear-thinning rheological models, with implications for haematological fluid dynamics," *Journal of Biomechanics*, vol. 85, pp. 230–238, apr 2019. [Online]. Available: http://www.sciencedirect.com/science/article/pii/S0021929019300739

[92] C.-H. Jeon and B. R. Hodges, "Comparing thixotropic and Herschel–Bulkley parameterizations for continuum models of avalanches and subaqueous debris flows," *Natural Hazards and Earth System Sciences*, vol. 18, no. 1, pp. 303–319, jan 2018. [Online]. Available: https://nhess.copernicus.org/articles/18/303/2018/

[93] Z. Zhang, Y. Jin, J. Yin, C. Xu, R. Xiong, K. Christensen, B. R. Ringeisen, D. B. Chrisey, and Y. Huang, "Evaluation of bioink printability for bioprinting applications," *Applied Physics Reviews*, vol. 5, no. 4, 2018. [Online]. Available: http://dx.doi.org/10.1063/1.5053979

[94] J. A. Lewis, "Direct Ink Writing of 3D Functional Materials," *Advanced Functional Materials*, vol. 16, no. 17, pp. 2193–2204, nov 2006. [Online]. Available: http://doi.wiley.com/10.1002/adfm.200600434

[95] V. G. Rocha, E. Saiz, I. S. Tirichenko, and E. García-Tuñón, "Direct ink writing advances in multi-material structures for a sustainable future," *Journal of Materials Chemistry A*, vol. 8, no. 31, pp. 15 646–15 657, 2020. [Online]. Available: http://xlink.rsc.org/?DOI=D0TA04181E

[96] S. Z. Guo, M. C. Heuzey, and D. Therriault, "Properties of polylactide inks for solvent-cast printing of three-dimensional freeform microstructures," *Langmuir*, vol. 30, no. 4, pp. 1142–1150, 2014.

[97] Q. Wu, D. Therriault, and M. C. Heuzey, "Processing and Properties of Chitosan Inks for 3D Printing of Hydrogel Microstructures," *ACS Biomaterials Science and Engineering*, vol. 4, no. 7, pp. 2643–2652, 2018.

[98] P. J. Halley and M. E. Mackay, "Chemorheology of thermosets - An overview," *Polymer Engineering & Science*, vol. 36, no. 5, pp. 593–609, mar 1996. [Online]. Available: http://doi.wiley.com/10.1002/pen.10447

[99] A. W. Sisko, "Flow of lubricating greases," *Industrial Engineering Chemestry*, vol. 50, no. 12, pp. 1789–1792, 1958.

[100] H. J. Oh, B. D. Freeman, J. E. McGrath, C. J. Ellison, S. Mecham, K.-S. Lee, and D. R. Paul, "Rheological studies of disulfonated poly(arylene ether sulfone) plasticized with poly(ethylene glycol) for membrane formation," *Polymer*, vol. 55, no. 6, pp. 1574–1582, mar 2014. [Online]. Available: http://dx.doi.org/10.1016/j.polymer.2014.02.011

[101] A. V. Shenoy, *Rheology of Filled Polymer Systems*, 1st ed. Dordrecht: Springer Netherlands, 1999. [Online]. Available: http://link.springer.com/10.1007/978-94-015-9213-0

[102] K. C. Yung, J. Wang, and T. M. Yue, "Chemorheological study of phosphorylated flame retardant epoxies," *Plastics, Rubber and Composites*, vol. 40, no. 1, pp. 25–31, 2011.

[103] J. Bruneaux, D. Therriault, and M. C. Heuzey, "Micro-extrusion of organic inks for direct-write assembly," *Journal of Micromechanics and Microengineering*, vol. 18, no. 11, 2008.

[104] H. Lobo and J. Bonilla, "General Introduction To Plastics Analysis," in *Handbook of Plastics Analysis*, 2003.

[105] J. C. Pinto, "Polymer Processing Instabilities - Control and Understanding," *Macromolecular Materials and Engineering*, vol. 292, no. 1, pp. 95–95, jan 2007. [Online]. Available: http://doi.wiley.com/10.1002/mame.200600410

[106] C. Duty, C. Ajinjeru, V. Kishore, B. Compton, N. Hmeidat, X. Chen, P. Liu, A. A. Hassen, J. Lindahl, and V. Kunc, "What makes a material printable? A viscoelastic model for extrusion-based 3D printing of polymers," *Journal of Manufacturing Processes*, vol. 35, no. May, pp. 526–537, 2018. [Online]. Available: https://doi.org/10.1016/j.jmapro.2018.08.008

[107] E. Krayukhina, A. Fukuhara, and S. Uchiyama, "Assessment of the Injection Performance of a Tapered Needle for Use in Prefilled Biopharmaceutical Products," *Journal of Pharmaceutical Sciences*, vol. 109, no. 1, pp. 515–523, 2020. [Online]. Available: https://doi.org/10.1016/j.xphs.2019.10.033

[108] P. K. Mallick, *Fiber-reinforced composites: Materials, manufacturing, and design*, 3rd ed. Taylor & Francis Group, 2007.

[109] J. M. Kenny and M. Opalicki, "Processing of short fibre/thermosetting matrix composites," *Composites Part A: Applied Science and Manufacturing*, vol. 27, no. 3 PART A, pp. 229–240, 1996.

[110] C. Garschke, P. P. Parlevliet, C. Weimer, and B. L. Fox, "Cure kinetics and viscosity modelling of a high-performance epoxy resin film," *Polymer Testing*, vol. 32, no. 1, pp. 150–157, jul 2013. [Online]. Available: https://linkinghub.elsevier.com/retrieve/pii/S0142941812001900

[111] E. Ruiz and F. Trochu, "Numerical analysis of cure temperature and internal stresses in thin and thick RTM parts," *Composites Part A: Applied Science and Manufacturing*, vol. 36, no. 6, pp. 806–826, 2005.

[112] E. Ruiz and C. Billotte, "Predicting the cure of thermosetting polymers: The isoconversion map," *Polymer Composites*, vol. 30, no. 10, pp. 1450–1457, oct 2009. [Online]. Available: http://doi.wiley.com/10.1002/pc.20710

[113] Y. Zhao and D. Drummer, "Influence of filler content and filler size on the curing kinetics of an epoxy resin," *Polymers*, vol. 11, no. 11, 2019.

[114] R. J. Johnson and R. Pitchumani, "Characterization of the Rheology and Cure Kinetics of Epoxy Resin with Carbon Nanotubes," *Frontiers in Heat and Mass Transfer*, vol. 1, no. 1, 2010.

[115] Z. Su, Z. Wang, D. Zhang, and T. Wei, "Study on rheological behavior and surface properties of epoxy resin chemical grouting material considering time variation," *Materials*, vol. 12, no. 20, 2019.

[116] T. Beran, T. Mulholland, F. Henning, N. Rudolph, and T. A. Osswald, "Nozzle clogging factors during fused filament fabrication of spherical particle filled polymers," *Additive Manufacturing*, vol. 23, no. May, pp. 206–214, 2018. [Online]. Available: https://doi.org/10.1016/j.addma.2018.08.009

[117] N. Kiuna, C. J. Lawrence, Q. P. V. Fontana, P. D. Lee, T. Selerland, and P. D. M. Spelt, "A model for resin viscosity during cure in the resin transfer moulding process," *Composites Part A: Applied Science and Manufacturing*, vol. 33, no. 11, pp. 1497–1503, jun 2002. [Online]. Available: https://linkinghub.elsevier.com/retrieve/pii/S1359835X0200177X

[118] International Civil Aviation Organization, "ICAO Environmental Report 2016, aviation and climate change," ICAO, Montreal, Tech. Rep., 2016.

[119] R. Venegas and O. Umnova, "On the influence of the micro-geometry on sound propagation through periodic array of cylinders," *Proceedings - European Conference on Noise Control*, pp. 807–812, 2008.

[120] J. Boulvert, J. Costa-Baptista, T. Cavalieri, M. Perna, E. R. Fotsing, V. Romero-García, G. Gabard, A. Ross, J. Mardjono, and J. P. Groby, "Acoustic modeling of micro-lattices obtained by additive manufacturing," *Applied Acoustics*, vol. 164, p. 107244, 2020. [Online]. Available: https://doi.org/10.1016/j.apacoust.2020.107244

[121] J. Boulvert, T. Cavalieri, J. Costa-Baptista, L. Schwan, V. Romero-García, G. Gabard, E. R. Fotsing, A. Ross, J. Mardjono, and J.-P. Groby, "Optimally graded porous material for broadband perfect absorption of sound," *Journal of Applied Physics*, vol. 126, no. 17, p. 175101, nov 2019. [Online]. Available: http://aip.scitation.org/doi/10.1063/1.5119715

[122] M. Koller, A. Kruisová, H. Seiner, P. Sedlák, B. Román-Manso, P. Miranzo, M. Belmonte, and M. Landa, "Anisotropic Elasticity of Ceramic Micro-Scaffolds Fabricated by Robocasting," *Acta Physica Polonica A*, vol. 134, no. 3, pp. 799–803, sep 2018. [Online]. Available: http://przyrbwn.icm.edu.pl/APP/PDF/134/app134z3p42.pdf

[123] R. Sailesh, L. Yuvaraj, J. Pitchaimani, M. Doddamani, and L. B. Mailan Chinnapandi, "Acoustic behaviour of 3D printed bio-degradable micro-perforated panels with varying perforation cross-sections," *Applied Acoustics*, vol. 174, p. 107769, 2021. [Online]. Available: https://doi.org/10.1016/j.apacoust.2020.107769

[124] M. R. Khosravani and T. Reinicke, "Experimental characterization of 3D-printed sound absorber," *European Journal of Mechanics, A/Solids*, vol. 89, no. February, p. 104304, 2021. [Online]. Available: https://doi.org/10.1016/j.euromechsol.2021.104304

[125] X. Cai, Q. Guo, G. Hu, and J. Yang, "Ultrathin low-frequency sound absorbing panels based on coplanar spiral tubes or coplanar Helmholtz resonators," *Applied Physics Letters*, vol. 105, no. 12, pp. 1–5, 2014. [Online]. Available: http://dx.doi.org/10.1063/1.4895617

[126] C. R. Liu, J. H. Wu, X. Chen, and F. Ma, "A thin low-frequency broadband metasurface with multi-order sound absorption," *Journal of Physics D: Applied Physics*, vol. 52, no. 10, p. 105302, jan 2019. [Online]. Available: https://doi.org/10.1088{%}2F1361-6463{%}2Faafaa3https://iopscience.iop.org/article/10.1088/1361-6463/aafaa3/pdf

[127] I. Gibson, D. Rosen, and B. Stucker, *Additive Manufacturing Technologies*, 2nd ed. New York, NY: Springer New York, 2015. [Online]. Available: http://link.springer.com/10.1007/978-1-4939-2113-3

[128] Z. Jiang, B. Diggle, M. L. Tan, J. Viktorova, C. W. Bennett, and L. A. Connal, "Extrusion 3D Printing of Polymeric Materials with Advanced Properties," *Advanced Science*, vol. 7, no. 17, pp. 1–32, 2020.

[129] Y. Kang, W. Lee, J. Hwang, and Y. Lee, "Influence of glass microsphere filler on the rheological behavior of an epoxy resin," *International Polymer Processing*, vol. 33, no. 2, pp. 146–152, 2018.

[130] S. J. Park, F. L. Jin, and C. Lee, "Preparation and physical properties of hollow glass microspheres-reinforced epoxy matrix resins," *Materials Science and Engineering A*, vol. 402, no. 1-2, pp. 335–340, 2005.

[131] X. Zhang, P. Wang, Y. Zhou, X. Li, E. H. Yang, T. X. Yu, and J. Yang, "The effect of strain rate and filler volume fraction on the mechanical properties of hollow glass microsphere modified polymer," *Composites Part B: Engineering*, vol. 101, pp. 53–63, 2016.

[132] G. C. Huang and J. K. Lee, "Isothermal cure characterization of fumed silica/epoxy nanocomposites: The glass transition temperature and conversion," *Composites Part A: Applied Science and Manufacturing*, vol. 41, no. 4, pp. 473–479, 2010. [Online]. Available: http://dx.doi.org/10.1016/j.compositesa.2009.12.003

[133] D. Kokkinis, M. Schaffner, and A. R. Studart, "Multimaterial magnetically assisted 3D printing of composite materials," *Nature Communications*, vol. 6, 2015.

[134] G. Siqueira, D. Kokkinis, R. Libanori, M. K. Hausmann, A. S. Gladman, A. Neels, P. Tingaut, T. Zimmermann, J. A. Lewis, and A. R. Studart, "Cellulose Nanocrystal Inks for 3D Printing of Textured Cellular Architectures," *Advanced Functional Materials*, 2017.

[135] S. Kyle, Z. M. Jessop, A. Al-Sabah, and I. S. Whitaker, "'Printability' of Candidate Biomaterials for Extrusion Based 3D Printing: State-of-the-Art," *Advanced Healthcare Materials*, vol. 6, no. 16, pp. 1–16, 2017.

[136] D. Therriault, R. F. Shepherd, S. R. White, and J. A. Lewis, "Fugitive Inks for Direct-Write Assembly of Three-Dimensional Microvascular Networks,"

Advanced Materials, vol. 17, no. 4, pp. 395–399, feb 2005. [Online]. Available: http://doi.wiley.com/10.1002/adma.200400481

[137] T. Yuan, L. Zhang, T. Li, R. Tu, and H. A. Sodano, "3D Printing of a self-healing, high strength, and reprocessable thermoset," *Polymer Chemistry*, vol. 11, no. 40, pp. 6441–6452, 2020. [Online]. Available: http://xlink.rsc.org/?DOI=D0PY00819B

[138] 3M, "Technical Data Sheet for 3M Glass Bubbles - Floated Product Series," 2015. [Online]. Available: https://multimedia.3m.com/mws/media/91048O/3mtm-glass-bubbles-floated-product-series.pdf

[139] Evonik Industries, "Technical Data Sheet for Aerosil 200," p. 2, 2019. [Online]. Available: https://products-re.evonik.com/www2/uploads/productfinder/AEROSIL-200-EN.pdf

[140] M. Li, X. Tian, D. J. Schreyer, and X. Chen, "Effect of needle geometry on flow rate and cell damage in the dispensing-based biofabrication process," *Biotechnology Progress*, vol. 27, no. 6, pp. 1777–1784, 2011.

[141] S. Oka, "Pressure development in a non-Newtonian flow through a tapered tube," *Rheo. Acta*, vol. 12, pp. 224–227, 1973.

[142] L. Ouyang, R. Yao, Y. Zhao, and W. Sun, "Effect of bioink properties on printability and cell viability for 3D bioplotting of embryonic stem cells," *Biofabrication*, vol. 8, no. 3, p. 035020, sep 2016. [Online]. Available: https://iopscience.iop.org/article/10.1088/1758-5090/8/3/035020

[143] Z. Xu, W. He, F. Xin, and T. J. Lu, "Sound propagation in porous materials containing rough tubes," *Physics of Fluids*, vol. 32, no. 9, 2020.

[144] C. D. Field and F. R. Fricke, "Theory and applications of quarter-wave resonators: A prelude to their use for attenuating noise entering buildings through ventilation openings," *Applied Acoustics*, vol. 53, no. 1-3, pp. 117–132, 1998.

[145] S. Y. Song, X. H. Yang, F. X. Xin, S. W. Ren, and T. J. Lu, "Modeling of roughness effects on acoustic properties of micro-slits," *Journal of Physics D: Applied Physics*, vol. 50, no. 23, 2017.

[146] C. W. de Silva, "Frequency Response," in *Vibration: Fundamentals and Practice*. Boca Raton: Taylor & Francis Group, 2011, pp. 110–116. [Online]. Available: https://books.google.fr/books?id=wzfNBQAAQBAJ

[147] A. A. Kilbas and S. S. Nair, "Generalized fractional calculus of the generalized wright function," *Mathematical Sciences Research Journal*, vol. 13, no. 3, pp. 48–67, 2009.

[148] R. Gorenflo, Y. Luchko, and F. Mainardi, "Analytical properties and applications of the Wright function," *Journal for Theory and Applications*, vol. 2, no. 4, pp. 383–414, 2007. [Online]. Available: http://arxiv.org/abs/math-ph/0701069

APPENDIX A FLOW ANALYSIS FOR MATERIALS WITH A SISKO VISCOSITY MODEL

The flow rate equation presented in eq. (4.3) assumes the applicability of a one-parameter power-law, which states that

$$\eta(\dot{\gamma}) = K\dot{\gamma}^{n-1}. \tag{A.1}$$

However, the viscosity profile of many materials, including some thermosetting composites, are better represented with other models such as the one proposed by Sisko [90]. The Sisko model is a power-law with an additional term η_∞ to account for a Newtonian viscosity plateau at high shear rates:

$$\eta(\dot{\gamma}) = K\dot{\gamma}^{n-1} + \eta_\infty. \tag{A.2}$$

In this project, initial studies on neat resin (EC-3524 B/A) with GM loadings > 20 wt.% (without FS) it was found that the Sisko model showed good agreement with rheology data when fitting capillary and rotational data. Introducing this simple first-order constant term invalidates the flow rates predicted by eq. (2.9) and (2.10). As a result, eq. (4.6) cannot be exploited to predict printing speed under a given pressure and time after mixing. In such case, a new flow rate equation must be derived from first principles in fluid mechanics. Let us first define the equation of motion for an incompressible non-Newtonian fluid using the strain tensor $\overline{\overline{\tau}}$ and velocity vector $\vec{v}$ [84]:

$$\rho\left(\frac{\partial\vec{v}}{\partial t} + \vec{v}\cdot\nabla\vec{v}\right) = -\nabla P - \nabla\cdot\overline{\overline{\tau}} + \rho g. \tag{A.3}$$

To complete eq. (A.3), the associated equation of mass conservation in cylindrical coordinates is required:

$$\frac{1}{r}\frac{\partial(rv_r)}{\partial r} + \frac{1}{r}\frac{\partial v_\theta}{\partial\theta} + \frac{\partial v_z}{\partial z} = 0. \tag{A.4}$$

Note that eq. (A.4) is only valid for straight cylindrical nozzles. It is assumed that the capillary flow is purely axial, i.e. only the z is non-zero, thus reducing eq. (A.4) to

$$\frac{\partial v_z}{\partial z} = 0. \tag{A.5}$$

Assuming steady-state flow and strain tensor symmetry, it may be shown that by choosing a pure power law model (eq. (A.1)) to describe the material the full form of

eq. (A.3) reduces to:

$$\begin{bmatrix} 0 \\ 0 \\ 0 \end{bmatrix} = \begin{bmatrix} -\frac{\partial P}{\partial r} \\ -\frac{1}{r}\frac{\partial P}{\partial \theta} \\ -\frac{\partial P}{\partial z} \end{bmatrix} - \begin{bmatrix} 0 \\ 0 \\ \frac{K}{r}\frac{d}{dr}\left[r\left(-\frac{dv_z}{dr}\right)^n\right] \end{bmatrix} + \begin{bmatrix} 0 \\ 0 \\ \rho g \end{bmatrix}. \tag{A.6}$$

It may be observed, in eq. (A.6), that pressure P is dependent of the axial coordinate z, thus the partial differential may be rewritten as dP/dz. In order to find the velocity profile and then the flow rate, eq. (A.7) must be solved using separation of variables by equating separately each side to an arbitrary constant, $\hat{\lambda}$:

$$\frac{dP}{dz} = \rho g - \frac{K}{r}\frac{d}{dr}\left[r\left(-\frac{dv_z}{dr}\right)^n\right] (= \hat{\lambda}). \tag{A.7}$$

The left-hand-side of eq. (A.7) is solved in a straightforward manner by taking the appropriate boundary conditions (i.e. $P(z=0) = P_0$ and $P(z=L) = P_L$):

$$\frac{dP}{dz} = \hat{\lambda} \Rightarrow P = \frac{P_L - P_0}{L} z + P_0. \tag{A.8}$$

where P_0 and P_L are the head and barometric pressure, respectively. As for the right-hand-side of eq. (A.7), with the constant $\hat{\lambda}$ known, the differential equation is rearranged to allow for solving through separation of variables:

$$\begin{aligned} (\rho g - \hat{\lambda}) \cdot \frac{r}{K} &= \frac{d}{dr}\left[r\left(-\frac{dv_z}{dr}\right)^n\right]. \\ \Rightarrow (\rho g - \hat{\lambda}) \cdot \frac{r}{2K} + c_1 &= \left(-\frac{dv_z}{dr}\right)^n. \end{aligned} \tag{A.9}$$

With the result of eq. (A.5), the constant c_1 in eq. (A.9) is trivial. Therefore, if $0 < n < 1$, solving eq. (A.9) by taking the n^{th} root and separating variables gives the velocity profile:

$$\begin{aligned} -\left((\rho g - \hat{\lambda}) \cdot \frac{r}{2K}\right)^{\frac{1}{n}} &= \frac{dv_z}{dr} \\ \Rightarrow -\left(\frac{\rho g - \hat{\lambda}}{2K}\right)^{\frac{1}{n}} \frac{r^{1+\frac{1}{n}}}{1+\frac{1}{n}} + c_3 &= v_z(r). \end{aligned} \tag{A.10}$$

Considering a zero velocity at the wall ($v_z(R) = 0$), the integration constant c_2 in eq. (A.10) is found as

$$c_2 = \left(\frac{\rho g - \hat{\lambda}}{2K}\right)^{\frac{1}{n}} \frac{R^{1+\frac{1}{n}}}{1+\frac{1}{n}}. \tag{A.11}$$

Substituting in the definition of $\hat{\lambda}$ found when solving eq. (A.8) and the constant c_2 into eq. (A.11), the non-Newtonian velocity profile as function of radius r from the centre of the flow is given by

$$v_z(r) = R^{\frac{1+n}{n}} \left(\frac{1+n}{n}\right) \left(\frac{\rho g L + P_0 - P_L}{2KL}\right)^{\frac{1}{n}} \left[1 - \left(\frac{r}{R}\right)^{\frac{1+n}{n}}\right]. \tag{A.12}$$

The gravity term $\rho g l$ may be neglected for short nozzle and high pressures. Eq. (A.12) may be further manipulated to obtain the volume flow rate for a pure power-law material, starting from the flow rate in eq. (A.13):

$$Q = \int 2\pi r v_z(r) dr \tag{A.13}$$

$$= R^{\frac{3n+1}{n}} \left(\frac{\pi n}{3n+1}\right) \left(\frac{\rho g L + P_0 - P_L}{2KL}\right)^{\frac{1}{n}}. \tag{A.14}$$

With the η_∞ term in eq. (A.2), the solution for the velocity profile is analogous to that of the pure power law, but becomes relatively complex at eq. (A.9), however, due to the presence of an extra first-order derivative term. In this case, a differential equation of the following form must be solved (e.g., via Laplace transforms):

$$v_z^{(n)}(r) + A v_z^{(1)}(r) + B v_z(r) = 0 \tag{A.15}$$

where

$$A = \tfrac{\rho g - \hat{\lambda}}{2K} \quad , \quad B = \tfrac{\eta_\infty}{n} \quad , \quad \hat{\lambda} = \tfrac{P_L - P_0}{L}.$$

Solutions to this type of differential equation will take the following form [147, 148]:

$$v_z(r) = v_0 \sum_{m=0}^{+\infty} \frac{(-B)^m r^{nm}}{m!} \, {}_1\Psi_1 \left\{ \begin{matrix} (m+1,\ 1) \\ (nm+1, n-1) \end{matrix} \middle| -A r^{n-1} \right\}$$
$$+ A v_0 \sum_{m=0}^{+\infty} \frac{(-B)^m r^{nm+n-1}}{m!} \, {}_1\Psi_1 \left\{ \begin{matrix} (m+1,\ 1) \\ (nm+n, n-1) \end{matrix} \middle| -A r^{n-1} \right\}, \tag{A.16}$$

where ${}_p\Psi_q$ is the Wright function defined as the a product series of gamma functions. The Wright function is written in its general form as

$$ {}_p\Psi_q \left\{ \begin{matrix} (a_i, \alpha_i)_{1,p} \\ (b_j, \beta_j)_{1,q} \end{matrix} \middle| \; z \right\} := \sum_{h=0}^{\infty} \frac{\prod_{i=1}^{p} \Gamma(a_i + \alpha_i h)}{\prod_{j=1}^{q} \Gamma(b_j + \beta_j h)} \frac{z^h}{h!}. \tag{A.17} $$

Therefore, the theoretical flow rate (calculated with eq. A.13) for a material with a Sisko material is expressed by

$$ \begin{aligned} Q = 2\pi v_0 \sum_{m=0}^{\infty} \frac{(-B)^m}{m!} \sum_{h=0}^{\infty} \frac{\Gamma\left(m+h+1\right)(-A)^h \, r^{(n-1)h+nm+2}}{\Gamma\left((n-1)\,h+nm+1\right) h!((n-1)\,h+nm+2)} \\ + 2\pi \; Av_0 \sum_{m=0}^{\infty} \frac{(-B)^m}{m!} \sum_{h=0}^{\infty} \frac{\Gamma\left(m+h+1\right)(-A)^h \, r^{(n-1)h+nm+n+1}}{\Gamma\left((n-1)\,h+nm+n\right) h!((n-1)\,h+nm+n+1)}. \end{aligned} \tag{A.18} $$

The expression in eq. (A.18) is significantly more complex to implement than eq. (2.9) and is only valid for materials with a rheological behaviour modelled by Sisko law. Besides, in this work it was found that the neat resin filled only with GM is not a satisfactory solution to print abradable materials with a sound absorbing function. Consequently, the foregoing mathematical developments yielding eq. (A.18) were not verified with empirical data; rather, these steps may prove useful in future works dealing with materials following a Sisko model, because these theoretical developments, and specifically eq. (A.18), have not been derived in the literature.

APPENDIX B SUPPLEMENTARY INFORMATION FOR ARTICLE 1

Vid. S1. μCT reconstruction of a 15-layer 0GM:12FS micro-scaffold printed with a tapered 250 μm nozzle at 50 mm.s^{-1}. The reconstruction shows in a non-destructive manner that the spanning filaments keep their circular shape for all stacked layers, and that there are few manufacturing defects throughout the sample. (Available at `https://youtu.be/X1Ksw7-4OTs`)

Vid. S2. μCT reconstruction of a 50-layer 10GM:8FS micro-scaffold printed with a tapered 250 μm nozzle at 50 mm.s^{-1}. The reconstruction shows in a non-destructive manner that the spanning filaments keep their circular shape for all stacked layers, and that there are few manufacturing defects throughout the sample. (Available at `https://youtu.be/dR4AXzGQf8s`)

Table B.1 Micro-computed tomography scan parameters

Image	**Sample**	**Objective**	**Vox size, [μm]**	**Exposure, [s]**	**Voltage, [kV]**	**Power, [W]**	**Projections**	**Filter**
Figure 4.3 (a)	0GM:12FS filament	4.0×	1.31	5.5	60	5.0	3201	LE3
Figure 4.3 (d)	5GM:10FS filament	4.0×	1.31	6.0	60	4.9	4502	LE3
Figure 4.3 (g)	10GM:8FS filament	4.0×	1.42	5.0	80	7.0	4501	LE3
Figure 4.3 (j)	15GM:7FS filament	4.0×	1.15	11.0	50	4.0	4501	LE3
Figure 4.3 (m)	20GM:6FS filament	4.0×	1.34	5.0	60	5.0	4501	LE3
Figure 4.3 (p)	Benchmark filament	4.0×	1.34	5.2	60	5.0	4601	LE3
Vid. S1	0GM:12FS scaffold	0.4×	7.45	2.2	50	4.0	1019	Air
Vid. S2	10GM:8FS scaffold	0.4×	12.89	1.8	50	4.0	1017	Air

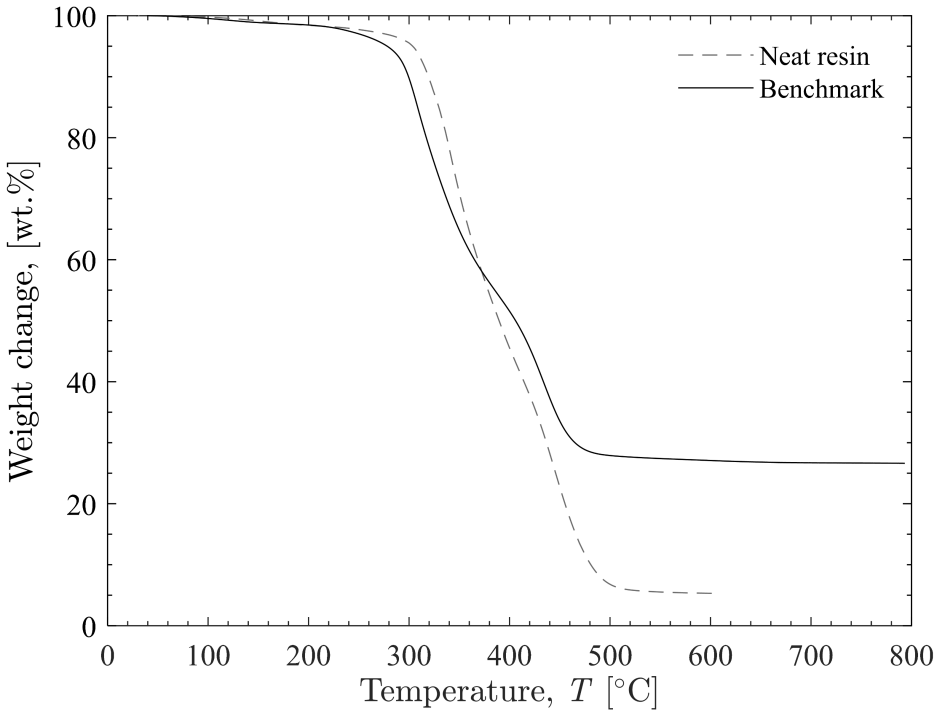

Figure B.1 Comparison of residual content for the benchmark and neat resin obtained through TGA (heating rate of 20 °C.min^{-1} under nitrogen atmosphere). The test for the neat resin was stopped at 600 °C where no additional weight variation was observed. The residual contents in the neat resin indicate that the resin system contains ∼95 wt.% of epoxy, the remainder (∼5 wt.%) being attributed to additive (e.g. carbon black) which decompose beyond 800 °C The benchmark has a residual weight content of ∼27.5 wt.%, including GM fillers and residuals. Subtracting the contribution of additives in the NR from the benchmark places the loading of GM in the benchmark to ∼22.5 wt.%.

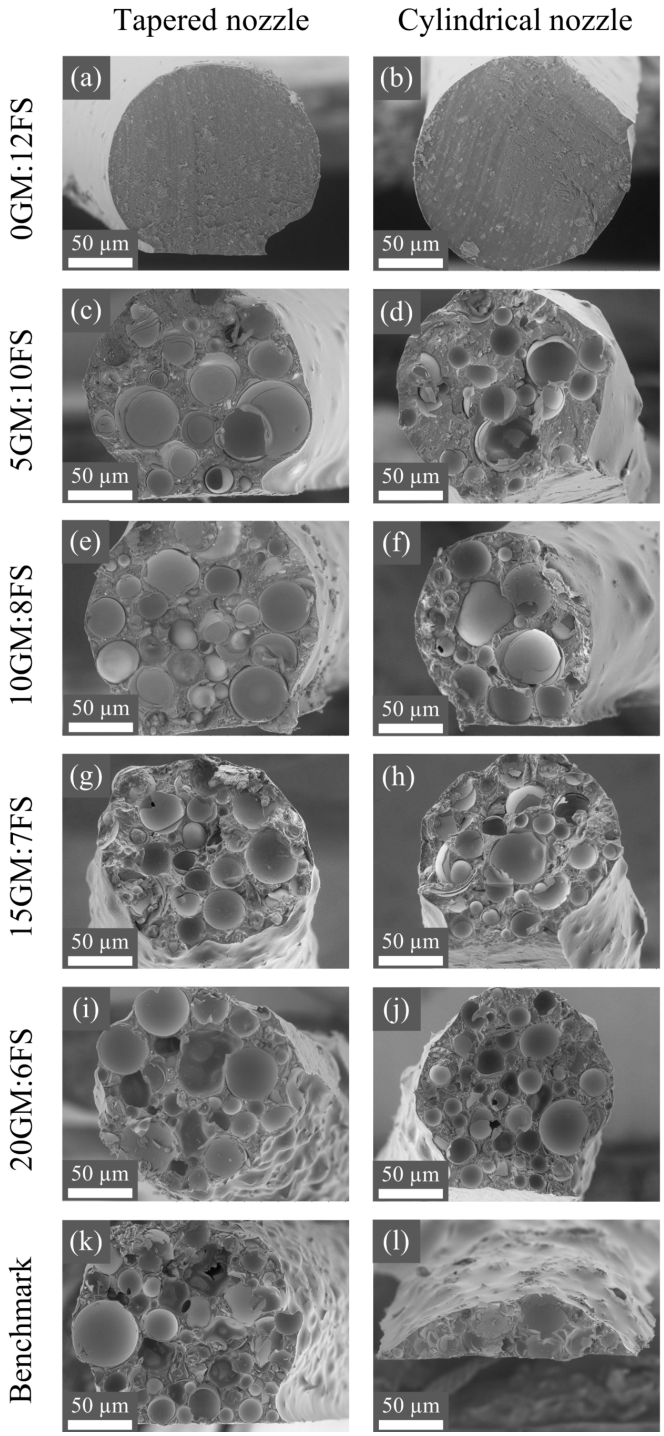

Figure B.2 SEM cross-section images of filaments extruded at 4.55 MPa through tapered and cylindrical 250 µm nozzles for (a,b) 0GM:12FS, (c,d) 5GM:10FS, (e,f) 10GM:8FS, (g,h) 15GM:7FS, (i,j) 20GM:6FS blends, and (k,l) the benchmark material. No GM crushing is observed using either nozzle geometries for star blends (0GM:12FS, 5GM:10FS and 10GM:8FS). GM crushing occurs for both cylindrical and tapered of nozzles for 15GM:7FS 20GM:6FS blends and the benchmark. Higher GM loadings cause inhomogeneous filament microstructures with variable degrees of filler crushing.

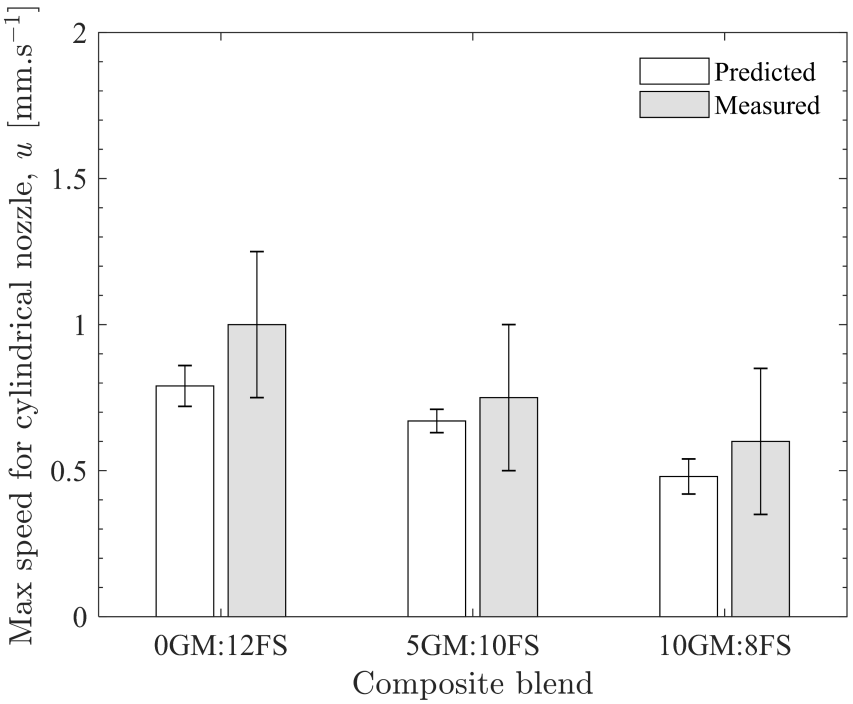

Figure B.3 Comparison between predicted and measured printing speeds for star blends at maximum system pressure through a 250 μm cylindrical nozzle, 30 minutes after material mixing. Predicted values are computed from the viscosity models using parameters and their respective confidence intervals from Table 4.3 & Table 4.4 and eq. (4.6). Measured speeds taken for a filament diameter equal to the nozzle tip diameter based on optical microscope measurements. For measured speeds, the error bars represent standard deviations resulting from taking the average of measured filament diameters. Errors for predicted speeds are derived from parameter confidence intervals and error propagation obtained during modelling. Predicted speeds are in good agreement with measured maximum speeds, suggesting the viscosity model is transferable between tapered and cylindrical nozzle of 250 μm diameter.